MILLIMETER SCALE ROBOTS FOR THE NANOFACTORY

by

RAKESH MURTHY

Presented to the Faculty of the Graduate School of

The University of Texas at Arlington in Partial Fulfillment

of the Requirements

for the Degree of

DOCTOR OF PHILOSOPHY

THE UNIVERSITY OF TEXAS AT ARLINGTON

December 2009

Copyright © by Rakesh Murthy 2009

All Rights Reserved

ACKNOWLEDGEMENTS

With my ambition of getting a doctoral degree approaching reality, I wish to dedicate this dissertation to my Mother, Pushpa Murthy and my Father, Sreedhara Murthy. I abstract their never ending support, encouragement and sacrifice towards all my dreams as a miracle and without which I would not have seen this day. Thanks Mom and Dad! I think my Father being a Professor has had a deep and hidden influence on some of my career decisions, and in understanding my future ambitions and I wish to thank him for that. I have always enjoyed my visits to his department in Mangalore University from the time I was a kid up until the last time I was there, a few months ago.

I owe all my knowledge, understanding and creativity in Robotics and Microsystems to my advisor Prof. Dan Popa. Under his guidance, I have matured along many technical and non technical fronts and I wish to express my gratitude. I have been his student for six years and hope to associate with him for a much longer time in the future. I thank Prof. Harry Stephanou for supporting me as a GRA during all these years, for his participation as a part of my dissertation committee, and for always encouraging me to look at the bigger picture in research. His critical reviews and discussions during my presentations at ARRI, have added immense value to my research. I would like to acknowledge and thank Dr. Woo Ho Lee for getting me started with my fabrication processes at Stanford Nanofab and for his participation as a member of my dissertation committee. I would also like to acknowledge Prof. Kamesh Subbarao and Prof. Frank Lewis for their insightful suggestions about my dissertation and for agreeing to be a part of my dissertation committee.

My experience at ARRI has been enriched by many researchers and staff with whom I have been fortunate to work with. I wish to thank Aditya Das, Mohammad Mayyas, Jeongsik

Sin, and Norm Spayd. I also like to acknowledge Jartuwat Rajruangrabin, Kathleen Elfrink, Alexis Bedoin, Remi Braud, Isaac Weintraub, Sanket Rathore, Charles Brown, and Ricky.

I wish to thank my friends Nayantara Mallesh and Rohan Rao who made it possible to have a life outside of my lab and research. I will always carry fond memories of times spent with them, such as our trip to Mexico, and the AM shows. I am looking forward to continuing our friendship for the years to come.

Finally, going back to family, I wish to acknowledge and thank my dearest brother Rajeev "juj" Vasisht. I will always cherish our childhood spent together, specially the few years in Bangalore. He has been a role model and shaped my character and personality in a profound and positive manner.

November 12, 2009

ABSTRACT

MILLIMETER SCALE ROBOTS FOR THE NANOFACTORY

Rakesh Murthy, PhD

The University of Texas at Arlington, 2009

Supervising Professor: Dan O. Popa

The top down approach is a commonly employed miniaturization pathway into micro and nanomanufacturing. Its popularity is due to the fact that it adapts traditionally engineered macro scale positioning, manipulation and processing technology with micro and nano scale precision and part sizes. However, state of the art top down systems such as the Atomic Force Microscope (AFM) span four to five orders of magnitude larger than the parts being handled. This dissertation addresses the need for creating millimeter size robotic positioning technology that closes the size gap between equipment and part sizes. Such microrobot manufacturing methodology comprising of micro component-level design, fabrication and high yield assembly, system-level packaging, modeling, precision evaluation and control is presented and exemplified using two classes of microrobots. Both microrobots incorporate Micro Electro Mechanical Systems (MEMS) to combine high precision and low foot-print.

The first microrobot type, the “ARRIpede” is a multi legged autonomous crawler, and is designed to operate as a mobile unit enabling parts transfer in a nanoassembly environment. An embodiment of this microrobot is demonstrated for planar motions with three degrees of freedom (XYθ). The microrobot consists of a MEMS die “belly” spanning 10mm x 10mm x 1mm with in-plane electrothermal actuators and vertically assembled legs, and an electronic “backpack” spanning 15mmx15mmx10mm to generate a leg gait sequence. By incorporating

bulk micromachined parts and precise epoxy dispensing at the assembled leg joint, the microrobot has a high payload bearing capacity (at least 9g). Simulations with a nonholonomic robot predict microcrawler velocities of a few mm/s under realistic assumptions. The open loop crawling velocity is experimentally characterized for various actuator frequencies and a close match with simulations is observed. A Linear Quadratic Regulator (LQR) based controller consisting of a high magnification camera and a laser displacement sensor for feedback is implemented. The open/closed loop positioning repeatabilities are evaluated and compared. .

The second micro robot called the "AFAM" (Articulated Four Axes Micro Robot) is a fixed base articulated design targeting micro and nano scale manipulation and probing applications. An embodiment of this microrobot is constructed incorporating four degrees of freedom (X, Y, Pitch and Yaw), occupying a total volume of 3mm x 2mm x 1mm, and operating within a workspace envelope of 50µm x 50µm x 75µm. This is by far the largest operating envelope of any other independent MEMS positioner with non-planar dexterity. A cable based transmission and motion amplification mechanism is designed to achieve the pitch and yaw degrees of freedom. The de-coupled motion of the microrobot is achieved by kinematic identification of the Jacobian and using a 3D flexure based kinematic model of the microrobot. By using the derived kinematics, the microrobot is driven to create nanoindents on a polymer surface. The end-effector positioning accuracy, repeatability and resolution are characterized using the nanoindents.

TABLE OF CONTENTS

ACKNOWLEDGEMENTS iii

ABSTRACT v

LIST OF ILLUSTRATIONS xi

LIST OF TABLES xvi

Chapter Page

1. INTRODUCTION 1

1.1 Motivation 1

1.2 Contribution 7

1.3 Dissertation Outline 10

2. BACKGROUND 12

2.1 Micro and Nanofactories. 12

2.2 Microrobots 13

2.3 MEMS Positioners 16

2.4 Microassembly and Manipulation 17

2.5 Nanoassembly and Manipulation 20

2.6 Nanorobots 23

3. A FRAMEWORK TOWARDS MANUFACURABLE MICROROBOTS 26

3.1 MEMS or not? 26

3.2 Framework Description 26

3.2.1 Design for Micromanufacturing 27

3.2.1.1 Component level design for performance 27

3.2.1.2 Component level design for manufacturing 28

3.2.1.3 System level design updates 28
3.2.1.4 Process improvement loop 29
3.3 Microrobot Process Indices 30
3.3.1 Mobile Microrobot 30
3.3.2 Articulated Arm 33
3.4 Actuation Technology 34
3.4.1 Figure of Merit 34
3.4.2 Actuation Force Requirement 35
3.5 Joints and Motion Transmission 37
3.6 Fabrication 40
4. MICROROBOT MANUFACTURING 42
4.1 Design of Microsnapfasteners for High Yield Assembly 42
4.1.1 HYAC Lemma 42
4.1.2 Micro part design for compliance based assembly 43
4.2 Design Example 44
4.3 Fabrication 47
4.4 Microassembly 52
4.5 Tolerance Analysis and Experimental Verification 54
4.6 Packaging 58
4.6.1 Packaging Requirements 58
4.6.2 Manual Packaging Setup 60
4.6.2.1 Die Attach 60
4.6.2.2 Wire Bonding 60
4.7 Automated Microsystems Packaging 63
4.7.1 Overview & System Architecture 63
4.7.2 Qualitative design rules 65

4.7.3 Inverse Kinematics for Die Attach 71

4.7.4 Visual Servoing 74

5. ARRIPEDE MICROCRAWLER 78

5.1 Micro robot description 78

5.2 Motion Principle and Prismatic Joint Design 79

5.3 Microfabrication and assembly 81

5.4 Backpack Electronics 81

5.5 Leg joint strength estimation 83

5.6 Packaging 84

5.7 Gait and dynamic analysis 85

5.7.1 ARRIpede Gait 85

5.7.2 Dynamics 85

5.8 Experimental Characterization 89

5.9 Modified dynamics for Closed Loop Control 93

5.10 Motion Control 97

5.10.1 Coarse tracking controller 97

5.10.2 Fine tracking controller 98

5.10.3 Trajectory Tracker 99

5.11 Precision Measurement 102

6. ARTICULATED FOUR AXIS MICRO ROBOT (A.F.A.M) 105

6.1 Introduction 105

6.2 Design methodology 107

6.3 Fabrication and Assembly 111

6.3.1 Fabrication 111

6.3.2 Z Stage and Cable Assembly 112

6.3.3 AFM Probe Assembly 113

6.4 Experimental characterization 113

6.4.1 Work Envelope Measurement 113

6.4.2 System Jacobian 114

6.4.3 Preliminary Precision Evaluation 116

6.4.3.1 Resolution 117

6.4.3.2 Repeatability 118

6.4.3.3 Accuracy 118

7. CONCLUSIONS & FUTURE WORK 121

7.1 Conclusions 121

7.2 Future Work 121

APPENDIX

A. SOI MEMS FABRICATION RECIPE 125

B. M^3 CONFIGURATION 130

C. DESIGN LAYOUTS 143

REFERENCES 153

BIOGRAPHICAL INFORMATION 163

LIST OF ILLUSTRATIONS

Figure Page

1.1 Top-Down Micromanufacturing 3

1.2 Nanofactory planning for Hybrid Nanoassembly 6

1.3 Nanofactory concepts.(a) Nanofactory on a 4” wafer (b) Nanomanipulation module 7

1.4 Microrobot manufacturing framework 8

2.1 Nanowalker Robot 14

2.2 Piezo MEMS enabled Millimeter Scale Robot 14

2.3 Jumping Microrobot 15

2.4 Microassembly techniques 19

2.5 Microassembly Station at the University of Toronto 19

2.6 Microassembly Station at the University of Oldenburg 20

2.7 Microrobot based Microassembly 21

2.8 Fukuda Lab Nanomanipulation Cell 24

2.9 Teleoperated nanorobotics system 24

2.10 Commercial Nanomanipulators. (a) Zyvex; (b) Kleindiek 25

3.1 Design for Micromanufacturing Robots 31

3.2 Microrobot design examples Microrobot design examples (a) Multiple assembly instances; (b) Component with passive gripper; (c) Assembled component; (d) Electrical interconnect 32

3.3 One degree of freedom flexure 38

3.4 Two axes flexure joint 39

3.5 Two axes flexure design 39

3.6 SCREAM Bulk Micromachining 41

4.1 Microsnapfastener FBD. (a) Free body diagram depicting the insertion of rigid part B into compliant snap-fastener A, shown in a two-point crossing state; (b) assembled condition. 44

4.2 Design of microsnapfastener and micropart 45

4.3 Microsnapfastener design. (a) Micro fastener modeled as a spring+ cantilever (b) -fastener misalignment with part 46

4.4 Force variation during microassembly- Insertion force (Y axis) variation for varying cantilever parameters versus insertion distance (X axis). (a) Low insertion & high retention forces (b) Experimental force insertion measurement 47

4.5 SOI Device Layer Microfabrication Process 48

4.6 SOI Handle Layer Microfabrication Process 49

4.7 Design layout for a 4” wafer 50

4.8 $2^1/_2$D part 50

4.9 Microrobot Joints. Left-Flexure joints,Right-Assembled joints 51

4.10 Assembled 3D Microflyer Mechanism 52

4.11 Combination of monolithic and flexure joints 53

4.12 Microassembly Platform. (a) Schematic diagram of μ^3 (meso-micro-nano) platforms with micro grippers; (b) Kinematic representation of the multirobot system 55

4.13 Part on substrate. (a) before detethering ;(b)after detethering 55

4.14 Surface profile data of the released and detethered micro part 56

4.15 Coordinate system transformation between part-on-substrate and assembly condition 56

4.16 Microassembly. (a) Assembly scene (b) Compliant gripping on part 57

4.17 Array of parts assembled using the μ^3 system 58

4.18 Microcrawler line diagram with backpack 59

4.19 Microrobot packaging setup 61

4.20 Wire bonding technique 62

4.21 Completed wire bond 63

4.22 M^3 assembly and packaging station 64

4.23 Schematic diagram of methodology for designing a
multiscale assembly system such as the M^3 66

4.24 Decrease in calibration error (σ_2) with an increase
in the number of calibration points 75

4.25 Die to carrier misalignment calculation based on imaging of
three carrier feed-through holes and three DRIE trenches on
the MEMS die. 77

5.1 ARRIpede (a) ARRIpede belly up with 8 legs;
(b)SEM image of prismatic joint 78

5.2 ARRIpede description (a) ARRIpede Microcrawler solid model
showing legs . b) Leg assembly with thermal prismatic joint; c)
Inverted ARRIpede microcrawler carrying electronics backpack;
d)Microcrawler carrying a 4g payload. 79

5.3 ARRIpede wave gait over one step. (a)~(e) depict complete
robot and figures (f)~(h) refer to a single leg. 80

5.4 ARRIpede layout diagram using LASI®. 81

5.5 Electronics Backpack. (a) Backpack components (b) Power
supply schematic; (b) High frequency multiplexing of input
pulses to the ARRIpede 82

5.6 Joint strength determination. (a), (b) Microforce sensor measuring
joint strength of ARRIpede; (c) Microrobot weight acting on a
misaligned leg. 83

5.7 Complete ARRIpede Package 84

5.8 Electronics Backpack 85

5.9 ARRIpede microrobot displacement per cycle for different friction
models. The drift observed in X_2 is a numerical artifact and is overcome
by the execution of a subsequent step in the gait sequence 89

5.10 Experimenting payload conveyance on ARRIpede with belly-up position 90

5.11 ARRIpede in a six legged configuration. 91

5.12 Displacement profiles. (a) ARRIpede forward motion along X (mm)
for varying amplitude and frequencies (b) Drift sideways along Y
axis (mm) 92

5.13 Payload tracked in conveyor mode. (a) ,(b) Forward motion for varying amplitude and frequencies with constant amplitude-frequency products; (c) -steering left,(d) steering right-with mismatched actuation frequencies. 93

5.14 Revised model description. (a) ARRIpede leg~belly and leg~ground interface and types of friction (b): Vector fields controlling robot orientation; legs depowered in the sequence shown 1~6 94

5.15 Representation of net force with respect to the center of mass 95

5.16 ARRIpede simulated motion for varying input amplitudes and frequencies 97

5.17 Experimental verification of displacement profile; (a) Hardware setup diagram, (b) Coarse Fine Controller Implementation 98

5.18 Control Block Diagram of the LQR Controller 100

5.19 LQR controller simulations at various actuation frequencies 101

5.20 ARRIpede precision measurements. (a) Setup; (b) Repeatability along X; (c) Repeatability along Y; (d) Electrothermal actuator resolution 103

6.1 Scanning Electron Microscope of the AFAM 106

6.2 Solid model of the microrobot and DOF notation and Kinematic Representation (P:Prismatic; R: Revolute). 106

6.3 Microrobot design sequence and parameters 108

6.4 XY stage design 109

6.5 XY Stage performance evaluation using FEA and experiments. (a)~(c) left column: Simulated axis and coupled axis motion profile for various flexure parameters-(a): Higher displacement (45 microns) and low torsional rigidity(0.26 N-m^2/rad); (b) Medium deflection (40 microns) and medium torsional rigidity (0.38 N-m^2/rad); (c) Low deflection (24 microns) and high torsional rigidity (0.5 N-m^2/rad); right column- experimentally measured displacements. 110

6.6 Z axis arm 111

6.7 Cable assembly 112

6.8 AFM probe mounted onto microrobot using a micro fixture 113

6.9 Microrobot work volume evaluation (points mark locations reached during volume sweep). 114

6.10 Indentations on a 2μm thick Parylene surface 116

6.11 A 3x3 Nanoindentation grid for repeatability measurement ... 116
6.12 Resolution measurement setup ... 117
6.13 Resolution variations along four DOF's ... 119
6.14 Repeatability measurement ... 120
6.15 Accuracy measurements ... 120
7.1 Controller for hybrid nano assembly ... 123
7.2 Work Volume of Nano Manipulation Workcell ... 123
B.1 Kovar Carrier (top view) ... 131
B.2 Sn-Au Preform ... 131
B.3 Completed Package ... 132
B.4 Four Axes Robot ... 133
B.5 Three Axes Robot ... 133
B.6 Two Axes Robot ... 134
B.7 Carrier Gripper ... 135
B.8 Die Pick Up Tool ... 135
B.9 M3 setup- Die Attach Sequence ... 138
B.10 Robot Home Positions ... 139
B.11 Visual Servoing VI ... 142
B.12 Inverse Kinematics VI ... 142
C.1 ARRIpede Actuator Type1 ... 144
C.2 ARRIpede Leg ... 144
C.3 ARRIpede Actuator Type2 ... 145
C.4 ARRIpede Actuator Type3 ... 145
C.5 ARRIpede Belly Type1 ... 146
C.6 ARRIpede Belly Type 2 ... 147
C.7 XY Stage type1 ... 148

C.8 XY Stage type1 149

C.9 Microsnapfastener type 1 149

C.10 Part corresponding to figure C.9 150

C.11 Single DOF flexures 150

C.12 Z Axis Arm for the AFAM version 1 151

C.13 Microsnapfastener type 2. 151

C.14 Z axis arm version 2. 152

LIST OF TABLES

Table Page

1.1 Nano factory scanning and manipulation attributes. 6

3.1 Comparison of actuation techniques 35

3.2 Figure of Merit 36

4.1 R_1 Calibration Results, Camera (Mm) & Pixel Coordinates 74

4.2 R_2 Calibration Results, Translation In Mm, Angles In Degrees & Pixel Coordinates 74

4.3 Experimental (X,Y) Data (µm) Showing Die To Carrier Misalignment 75

5.1 Robot speed results from vision data for forward motion, and the effect of the amplitude-frequency product 91

5.2 ARRIpede steering data 91

6.1 Actuator to joint relationships 106

6.2 Sample measured displacement data at TCP 115

B.1 Tolerance Budget for Die Attach 132

B.2 Pneumatic Hardware 134

B.3 End Effector Design 136

B.4 Camera Calibration Data 141

B.4 Robot Calibration Data 141

CHAPTER 1

INTRODUCTION

1.1 Motivation

Microsystems technology (MST) has brought profound possibilities to the future of science and engineering. Over the past two decades, this technology has grown deep and wide and finds applications within various disciplines like biotechnology, medicine, robotics, optics, automotive engineering, space and propulsion, etc [1-2]. Devices that are manufactured using MST, popularly called Micro Electro Mechanical Systems (MEMS) are small, light and can be batch manufactured. Perhaps, one of the most significant roles played by MST or MEMS is that of a portal to exploring the exciting world of nanotechnology. For example, micromachined grippers and probes in conjunction with micromachined piezoelectric actuators are invaluable tools used in nano material characterization, nanoassembly, handling and manipulation of biological cells, etc [3-4].

Micromanufacturing has evolved rapidly in recent years, and in addition to Silicon it also uses materials such as metals, polymers, glass, etc with a minimum feature size as low as 500 nm. There are a number of different fabrication techniques that are used to make micro components and MEMS devices. One of the most widely used methods is surface micromachining which is based upon IC fabrication techniques used in microelectronics industry [5]. Surface micromachining, like IC fabrication, is based upon successive deposition and etching of thin films of materials such as poly silicon. Another common technique is bulk micromachining with examples such as Deep Reactive Ion Etching of Silicon on Insulator materials and LIGA (an acronym for lithography, electroplating and forming in German) [6-7]. Other non conventional techniques that can be used are micro electro discharge machining (EDM), laser micromachining [8]. Most of these techniques commonly used for fabrication

result in micro parts that are essentially $2^1/_2$D (or planar). With techniques leading to 3D profiles, their throughput is a serious limitation. The resulting MEMS primarily consist of a single type of material or group of materials that are closely related in composition and fabrication related compatibility and termed *'Monolithically Fabricated Systems'.* Such systems, though easy to manufacture are limited in their functionality due to the limited choice of materials and planar design of components. In order to overcome this disadvantage and achieve higher functionality along the vertical axis, '*microassembly'* is employed. This is involves using a microgripper that is designed to manipulate at this scale taking scaling effects into consideration.

Packaging is another important aspect of micromanufacturing. It refers to the establishing of electrical, optical or mechanical interconnects between various internal modules of the MEMS device and between the device and the outside world. Packaging usually results in maintaining a suitable operating atmosphere for the device, providing mechanical support and establishing optical, electrical, mechanical, or fluidic feedthroughs to the system without compromising with the other conditions. Thus, micromanufacturing consisting of fabrication, assembly and packaging is a multifaceted problem.

High precision positioning systems play a critical role in micro systems manufacturing. They facilitate probing, gripping and positioning tasks and can be designed to handle specific applications such as nanoscale micro assembly, alignment of optics, recording media positioning in high density storage devices, etc. One of the approaches in designing these positioning systems has been the so-called "Top Down" approach in which macro scale positioning systems have operated upon micro and nano scale parts. These systems enable very high precision positioning, with placement resolution going down to the order of a few nanometers. However, they span atleast four to five orders of magnitude larger than the parts being handled, leading to tradeoffs between precision, throughput and cost. Thus, there is a need for *millimeter and micron sized positioning system technology* that combine high precision

with high throughput along with other application-specific requirements such as strength, dexterity, bandwidth, and work volume.

From a production point of view, micromanufacturing can be defined as the miniaturizing of products, some of which take the form of miniaturized production tools and consequently lead to ultra miniature products. This is illustrated in figure 1.1. Referring to this figure, the most common route (referred to as type 1 in the figure) employs macro scale production tools in manufacturing MEMS. This is the most popular approach, as it adapts already existing technology into building useful micro systems. In this case however, the production tools use as much space and energy as when they are used to produce macro scale products.

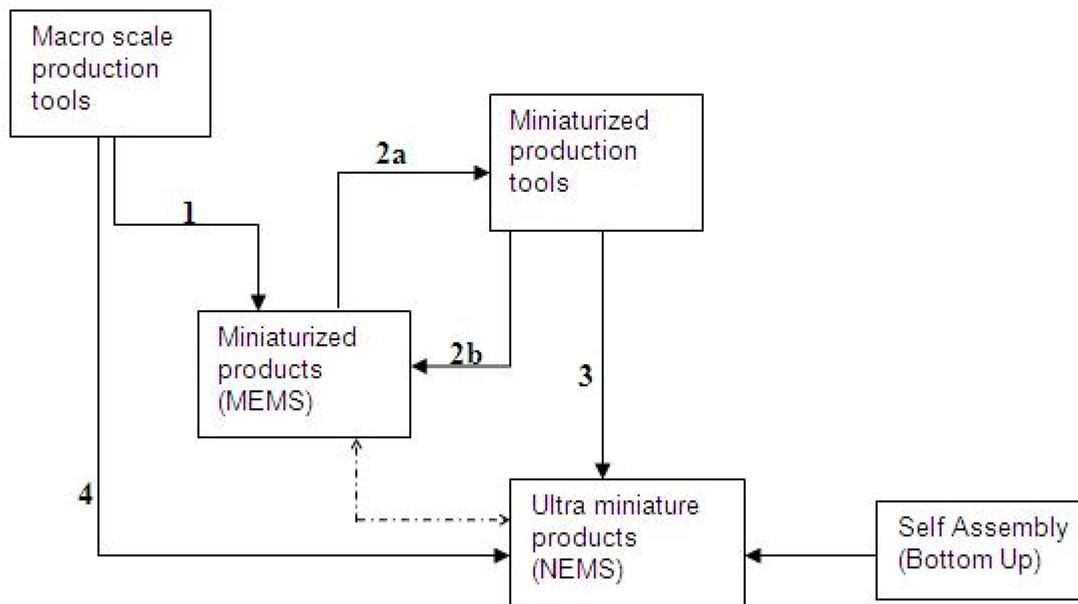

Figure 1.1 Top-Down Micromanufacturing.

Ideally, the production of micro systems should spin off miniature production tools represented by manufacturing type 2a, such as millimeter scale or micron scale positioning and processing systems that lead to cost efficient micro manufacturing shown in the figure as type 2b and nano

manufacturing (type 3) leading to Nano Electro Mechanical Systems (NEMS). However so far, miniaturization of products has not really led to the miniaturization of production equipment.

High precision positioners (robotic manipulators) play a larger role in realizing NEMS. They enable the much required confluence of top down fabrication and assembly with bottom up strategy. In the NEMS context, bottom up technology relates to self assembly of parts that are few nanometers in size into homogenous symmetrical entities. The bottom up strategy can generate high throughput nano patterns in the hundred nanometers scale. The ability to grip and manipulate these patterns into complex 3D and heterogeneous products is very critical to realizing of NEMS. Miniaturizing of positioning equipment can lead to the so called "hybrid assembly" that combines top down with bottom up approaches. An important requirement that remains unexplored is the quantitative analysis of and the means to achieve high throughput in NEMS manufacturing. Current top down manipulators such as Atomic Force Microscopes (AFM) and other Scanning Probe Microscopy (SPM) technologies provide the necessary resolution of motion required for NEMS.

In order to achieve bring nanomanufacturing closer to reality, low cost production and miniaturization of these manipulators is important, which is the essence of micromanufacturing. This motivates the design of millimeter scale (die scale) micro robots that can serve various manufacturing needs of MEMS and NEMS. Fundamental to the successful manufacturing of die scale micro robots is streamlining of the manufacturing process. This includes addressing the following needs:

- Feasible to the production of microrobot configurations that suffice varying mobility, dexterity, precision, force, and bandwidth requirements. Depending on their role, the micro robots may be required to function as articulated manipulators or mobile part carriers.

- Formulating a micromechanical design procedure that incorporates reliable and high yield fabrication and/or assembly process.

- Planning and sequencing assembly and packaging subtasks to successfully accomplish manufacturing.

Thus there is a clear need to view and establish MEMS from a micro and nano manufacturing scenario. A Nano factory can be defined as a combination of tools and processes configured to manufacture nano systems by addressing tradeoffs between throughput, cost, and precision and energy consumption [9-10]. Central to the nano factory infrastructure is tooling, which creates cooperative interaction between available nano manufacturing technologies related to processing, manipulation, and sensing while still addressing product specific requirements. This is illustrated in figure 1.2.

Key constituents of the nano factory tooling are positioning systems that provide the ability to for nano objects to be pushed or pulled, bent, twisted, cut, picked and placed, positioned, oriented, and assembled to form the desired nano patterns, structures, devices and systems. Typical parts that require manipulation are Carbon nanotubes, Silicon nanowires, nano particles and colloids, supra-molecules, etc. A survey of current state-of-the-art in nanomanufacturing shows various tool configurations use Scanning Probe Microscopy (SPM) tools such as the Atomic Force Microscope (AFM) to accomplish these tasks. These tools can also be used as sensors to determine the state of the parts after manipulation.

SPM based nanomanipulation tools has been very successful in providing an opportunity to understand the nano world. However the drawback of using these as nano robots is that they can be cost ineffective and highly serial. For example, AFM's are commonly used for high resolution scanning and manipulation of nano parts. At any given time it can either be used as a sensor or an actuator, thus slowing down the process and it also introduces uncertainty in the assembly operation as the system state could have changed between the two operations. For this reason, the configuration should consist of is configured with independent sensing and manipulation units. Table 1.1 summarizes attributes of these two modules.

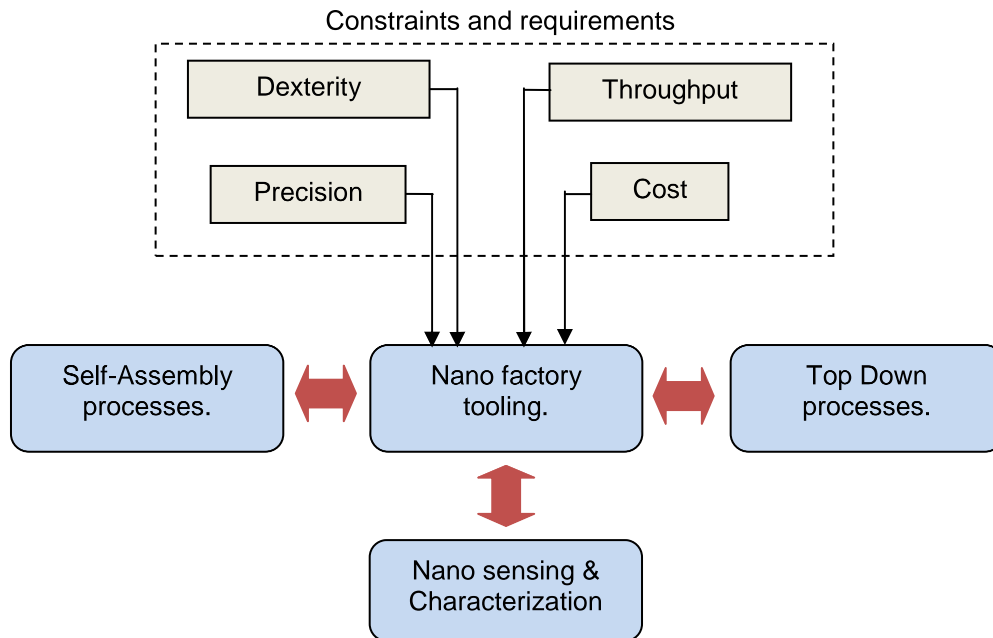

Figure 1.2 Nanofactory planning for Hybrid Nanoassembly.

The manipulation module consists of multiple AFAM micro robots with AFM probe tips attached as end effectors. The ARRIpede micro robot is configured for nano parts/assemblies positioning and locomotion between locomotion modules showed in the figure 1.3 top-right. Figure1. 3 top-left shows a factory on a wafer scenario in which, multiple manipulation modules operate.

Table 1.1 Nano factory scanning and manipulation attributes.

Operation	Scanning	Manipulation
Technique	SPM, SEM	Probing using MEMS robots + SPM
Control	Closed loop (SPM)	Hybrid (open+closed) Open loop using micro robot repeatability or closed loop using SPM tip)
Bandwidth	High	Low
Frequency of tool usage	Intermittent between manipulation steps	Continuous
Sensory	Laser, Electron Beam/ Tunneling current for TEM	Force sensor (designed with micro robot for in-situ sensing)

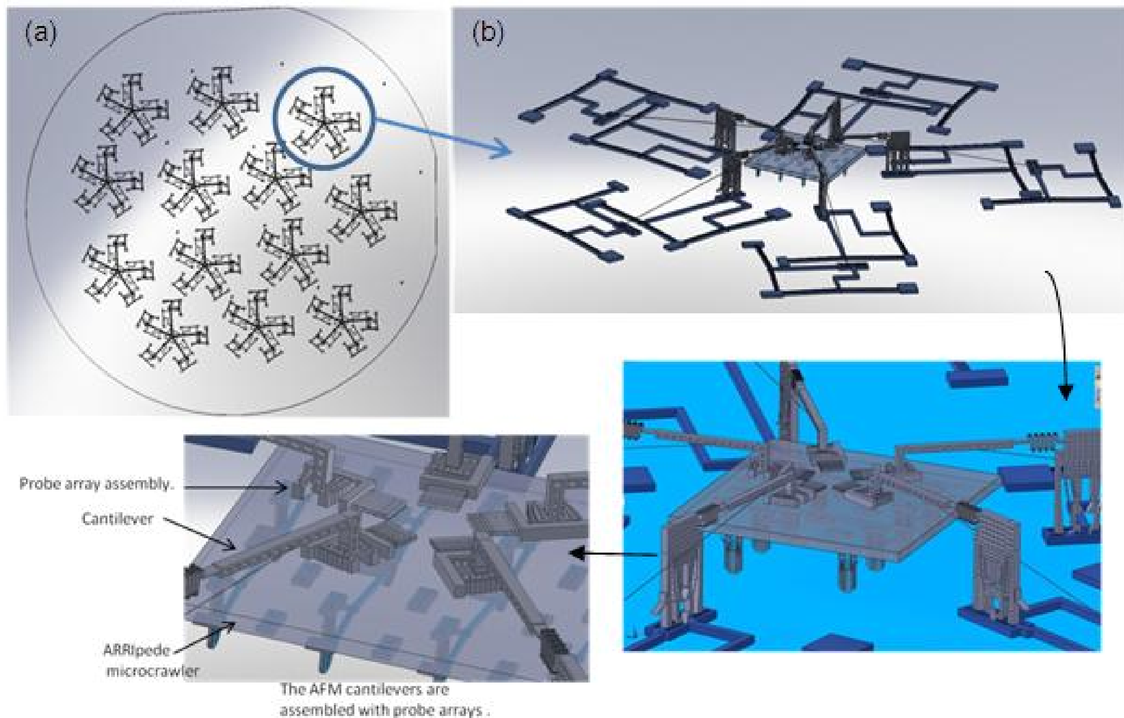

Figure 1.3 Nanofactory concepts. (a) Nanofactory on a 4” wafer (b) Nanomanipulation module.

1.2 Contribution

One of the necessary conditions in extending component/part level micro and nano manufacturing solutions to the system level is the availability of micron to millimeter scale positioners with high positioning precision. In this context, the contributions made by this dissertation are summarized as follows:

- A framework for constructing manufacturable millimeter scale robots. The framework includes *Design for Manufacturing (DFM)* procedure for MEMS robots that aims at satisfying application specific requirements while addressing manufacturing constraints. The DFM framework streamlines microrobot manufacturing and is exemplified using two unique microrobots. A broad outline of the DFM procedure is shown in figure 1.4.

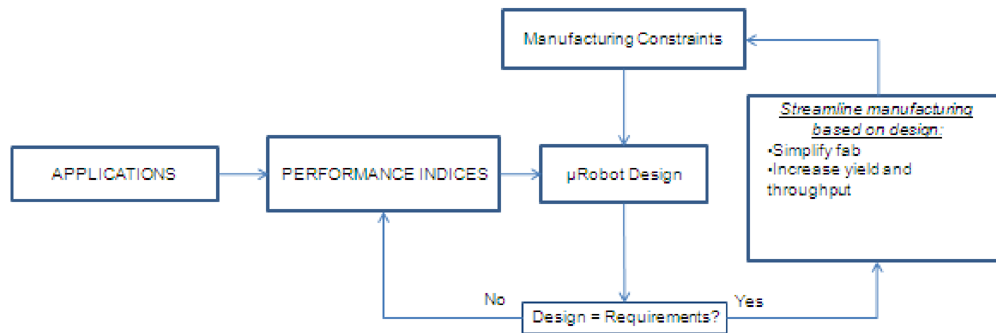

Figure 1.4 Microrobot manufacturing framework.

- The design and implementation of a '*high precision with long range of motion*' mobile MEMS (Micro Electro Mechanical Sytems) robot called the ARRIpede. This microcrawler robot is designed to cover many meters with an on-board power supply while delivering planar repeatability of the order of 5 microns/0.08 degrees. Advances that render this capability are:
  - The design of micro mechanical joints and bonding techniques with high load bearing capability. The resulting ARRIpede can carry upto twice it body weight such as a power supply backpack leading to untethered operation.
  - Design of electrothermal microactuators capable of generating high locomotion forces while still maintaining a footprint within a few hundred microns to few millimeters.
  - A unique power distribution scheme that is used to work around the high power requirement of electrothermal actuators. This dissertation presents a unique way to cycle power between legs that need to be actuated at the same time, leading to the power requirement of one leg at any given time.
  - Microrobot package design to include the successful integration of power electronics backpack with the micro mechanical module, while still limiting the complete unit weight to within the payload capability. The package design is capable of drawing

power from an on-board battery, modulating voltage/current based on the actuator requirements, and generating the necessary gait.

- The design and implementation of a '*dexterous microrobot with true 3D work envelope'* called the AFAM. This microrobot is designed for pick and place nanoassembly, nanomanipulation and nano-characterization applications. The uniqueness of the microrobot design is in the fact that it spans a few mm^3 in volume with a true 3D work envelope (50µm x 50µm x 75µm), positioning repeatability in the hundreds of nanometers and resolution in the tens of nanometers. These specifications are very unique to MEMS based positioners which often have very limited out-of-plane dexterity.

The advances that have enabled this uniqueness can be listed as follows:

  - The design of out-of-plane transmission systems such as cable drives and rigid body mechanisms coupled with bulk micromachined flexural joints that convert in-plane displacement to out of plane motion.
  - The design of assembled joints and bonding techniques that increase joint strength and provide balancing forces/torque when the microrobot is operating.
  - The assembly of Atomic Force Microscope tips onto the microrobot.

The successful miniaturization of high precision tools and robots into the millimeter or micro scale requires addressing multi faceted challenges related to the design, fabrication, assembly, power handling and packaging at the component as well as system level. The contributions made by this dissertation to the existing micromanufacturing knowledge base are:

- Design and fabrication of components for high yield assembly. The variance in part geometry (micromachining tolerance) is identified and the positioning error in the microassembly station is known from past work. Using this information, the micro-snapfastener joints are designed such that their compliance with mating part location is greater than the cumulative sum of positioning error. This ensures higher success in microassembly (leads to high yield).

- Formulation of packaging techniques such as wire bonding and die attach applicable to untethered MEMS robots. Traditional MEMS die attach and wire bonding techniques are unsuitable for assembled MEMS robots.
- An automated die scale assembly and packaging system consisting of off-the-shelf hardware and custom designed software interface is developed. Various open and closed loop control schemes are incorporated and task assignment is accomplished by comparing the tolerance budget and available precision. This dissertation presents qualitative RRA (Resolution, Repeatability and Accuracy) rules used for task assignment amongst available hardware. Inverse kinematics and visual servoing techniques are implemented for MEMS die to package carrier and results are shown.

1.3 Dissertation Outline

This dissertation is organized as follows; Chapter 2 includes background and literature review on micro and nanoscale assembly and manipulation techniques, micro and nanorobots, millimeter scale positioners, and microfactory concepts. A brief account of typical nano scale components such as Carbon Nanotubes (CNT's) is also included.

Chapter 3 presents a framework for manufacturable microrobots including a design for micromanufacturing. This framework streamlines the construction of MEMS microrobots that can be used for micro and nanomanufacturing applications.

Chapter 4 presents details on design of MEMS snapfasteners, joints and other microrobot components, their fabrication and assembly. Using one example of a snapfastener design, the high yield assembly condition is presented and evaluated. Microrobot packaging techniques followed are presented. An overview and system architecture of the M^3, which is a modular reconfigurable die level assembly and packaging system, is described. Using an example, inverse kinematic and visual servoing experiment results are presented.

Chapter 5 presents the ARRIpede concept and its stick-slip based motion principle. Details on electrothermal actuator design and modeling is presented. A static force analysis

employed to determine a rough estimate of the force output is presented followed by a comprehensive dynamical friction model used to simulate the leg displacement for various friction conditions between the leg and the crawling surface. Chapter 4 also includes information on prototype backpack electronics used to regulate the voltage and current inputs from battery and generate the wave gait pattern with high frequency multiplexing of input PWM's. An LQR based controller design, experimental results to measure steering, forward/lateral velocity and positioning repeatability are included.

Chapter 6 presents the AFAM microrobot design including the XY stage and actuator bank, Z stage and the two axes flexure, the out-of-plane transmission design, assembly and a kinematic model of the robot. The microrobot Jacobian is derived to relate actuator inputs to the end effector motion in global frame. Preliminary indentation experiments relating using an assembled AFM tip is presented and the microrobot precision is determined using this nanoindentation data.

Chapter 7 presents conclusion and future work on configuring a nanomanipulation module using the microrobots presented in this dissertation.

CHAPTER 2

BACKGROUND

2.1 Micro and Nanofactories

The current state of the art micromanufacturing technology is capable of producing diverse range of products and is positively exemplified with some highly successful microsystems. However it is commonly observed that the magnitude of time and energy demanded by these micromanufacturing processes are comparable to conventional manufacturing, compromising the promise of low costs and high throughputs that can be achieved. And sometimes, we also encounter mismatch between manufacturing process available and desired materials. Thus, there is a need to re-look top down micromanufacturing in terms of achieving reduced energy consumption and designing easily reconfigurable systems to suit varying product requirements. A Microfactory can be defined as an arrangement of miniaturized production tools that are designed to realize this goal. The overall ambition also includes simplifying micromanufacturing system architecture.

In this context, many teams have researched the microfactory concept and the Mechanical Engineering Laboratory, Ministry of Trade and Industry, Japan, can probably be regarded as the pioneers [11], [12] and [13]. Their concepts date back to the early 1990s with a desktop sized miniature factory consisting of multiple machine tools and manipulators. The toolset includes a Microlathe with spindle speeds going up to 10000rpm and capable of handling minimum part sizes of 60 µm, a micro-mill type machine, a micro-press and microrobots for handling the parts. These tools span two to three orders of magnitude larger than the average size of parts in a typical microsystem. As an example, this microfactory was demonstrated to be capable of machining and assembly of ball bearing components [14]. Other examples include concepts developed by the EU consortium for mass manufacturing of

miniaturized parts, Fraunhofer-Institute for Production Automation, and the Carnegie Mellon University.

A Nanofactory can be defined as a collection of meso and micro production tools applied to the manufacturing of Nano Electro Mechanical Systems (NEMS). This factory represents the confluence of high throughput low complexity bottom up manufacturing with a low~ medium throughput high complexity top down manufacturing at the hundreds of microns scale. The Nanofactory definition presented here is in the light of hybrid nanoassembly and other definitions exist. A nano factory using top-down approach has been envisioned ever since Drexler's book on Nanotechnology [15], however, atomically precise manufacturing is still in the realm of science fiction.

2.2 Micro Robots

Robots have empowered manufacturing since the early 1960's when UnimationTM implemented a 1.5m tall hydraulic manipulator to supply parts to die casting machines. Since then, manipulators have evolved with ever growing application areas such as industrial, medical, human-assistance, recreation, defense, etc [16]. The term micro is prefixed to robotics in many contexts. For example, when manufactured using micro systems technology, when designed for micro assembly or micro manipulation tasks, or when mobile robots are assembled using micro motors. In a broader sense, micro robots span between a few hundred microns to a few millimeters in scale and some popular examples are cited.

Fabricated using Micro Systems Technology (MST), two kinds of MEMS robots have evolved. The first kind carries the more classical anatomy consisting of joints, actuators and on board power source. Multi-legged, cilia-like locomotion using Micro-Electro-Mechanical-Systems (MEMS) have been demonstrated. Examples include a 15x5x1.5mm^3 microrobot with polymide joints that could reach a velocity of 6mm/s [17], a 10x10x0.5 mm^3, 90+ legged crawler though it exhibited payload carrying limitations [18], and a 30x10x1 mm^3, 256-legged walking robot using out of plane thermal actuators, and demonstrated velocities of 1mm/s [19]. A similar out-of

plane walking gait with 8 cilia was proposed in [20] using Ionic Polymer Metal Composite legs. The robot dimensions were larger 6x3x1.5 cm^3, and exhibited a larger payload carrying capacity, but a slower velocity of 0.25mm/s. A thermal actuator based six legged microrobot is presented in [21]. This tethered microrobot can crawl at 0.1mm/s speed, carrying a payload of approximately 3.5g. Recent work at EPFL [22] demonstrated a 1cm x 1cm electrostatic comb drive locomotor with 0.2mm/s velocities, and 16 μW power consumption.

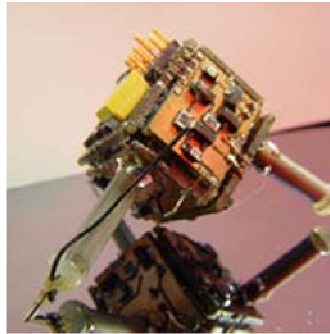

Figure 2.1 Nanowalker Robot [23].

The Nanowalker robot from École Polytechnique of Montreal and MIT [23] is designed for nanoassembly operations. It consists of a tripod like structure with three legs that are piezo driven. The robot spans about 31mm in X and Y and about 33mm in height and houses electronics that drive the piezo and a support bracket for mounting a STM probe tip. The Army Research Laboratory (ARL) have published recent progress in integrating a thin film PZT based in plane actuator coupled to a Si flexure based leg joint [24].

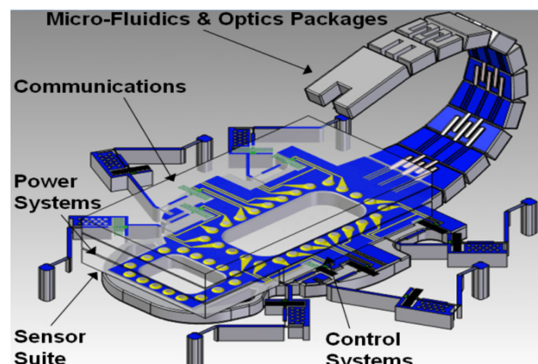

Figure 2.2 Piezo MEMS enabled Millimeter Scale Robot [24].

A magnetic thin film based micro levitation based robot has been proposed by the University of Waterloo [25]. This robot is designed to carry a photo thermal actuation based thermal microgripper. The current robot prototype consists of a bulk magnet with an attached photo thermal gripper. Pair of external electromagnets is used to levitate the robot while a laser beam is focused on the gripper while performing assembly.

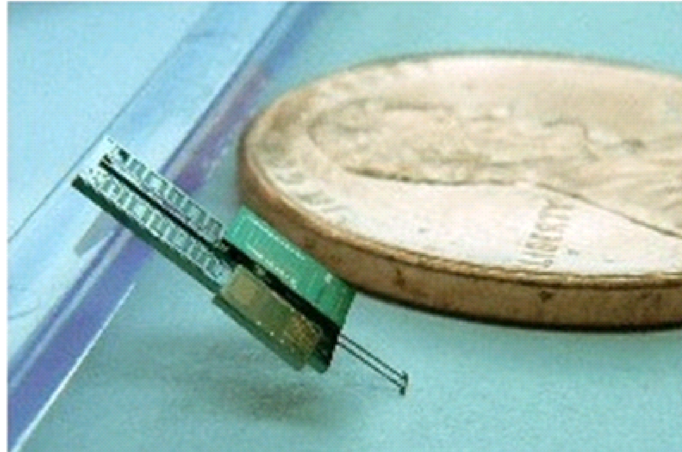

Figure 2.3 Jumping Microrobot [26].

An elastomer *micro rubber-band* has been integrated with electrostatic SOI MEMS in the prototyping of a jumping microrobot [26]. Although locomotion in the form of jumping presents an attractive way to avoid obstacles, jumping with an onboard power source leading to autonomous locomotion and controlling the angle of take off leading to a desired jump trajectory seem to be critical challenges that need to be overcome. The I-Swarm (Intelligent-Small World Autonomous Robots for Micromanipulation) consists of a swarm of tripod style solar powered micro robot driven by piezoelectric actuators [27]. An application specific Integrated Circuit (ASIC) is used to provide a low weight and efficient means to power the polymer piezo actuators.

The second category includes a new classes of micro robots with sub-mm dimensions. These robots span tens to a few hundred microns in size and are driven using external force fields. One example is a 300μm x 300μm robot driven by magnetic force fields [28]. The robot

consists of two soft paramagnets made of nickel. Steering is achieved by balancing the force of attraction between the two soft magnets and by resonating one that is attached to a spring. Another example of a magnetically driven microrobot is a Neodymium Boron Iron based permanent magnet cut to 250x130x50μm^3 [29]. An electrostatic scratch drive based microrobot [30] spans 60x25x10 μm^3. These microrobots carry applications in nano manufacturing and drug delivery.

A wide variety of autonomous mobile robots have been developed over the years for surveillance and combat applications, exhibiting various forms of locomotion such as rolling, walking, climbing, crawling, jumping and flying. Among them, walking and crawling inspired by biology have been routinely employed on mobile robots of all sizes [31]. Micro autonomous vehicles (MAVs) are drawing more attention recently for various urban and military applications such as reconnaissance and surveillance, search and rescue, detection of biological and chemical materials, etc. [32]. The "RoACH" is an autonomous 2.4g crawling hexapod robot [33]. Powered using shape memory alloy based actuators, this robot can crawl one body length per second or approximately 3cms/sec. The Harvard fly [34] and the Micro Mechanical Flying Insect (MMFI) [35] are piezoelectric actuator based flyers. Both consist of ultra-light weight laser micro machined chassis integrated with flexural joints. The Geckobot is a dry adhesion based crawler inspired from Gecko's ability to climb very smooth vertical walls. Nanoscopic hair like polymer fibers are fabricated and stalked to produce Van der Waals force [36].

2.3 MEMS positioners

Over the past two decades, with the advent of microsystems and nanotechnology, precision requirements for robot manipulators have increased considerably. Precision robots are invaluable tools for micro and nano manipulation [37-38], automated and teleoperated assembly [39]. Typical top-down micro and nano assembly hardware use precision robots and end-effectors that are still many orders of magnitude larger than the size of the parts they

manipulate [40]. With advances in Micro Electro Mechanical Systems (MEMS), new types of positioning stages have been proposed to aid nanoscale manipulation, probing and force measurement, optical microsystems, and high density data storage devices [41-42]. The design of such positioners must balance key performance parameters such as range of motion, force output/payload capacity, and dexterity (degrees of freedom).

A popular example of monolithically fabricated micropositioners is actuated using electrostatic comb-drives [41]. As a result, they have limited out-of-plane displacement outputs (e.g. mostly planar dexterity) [42]. Other examples include atomic force microscope (AFM) tips, which mostly operate along a single vertical direction [43]. On the other hand, positioners with more than 3 degrees of freedom have been fabricated using thin-film deposition and etching, but they have limited force outputs, payload capacities, and reliability to operate as independent micromanipulators [44]. In order to overcome these inherent trade-offs, micro-positioners have been used as grippers or force probes in conjunction with larger conventional positioning stages, and therefore the overall dimensions of the manipulator spans several inches. This is a severe limitation in applications requiring multiple such positioners within confined volumes, for example inside a scanning electron microscope (SEM) chamber.

2.4 Microassembly and Manipulation

Many of the MEMS devices being developed are fabricated using surface micromachining, which is adapted from IC fabrication technology. Surface micromachining is basically the serial growth and/or removal of sacrificial thin films. Due to the use of thin film fabrication techniques, the MEMS parts that are created are relatively thin, in comparison with their length and width. Examples of thin film MEMS fabrication techniques are poly MUMPS ® and SUMMIT V ®, with the number of layers ranging between 3 and 5. Although this technique leads to MEMS parts that are “released” to move in the final stages of the fabrication process, their motion range is restricted. Additionally, their cross section is thin and leads to weak joints. A greater limitation lies with the inability to integrate materials that are fabrication incompatible.

All of these limitations affect the variety of products that can be fabricated and can be overcome by incorporating microassembly into the micromanufacturing process. Microassembly refers to the post-fabrication manipulation and joining of parts typically ranging between a few microns upto 1mm in size. Figure 2.4 shows three approaches to microassembly from a throughput standpoint. The three techniques are serial, parallel, and exponential. Serial microassembly involves using micromanipulators and grippers on individual components and serially altering their position and orientation from the substrate onto the final point of assembly. The manipulators or grippers can be passive such as probes and jammers or active open/close type mechanisms such as tweezers or MEMS actuator based grippers [45-46].

Parallel microassembly refers to the simultaneous assembly of more than one part. The intention behind this technique is to maximize assembly throughputs. Referring to figure 2.4, parallel microassembly can be distinguished into deterministic and stochastic types, depending on whether the exact trajectory of mating parts can be predicted or not. Deterministic parallel microassembly can be achieved using arrays of probes or microgrippers or using flip chip die ~ die or wafer ~ wafer part transfer [47-48]. Stochastic parallel microassembly can be achieved by subjecting an array of parts to a global force field such as vibrations and fluidic agitation [49-51]. During this process the parts undergo repositioning and reorientation from their original state, reach the desired mating point and bond to the mating part.

Parallel microassembly can lead to high throughput, however the assembly yield can be very low. Robotic top-down deterministic serial and parallel microassembly has been explored using high precision positioners and vision feedback [52-55]. Vision-based feedback is a very popular choice due to the availability of sub-micron resolution and high resolution CCD’s. Force sensing based approaches can be used for in-situ measurements and can provide precise information about contact between surfaces [56-57].

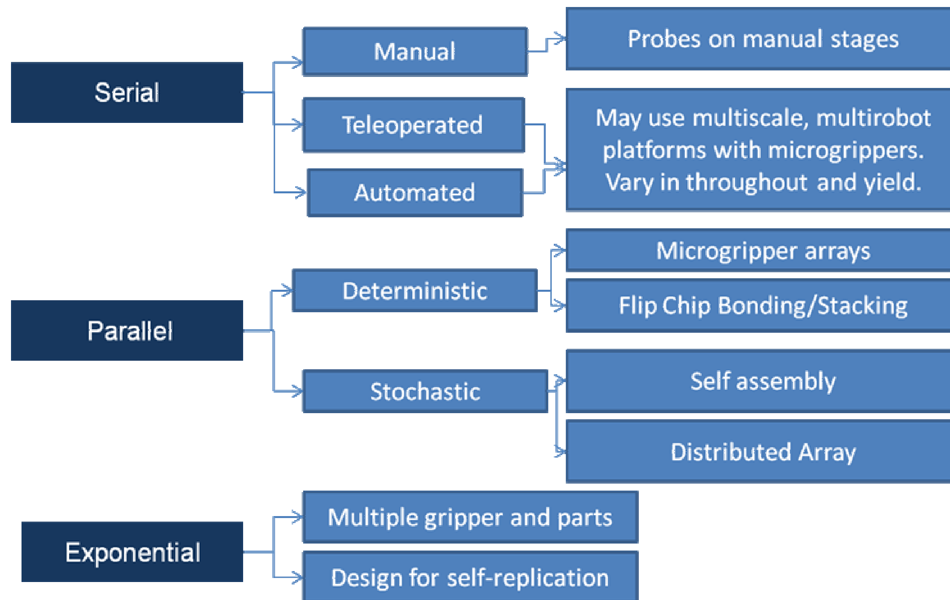

Figure 2.4 Microassembly techniques.

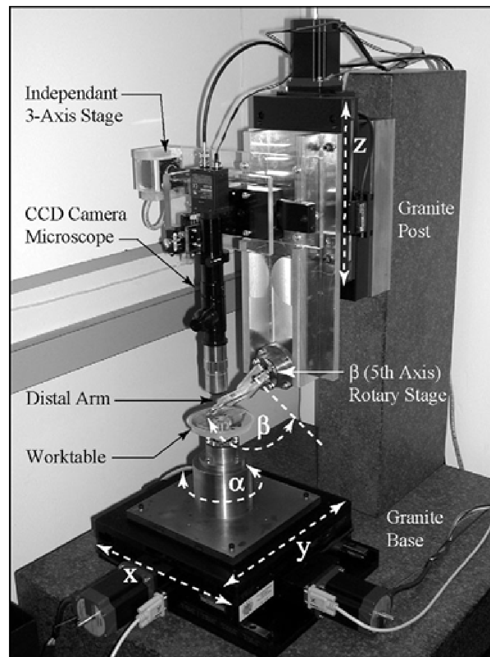

Figure 2.5 Microassembly Station at the University of Toronto [58].

Top down microassembly refers to the use of a multi-scale system consisting of macro or meso scale robots operating upon and assembling micro scale parts. There are many examples of such microassembly platforms and some of them are presented here. A five axis robotic manipulator, named the MJMP (Manipulator and Joiner of Micro Parts) has been developed by the University of Toronto [58] as a microassembly workstation, shown in figure 2. 5. The robotic manipulator consists of a MEMS gripper bonded at its distal end using solder bonding. The microgrippers span 1.5mm x 0.6mm in area.

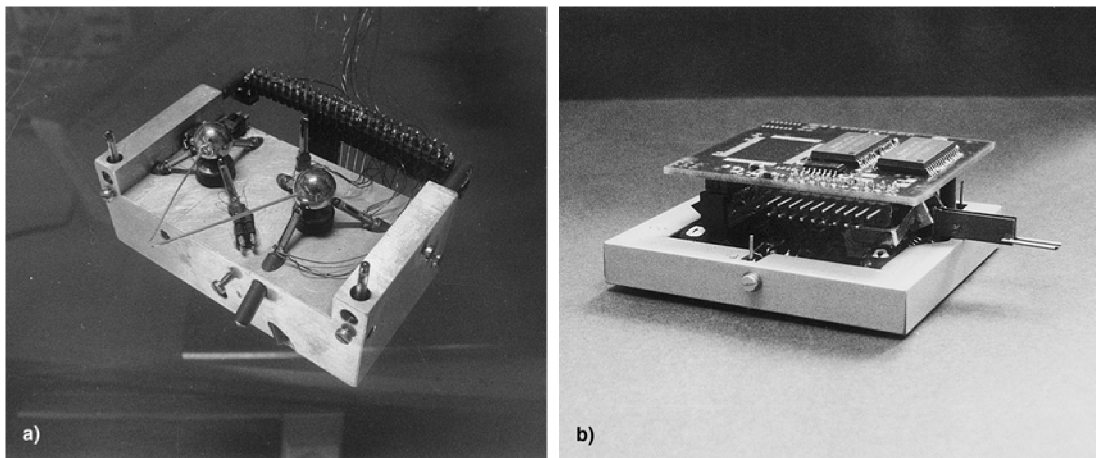

Figure 2.6 Microassembly Station at the University of Oldenburg [62].

An automated microrobot based microassembly desktop station (MMS) has been developed at the University of Oldenburg [59]. This system was designed to perform assembly and also enable testing /measurement of the assembled microsystem. This platform consists of piezo based micromanipulation and positioning units for coordinated assembly operations. The two robots called MINIMAN and SPIDER, are shown in Fig. 2.6(a and b). The SPIDER (Fig. 6b) employs bimorph piezoactuators for gripping and includes six piezolegs.

2.5 Nanoassembly and Manipulation

Nanoassembly refers to the assembly of components with part sizes ranging between a few nanometers to a few hundred nanometers and is one of the key disciplines in nanotechnology [60].

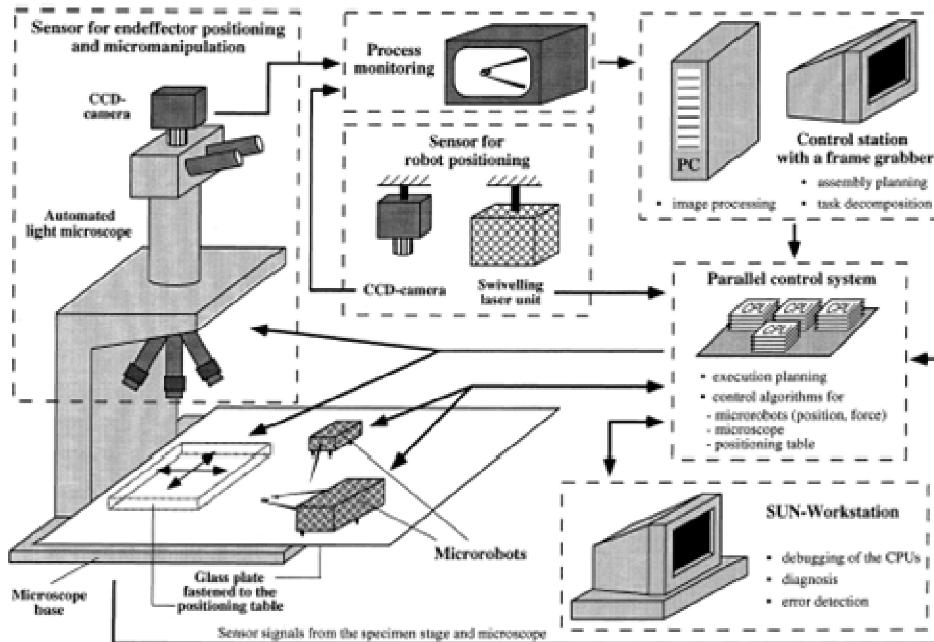

Figure 2.7 Microrobot based Microassembly [59].

There are many nanoassembly techniques that have been developed in the last two decades and they are broadly classified into self assembly (bottom-up) and top-down categories. Self assembly often refers to the assembly of units such as molecules and mono-layers. A popular example is the self-assembled monolayers (SAMs). A self assembled monolayer (SAM) consists of a layer of amphiphilic molecules in which one end of the molecule shows a special affinity to the substrate. The tail end consists of a functional group and can be used to modify the properties of the surface. This characteristic is often used in NEMS design. A disadvantage while using self-nanoassembly is that it is difficult or impossible in many cases to produce complex designed and interconnected patterns or structures. [61-64]. The assemblies in many cases form symmetrical structures.

Top down robotic nanoassembly refers to the controlled manipulation, handling and assembly of nano objects by robots. As with the case with microassembly, this technique can

be employed to manufacture new nano patterns, structures, devices and systems with nanoscale accuracy [65-70]. Due to the size of these robots being many orders of magnitude larger than the parts, this approach is called top-down.

Nanoassembly was famously proposed by Richard Feynman in 1959, in his lecture, “There’s Plenty of Room at the Bottom,” which is considered by many to be starting point for nanotechnology [71]. Drexler [72] proposed nanomanufacturing using self-replicative molecular assemblers In his concept, Drexler proposed creating molecular machines called assemblers, that are able to build a wide range of useful products as well as copies of themselves (self-replication). The invention of the scanning tunneling microscope (STM) was the first step along the road to technologies able to act at the level of individual atoms, which allows scientists to view and manipulate nano particles directly [73-74]. The success of the STM also led to the development of other scanning probe microscopes (SPMs), including the atomic force microscope (AFM) [75]. They can also be used to create nanostructures or move individual nano objects from place to place. The AFM is often used by scientists to perform nanomanipulation and nanocharacterization. This tool offers molecular scale precision under stable conditions. An example is the Veeco’s ICON ® system, which is an AFM system for direct nanoscale manipulation, nanolithography and imaging [76]. In recent years, SPMs are increasingly being used for nanolithography and patterning [77-80]. The first demo from IBM positioned Xenon atoms in the IBM logo formation and is a popular example of the system capability. SPM brings molecular level capability leading to the possible creation of new materials and tailoring of key properties of available materials [80-81]. The drawbacks however include the serial operation of nanoparts and the fact that at any given time, these tools can be used either for scanning or manipulation. This has lead to reduced throughput in nanomanufacturing. Other problems are specific to the presence of dominant surface forces which result in positioning uncertainty. Compared with gravitational forces, surface forces are

much stronger in the nano world leading to uncertainty in releasing a gripped object. This has led to specialized nano gripper and probe design and specialized handling strategies [82-86].

2.6 Nanorobots

Nanorobots referred to in this dissertation are defined as systems capable of nanomanipulation, i.e. systems that can manipulate nanometer size objects with a nanometer size end effector and nano to sub nano meter precision. Positioners or manipulators that render this ability are often many orders of magnitudes larger than the nanometer. The Atomic Force Microscopes probes and the Scanning Tunneling Microscopes are the most widely used nanomanipulators as they provide a means to both manipulate and sense at the nanoscale.

As described in section 2.6, the atomic force microscope (AFM) belonging to the scanning probe microscopy (SPM) based tool family enables nanomanipulation and also supports a wide range of characterization capabilities at the nanometer scale. Thus it has single handedly enabled sensing and manipulation at these scales [87]. These systems can be operated in teleoperated or preprogrammed open-loop fashion with real time modification of the SPM tip and feedback parameters during operation. An AFM typically operates in one of two modes, contact mode or tapping mode. Contact mode is where the tip scrapes along the surface. Tapping mode oscillates the tip at its resonant frequency and includes intermittent contact with the surface. Thus, it does not scratch the substrate as much as contact mode and provides damage-free scanning on more surfaces with extended life of the scanning tip. Continuing the discussion presented in section 2.6, the AFM has the limitation of either being able to sense or manipulate at any given instance. To work-around the problem, the Scanning Electron Microscopy (SEM) can been used as a sensor for surface characterization and imaging applications. However, the scanning rate at very high resolutions can be serious drawback along with the fact that the samples have to conductive in nature. Additionally, the e-beam is also incapable of manipulation. None the less, a combination of the SEM with an AFM does enable parallel manipulation and sensing during nanomanipulation. An example of a

nanorobotic setup that uses the SEM + AFM combination is shown in figure 2.8. This setup is described in [88] and is ongoing work at the Fukuda Lab at Nagoya University, Japan. The setup consists of a nanorobotic manipulation system, a SEM based sensing system, an AFM and a nanofabrication system based on electron-beam-induced deposition (EBID). This setup has been successfully employed to manipulate and assemble CNT (Carbon Nanotubes) and conduct in situ analysis of nanomaterials.

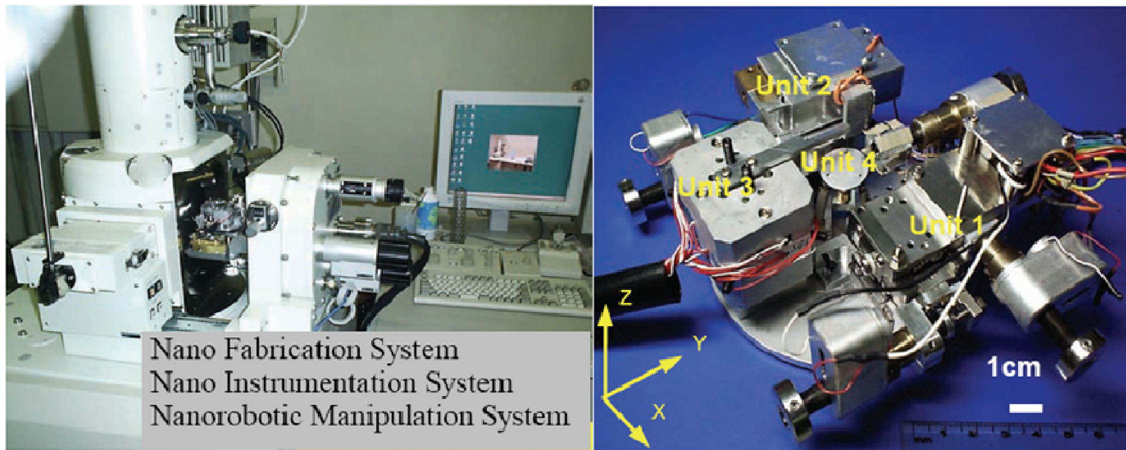

Figure 2.8 Fukuda Lab Nanomanipulation Cell [88].

A tele-nanorobotics system using an Atomic Force Microscope as the nanorobot has been proposed in [89].

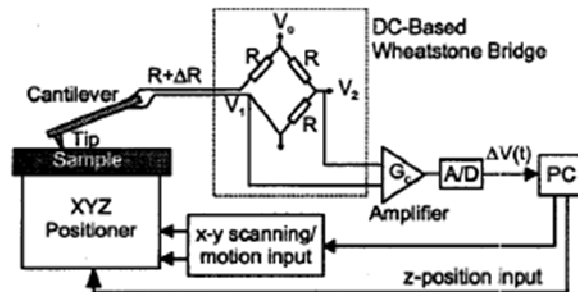

Figure 2.9 Teleoperated nanorobotics system [89].

This work presents modeling and control of the AFM cantilever, and a 3D Virtual Reality visual feedback interface using a haptic device. A piezoresistive cantilever connected to a

Wheatstone bridge shown in figure 2.9 is employed in place of the more commonly used laser sensor.

Zyvex Corporation has developed a versatile platform technology for nanomanipulation, nanometrology, and nanoassembly applications shown in figure 2.10. This system consists of coarse positioning axes with 12 mm range of travel and 100 nm precision coupled to fine positioning axes with up to 60 micron range of travel and 5 nm precision[90]. This system can be reconfigured using quick-changeable end-effectors including nano probes and microgrippers. This systems supports up to four independent positioners thus providing the ability to operate four end-effectors to within 5nm of a desired location.

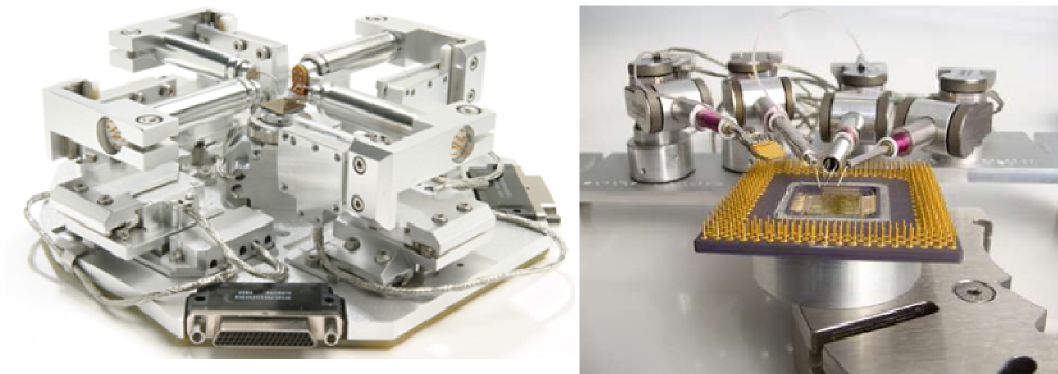

Figure 2.10 (Left) Zyvex Nanomanipulation Setup [90]; (Right) Kleindiek Manipulators [91].

Positioning of CNT’s and other nanoparts using a nanorobotic setup consisting of Kleindiek Manipulators is shown in figure 2.10(right) and described in [91]. This setup consists of Kleindiek Manipulators used for controlled positioning of nanowires and study on the suitability of their use as NEMS.

CHAPTER 3

A FRAMEWORK TOWARDS MANUFACTURABLE MICROROBOTS

3.1 MEMS or not?

Over the past two decades, robotics and microsystems technology have interweaved in many ways leading to some fantastic applications such as atomically precise manipulators, drug delivering microrobots, rugged mobile units for defense, etc. From literature review presented in section 2.2, it is clear that miniaturization of robots can be achieved even without the utilization of MEMS. While such microrobots represent embodiments of miniaturization, MEMS based robots offer two distinct several advantages for applications in micro and nanomanufacturing:

- Scaling: MEMS robots can be scaled down to span a few hundred microns to few mm^3. This is an advantageous because multi-robot based manufacturing is required at the micro/nano scales.
- Precision: Microactuators offer nanometer scale positioning resolution.

Due to these advantages, MEMS was selected as the miniaturization pathway in this dissertation.

3.2 Framework Description

From the microrobotics literature review presented in section 2.2, it is evident that many teams have pursued developing MEMS robots. The present state of the art in MEMS presents many types of actuators such as piezoelectric, SMA etc., fabrication techniques producing thin films and high aspect ratio structures out of various materials, and many approaches to assembly and system integration. A miniaturized high throughput micro and nanomanufacturing setup will consist of multiple instances of MEMS robots built to perform various functions. This suggests the need to formulate a framework streamlining the design and the manufacturing

processes leading to high volume and reliable manufacturing of these robots. This framework is presented as a design for manufacturing (DFM) procedure and is exemplified in the remainder of the document.

3.2.1 Design for Manufacturing

The framework presented in this section assumes the following details:

- Target systems are MEMS robots with applications in micro and nanomanufacturing alone.
- The overall approach towards manufacturing them is limited to the top-down type.

Some definitions used in the framework are:

- Performance Indices (PI): These are specifications demanded by the application. Examples: Bandwidth, payload, etc.
- Constraints: Limitations in achievable specifications imposed by the fabrication, assembly, packaging and testing related processes. Examples: Aspect ratio, minimum part size, etc.

The design for manufacturing framework is outlined in figure 3.1. As seen in the figure, the framework is divided into sub-modules, which are described as follows:

3.2.1.1 Component level design for performance

This is the first phase in designing the microrobot. In this step, performance indices (PI) arising from the application on hand are compared with a database consisting information on actuation types, joints and transmission types, and materials resulting in the design of microrobot building blocks. PI related to actuator design are the bandwidth, power density, strain, resolution, and force output. PI related to design of joints are work volume, payload, and the bandwidth. Constraints acting during this phase result from the fabrication technology that can be employed to create these components. Parts can be made of differing materials based on their respective PI. For example, actuators can be made of a ceramic material such as PZT in order to satisfy the high bandwidth PI while the joints can be bulk micromachined Si resulting

in high strength joints. Integration of components from varying materials is handled during the component design for manufacturing phase described in section 3.2.1.2, during which techniques such as assembly and bonding are adopted. Following actuator design, the number of actuators and their arrangement leading to a preliminary substrate design is accomplished to address PI such as required work volume, payload, and target microrobot size.

3.2.1.2 Component level design for manufacturing

Following the design of components that satisfy application specifications, the designs are modified to suit post fabrication operations such as assembly and packaging. Actuators and joint/transmission components may need to be assembled to achieve the following constraints:

- Integrate components whose fabrication processes are not compatible.
- Form unique joint designs that cannot be accomplished using fabrication alone.

In order to be 'assemblable', the components are redesigned to suit the assembly techniques followed. Top down assembly can be very broadly classified into active and passive types based on the gripping technique. Passive assembly requires a compliant regime to be included in the part design, while active gripping requires a rigid region suitable for gripping. Figure 3.2 (b, c) show component design with a compliant regime for gripping. Similarly, actuators are redesigned to accommodate assembled joints. Packaging at the component level refers to the design of electrical interconnects in order to establish power supply from an external power source and to route sensor signals via the component. Actuators designs are thus, further modified to accommodate these interconnects. Figure 3.2 (d) shows an electrothermal actuator wire bonded to an external power supply. The component level design update results in an updated substrate level design.

3.2.1.3 System level design updates

During this phase, constraints arise due to the fact that all microrobot components come together and design is modified as per a system level assembly and packaging plan. This plan includes a sequence of the following operations:

- Part pick and place using microgrippers to form serial or parallel array of joints.
- Parts/joints bonding using epoxy to increase mechanical strength.
- Solder reflow to form interconnects.via joints.
- Integration of electronics and micromechanical modules using mechanical bonding and Formation of electrical interconnects.

The sequence of these assembly and packaging operations depend on the top down manufacturing system configuration, and on details that are intricate to the microrobot design. For example, the assembly of micromechanical components on substrate prior to its integration with the electronics module is preferred due to fixturing challenges that arise at the microassembly station due to the presence of the electronics module with the substrate. Also, as seen from figures 3.2 a-b, the dimensions of the end-effector play a very critical role in the resulting dimensions of the microrobot. The clearance required to accommodate the gripper during assembly packaging operations are taken into consideration during this design phase. The result is an updated microrobot design with the package. Following this phase, the final design is compared to the PI.

3.2.1.4 Process improvement loop

This process improvement phase is aimed at making improvements to the process involved in the micromanufacturing framework described trough sections 3.2.1.1~3.2.1.3. This includes the following operations:

- *Minimize fabrication complexity:* It is always desirable to keep the fabrication process used in the production of components as simple as we possible can. The use of simple fabrication techniques can lead to reduced production cost and higher yield in fabrication.
- *Use batch fabrication techniques:* The possibility of adapting a batch fabrication process is investigated to achieve higher throughputs.
- *Design for high yield assembly and packaging.*

- *Package scaling:* The microrobot packaging that consists of structural and electrical interconnects, power electronics and signal conditioning, and possibly an on-board power source can be improved in order to reduce payload, system reliability and reduce the complexity involved in their manufacturing.

3.3 Microrobot Performance Indices

Drawing parallels from conventional manufacturing, micromanufacturing offers two roles for robots; mobile unit for part positioning and articulated manipulator arms for assembly. In this section, the requirements imposed by relevant applications are drawn. These requirements are referenced for decision making in the framework.

3.3.1 Mobile Microrobot

- These microrobots are used to convey parts in and out of a assembly cell and also participate in the process (manipulation, assembly, bonding etc.). The design requirements drawn from these requirements are:
- Payload: The payload carried by the microrobot is sub-categorized into backpack and locomotion modules. The backpack module consists of power, control, and communication electronics, a battery for autonomous operation, and the process substrate.

The weight of the backpack payload typically varied between 0.5g ~3g. On the lower end of that range are ASIC designs [23,33] designed specifically for the microrobot design and towards the middle and higher end are discrete SMD type PCB’s [21]. Li-Poly batteries such as the Full-River ® offer high current discharge (~300mA) at modest power ratings (20~30mA-h)

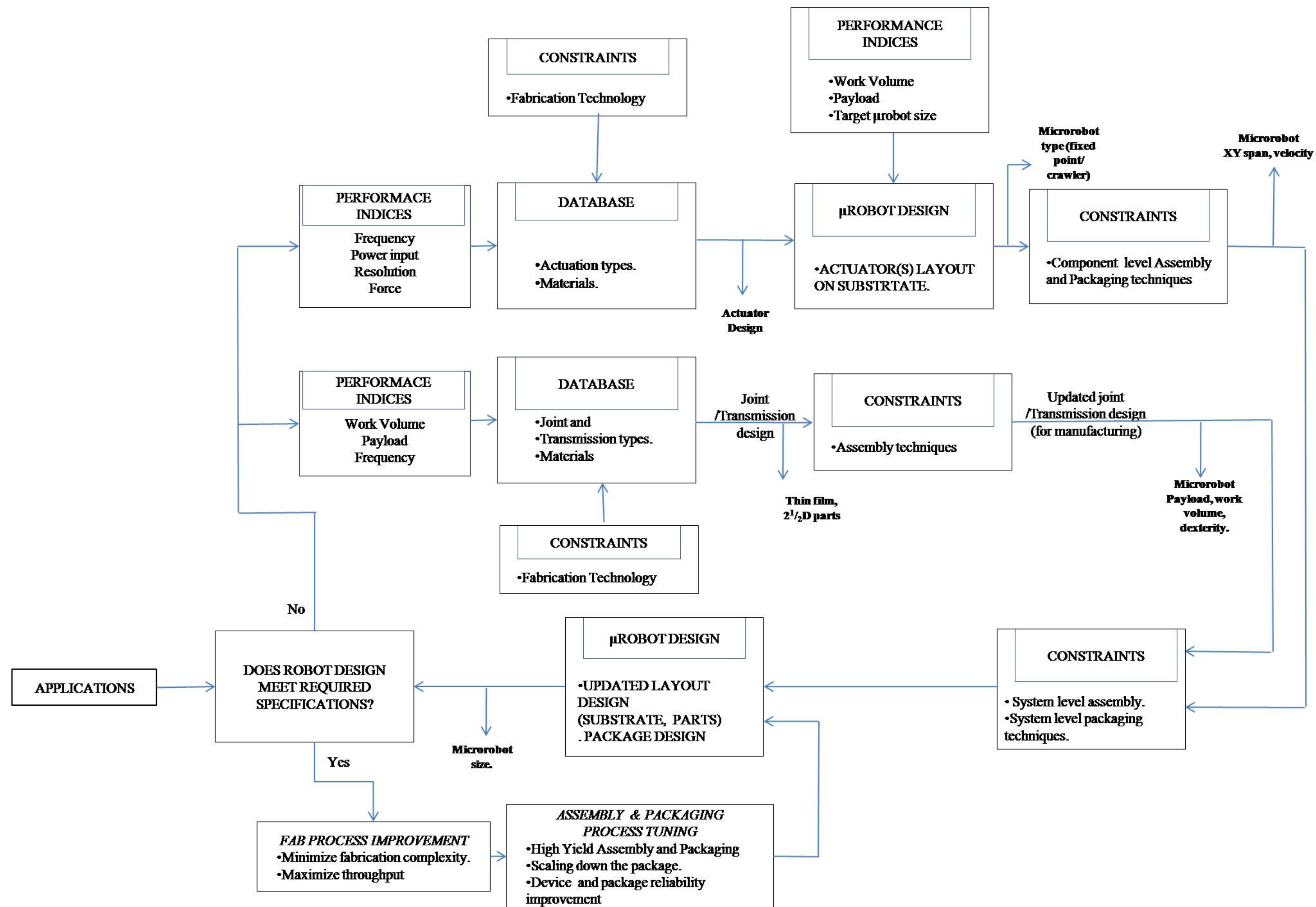

Figure 3.1 Design for Micromanufacturing Robots

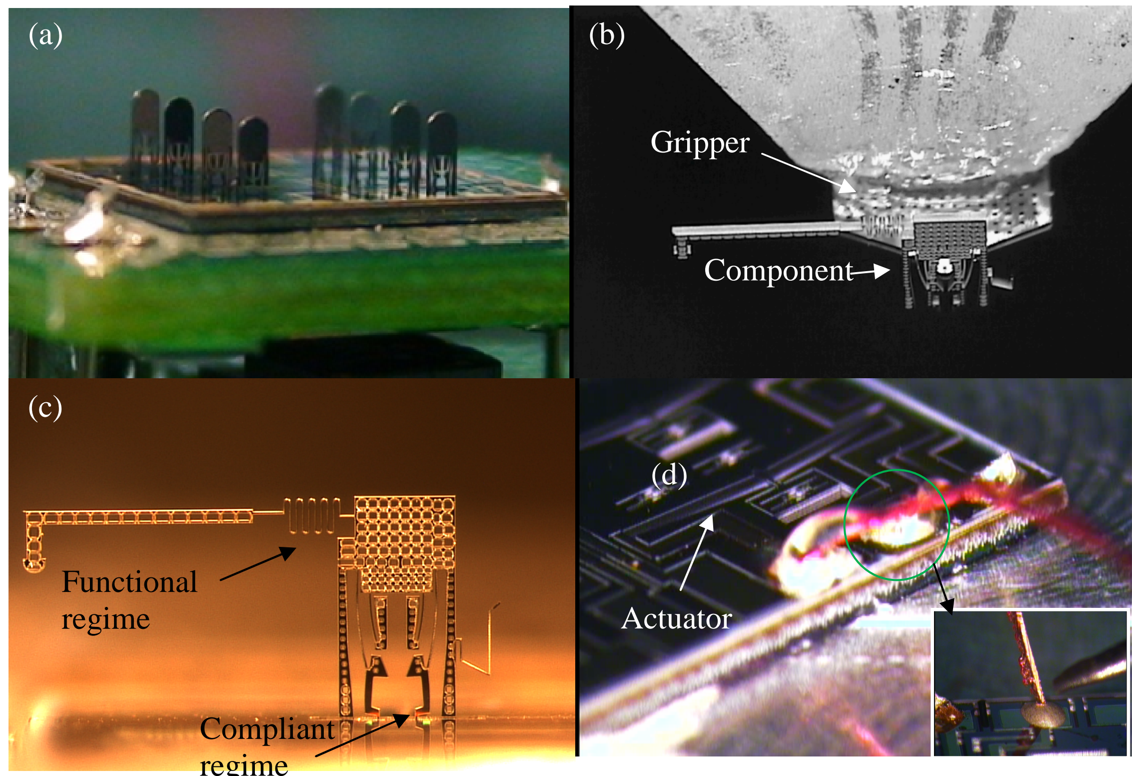

Figure 3.2 Microrobot design examples (a) Multiple assembly instances; (b) Component with passive gripper; (c) Assembled component; (d) Electrical interconnect

and weigh close to 1g. The process substrates conveyed are MEMS substrates typically weighing between 1~1.5g. This takes the backpack weight adds upto 5.5g. The locomotion module consists of micromechanical actuators, joints, wire-bonds, die attach solder used to interface with the electronics adding up to 1.5g. Thus, the total payload adds up to 7g and this is set as one of the requirements.

- Precision: This requirement is bound by tolerance budgets offered during microassembly (1~50 microns) and nanoassembly (30~100 nanometers) operations. Typical piezo MEMS actuators are capable of sub-nanometer motion resolution while electrostatic and electrothermal types offer 5~10 nanometers. While this is the capability of the actuator itself, the addition of motion transmission systems, end-effectors, payload etc., lead to loss in precision. Design for controllability, and implementing closed loop control results in improved precision. This leads to the

minimum required precision metrics which are resolution ranging between 30~100 microns and repeatability ranging between 1~50 microns.

- Volume: The XY footprint of the microrobot should be minimized to approach the maximum size of the workpiece (substrate) conveyed during assembly operation. Typical MEMS die sizes range between 5~10mm. The maximum Z constraint is based on the room available in typical working environments such as inside an Atomic Force Microscope (~1.5cms). Thus the target volume for the microrobot is 10x10x15mm^3.
- Dexterity: A minimum of three degrees of freedom (XYθ) are required for planar mobility. Most MEMS actuators undergo prismatic or almost prismatic strain. Thus, a first choice in configuration would be to actuate an array of actuators with legs to form a dynamic stick slip vector field. Configuring flying or jumping microrobots is deemed unnecessary at this stage.
- Velocity and range of motion: The work area is typically bounded by that of a 6" wafer loaded on a Scanning Electron Microscope or Atomic Force Microscope. Hence the microrobot should be capable of velocities of atleast a few mm/s.

3.3.2 Articulated Arm

Contrary to the mobile microrobot, an articulated manipulator type microrobot poses stringent requirements on operating precision and dexterity. Some of the specifications drawn to streamline construction of this microrobot type are listed.

- Precision: With parallel manipulation of typical nanoparts such as CNT's as the primary intention, this microrobot type is required to demonstrate open loop repeatability ranging between 50~100 nanometers (typical part size range) and a minimum resolution of 20~30nm. Other applications such as serial nanomanipulation, sensing, and nanoindentation applications demand lower precision levels.
- Dexterity: Successful nanomanipulation required true 3D work volume (XYZ). Thus a minimum of three degrees of freedom are required.

- Work Envelope: Since these microrobots are primarily intended to be used in conjunction with an AFM scanner, their work envelopes need to match. Thus, a desired work envelope is a volume is set as 50 x 50 x 50 μm^3.
- Bandwidth: The microrobot should be capable of operating a single probe tip as an end-effector with a mechanical bandwidth of 100-150 Hz, and an array of probes with a bandwidth of several hundred Hz.
- Force and torque requirements: While producing manipulating forces of atleast a 2 mN along the out of plane axis for nanoindentation applications, the manipulator transmission and joints should provide resisting torque of upto between 0.1~1N-m^2/rad depending on the application on hand.

3.4 Actuation Technology

Popular MEMS actuators types are based on electrostatic, electrothermal, piezoelectric, electromagnetic, and shape memory effects. These actuators have varying strain, force, power, area/volume and efficiency specifications coupled with variations in ease of fabrication and integration with interfacing modules such as electronics.

Table 3.1 shows a comparative study of MEMS actuators. From this table, it is evident that electrostatic and piezoelectric actuators offer higher power densities which is favorable for autonomous locomotion.

3.4.1 Figure of Merit

Electrothermal actuators consume the highest power due to the low efficiency joule heating based strain used for actuation. From manufacturability perspective, fabricating and integrating piezoelectric or electromagnetic actuators involves painstaking and elaborate processes. Electrostatic and electrothermal actuators are compatible with Si based single mask batch fabrication processes.

Table 3.1 Comparison of actuation techniques.

Actuation Technique	Force scale	Displacement range	Power Required	Frequency of operation	Fabrication/ Integration
Piezoelectric (thin films)	E+01μN	Few μm (<10μm)	Low (High Voltage)	E+03Hz	Very difficult
Electrostatic (bulk)	E+02μN	E+1μm	Low (High Voltage)	E+03Hz	Easy
Electrothermal (bulk)	E+01mN	E+1μm	High (High Current)	E+01Hz	Easy
Electromagnetic	E+02μN	Few μm (<10μm)	Low	E+02Hz	Difficult
SMA (NiTi)	E+02μN	Few μm (<10μm)	High	Few Hz (<10Hz)	Difficult

Ease of fabrication and compatibility with other down-stream processes such as assembly and packaging are the biggest challenges faced by PZT based thin film actuators. Electrothermal actuators provide the highest combined force output and strain amongst all, closely followed by electrostatic actuators which occupy a larger foot print on the substrate. A figure of merit is defined as:

$$\eta = F.O.M = \frac{WorkDensity \times Bandwidth \times .Strain}{Size} \tag{3.1}$$

Table 3.2 shows the 'η' for the actuator types listed in table 3.1. From this table, bulk micro machined electrothermal and electrostatic actuators offer a high figure of merit combined with relatively easy fabrication techniques and good compatibility with other MEMS components. For these reasons, they are good candidates for constructing microrobots.

3.4.2 Actuation Force Requirement

Based on the conclusions drawn in section 3.2.1, a microcrawler with stick-slip motion is the first choice in design. A static force condition is set up to roughly estimate the magnitude and range of actuation forces required for the mobile microrobot locomotion.

Table 3.2 Figure of Merit.

	Strain (%)	Size (mm^3)	Bandwidth (Hz)	Work Density (J/mm^3)	FOM (Normalized)
Piezoelectric (thin films)	0.75	2.5	2.0E+03	1.2E-4	0.72
Electrostatic (bulk)	2	1.0	1.0E+03	1.8E-4	3.6
Electrothermal (bulk)	5	0.2	100	1.0E-4	2.5
Electromagnetic	0.2	10	1.0E+3	4.0E-4	0.08
SMA (NiTi)	2	5	3~5	5.0E-3	0.1

$$Nf_{act} < \frac{(N+P)\mu_s Wg}{(N+P)} = \mu_s Wg, \tag{3.2}$$

$$Nf_{act} > \frac{P\mu_s Wg}{(N+P)}, \tag{3.3}$$

$$f_{act} > \frac{\mu_s Wg}{(N+P)}. \tag{3.4}$$

Where, the payload mass 'W' is assumed as 8g (from section 3.2.1), 'N' is the number of active legs which are actuated, 'P' is the number of passive legs that act as points of support, 'μ_s' is the coefficient of static friction between the legs and the crawling surface, and 'f_{act}' is the actuation force. Equation 3.2 implies that when the *N* active legs are actuated, they do not overcome the force due to friction. Thus the *N* legs do not slip. Equation 3.3 implies that when the *N* active legs are actuated, they cause the *P* passive legs to slip. Thereby the robot body moves in the opposite direction to the actuation and the passive legs are dragged with it. Equation 3.4 is the required condition for the legs to be brought back to the initial condition one after the other. The wave gait is the first choice in sequencing power distribution for stick-slip locomotion. Thus, when the first leg is powered-off with the rest *(N-1)* in "ON" state, the leg slips. For example; when P=2, N=4, W=8g, μ_{s1} =0.33 (typical silicon-silicon coefficient of

friction). Equations 3.2 ~ 3.4 produce the following conditions for actuation force: a) f_{act}<4.219mN; b) f_{act}>0.423mN; c) f_{act}>1.90mN.

Thus, the actuator selected needs to produce between 1.9 and 4.22mN in order to overcome the friction and realize microcrawler type locomotion. Bulk micromachined electrothermal actuators are capable of generating this level of output forces and occupy roughly 2mm^2 area on the substrate. Thus, four such actuators as required by the static analysis above will roughly occupy 8mm^2 area. From section 3.2.1, the maximum allowable XY span is 100mm^2 which leaves plenty of room for the motion transmission system, passive legs, and area occupied in interfacing the MEMS substrate with the backpack. This also suffices mN level force required by the articulated manipulator arm robot.

One of the challenges in using electrothermal actuators is the high actuation power required. This is particularly important when we need to operate in untethered mode, while powering the microrobot from an on-board battery. The power drawn by four to six electrothermal actuators can easily run upto several Watts. A unique way to work around this drawback would b e to divide every cycle of the carrier PWM signal into sequence of high frequency (1 kHz) pulses sent to different actuators. However, at any given instance of time there is current flowing to only one actuator, and the load on the power electronics is reduced by 1/N, where 'N' is the number of active legs, at a cost of 1/√N to the amplitude of motion. Another potential drawback of electrothermal actuators can be excessive heating leading due to reduced heat dissipation within vacuum environments, such as inside a SEM chamber. This however, can be resolved by designing for increased heat dissipation via conductivity.

By comparing the actuator review with microrobot requirements and desired specifications presented in section bulk micromachined electrothermal actuators are chosen to drive the microrobots.

3.5 Joints and Motion Transmission

The joints connecting the legs to the actuator of the microcrawler need to satisfy the high payload condition outlined in section 3.2.1. With the articulated arm design, the

requirement changes to producing mN range force output in 3D while resisting upto few N-m^2/rad of torsional rigidity. Thin film micromaching based joints, such as those formed using Poly MUMPS ® have been used to achieve in-plane and out-of-plane joints with varying degrees of freedom. However, these joints are weak and are not the first choice for microrobot design. High aspect ratio bulk micromachined flexures can be monolithically fabricated to form in-plane joints and assembled to form out-of-plane joints with high section modulus and thus required stiffness and load bearing capacity. High aspect ratio flexures can be adapted to satisfy joint requirements as follows:

- As single degree of freedom passive revolute joints, they provide high stiffness along axes perpendicular to the axes of motion. This can be used to generate the high torsional rigidity required by some of the joints supporting the manipulator type microrobot.

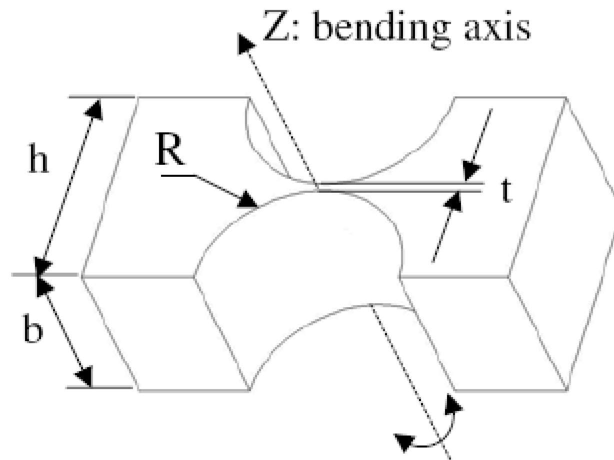

Figure 3.3 One degree of freedom flexure [42]

An example of such joints used as a part of a XY stage design [42] is shown in figure 3.3. Referring to this figure, bulk micromachining such as DRIE can be adopted to achieve appropriate values of dimension ‘b’.

- As part of microsnapfasteners they can be used for assembly of out-of-plane joints, such as microcrawler legs.

- As two and three degree of freedom revolute joints, they provide a means to incorporate dexterity required by the manipulator type microrobot.

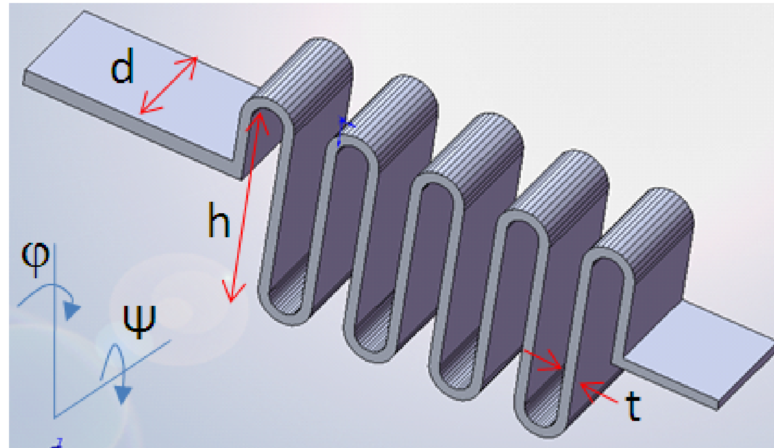

Figure 3.4 Two axes flexure joint.

Figure 3.4 shows a typical two axes flexure design. The two degrees of freedom associated with this design are pitch along the 'Ψ' axis and 'φ' along the yaw axis.

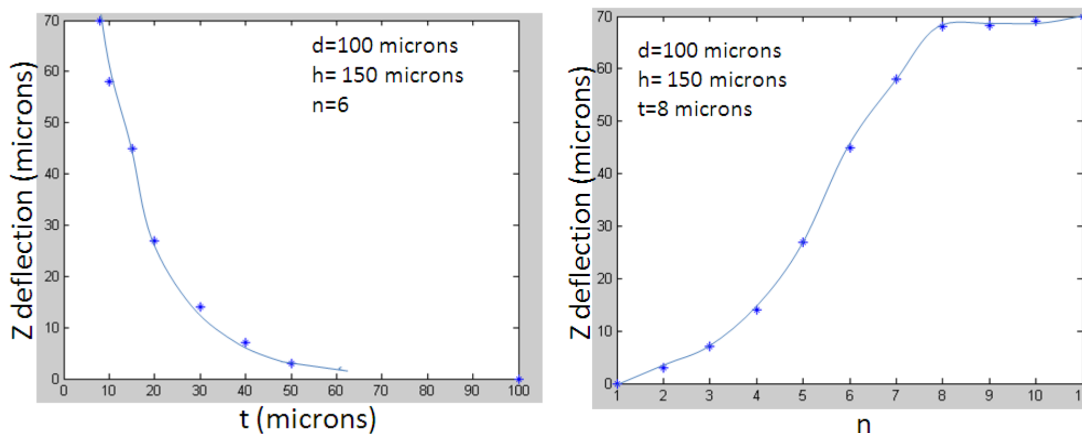

Figure 3.5 Two axes flexure design

The design parameters are the depth 'd', which is also the depth associated with typical micromachining techniques (device layer on a Silicon on Insulator wafer), the number of turns 'n', thickness 't', and the height 'h'. Figure 3.5 shows the maximum elastic deflection variation along the Z axis for various design parameters.

- Flexural joints are an excellent means to transmit the high precision associated with MEMS actuators for high precision applications. This is mainly because of the absence of friction and backlash.
- Two and three DOF flexures can be used to efficiently transmit planar motion into non-planar directions. This is critical in achieving the 3D work envelope required by the manipulator type microrobot.

Based on the above mentioned details and the analysis described in section 3.4 to 3.5, electrothermal actuators coupled to microsnapfasteners and high aspect ratio flexures are chosen as the basic building blocks used to create microrobots.

3.6 Fabrication

There are several ways to accomplish bulk micromachining of these high aspect ratio actuator and joints. The choice of micromachining process is dictated by the material and specification of device dimensions and tolerances. DRIE MEMS, SCREAM, LIGA, etc are some examples. Some of these processes are carried forward from VLSI related CMOS fabrication techniques. DRIE MEMS is one such example.

Deep Reactive Ion Etching [92] based fabrication typically results in 18~20:1 aspect ratios and are mainly compatible with poly Si. The process involves using a two gas mixture. One of the gases (SF_6) reacts with Si and is used as the dry etchant, while the second gas (O_2 or C_4F_8) is used to passivate the side walls resulting in high aspect ratio structures. This process can be accomplished using a single mask for patterning and is a popular technique used by researchers in this field.

The SCREAM process [93] is similar to the DRIE with the addition of a metallization step. The metallization is used to further passivate the side walls, thus achieving higher aspect ratios. The LIGA stands for lithography, electroplating and molding (from a German acronym). In this process, an X ray sensitive polymer photoresist , typically PMMA, bonded to an electrically conductive substrate, is exposed to parallel beams of high energy X rays from a

synchrotron radiation source through a mask. Chemical removal of exposed resist results in 3 dimensional microstructures, which can be filled by electro-deposition of metal. The metallic mold is used to produce parts in polymers or ceramics using injection molding. Other bulk micromachining techniques include non-conventional machining such as the use of laser, wire-EDM, and ultrasound.

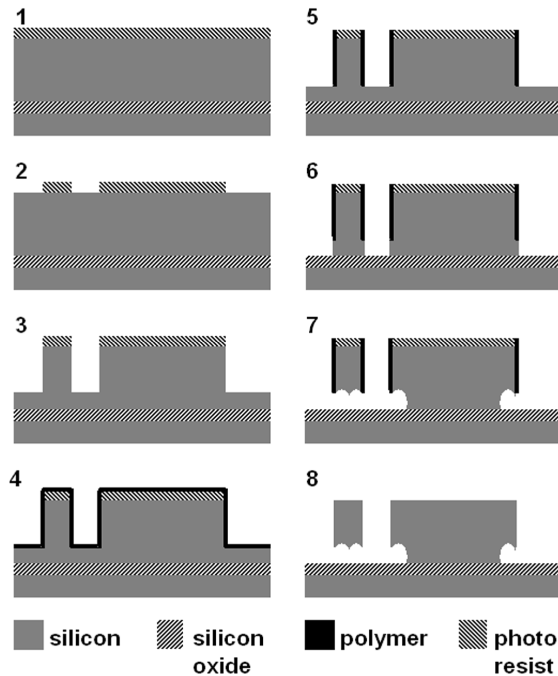

Figure 3.6 SCREAM Bulk Micromachining [93].

The single mask DRIE process is a batch fabrication technique and can lead to high throughput fabrication of microrobot components. The desired substrate XY footprint from section 3.2.1 is 10mm x 10mm. A 4” Si wafer can be used to batch fabricate 52 substrates with this footprint. With this reason, DRIE based single mask process technique is selected as the fabrication technique.

CHAPTER 4

MICROROBOT MANUFACTURING

The framework presented in chapter 3 describes a methodology to zero down on the configuration and micromanufacturing technology to be developed or utilized. Based on this outline derived, the detailed design, fabrication, assembly, and packaging details are described in this chapter. The micromanufacturing philosophy adopted in prototyping the microrobots presented in this dissertation is summarized as follows:

- Design flexure based assemblable microsnapfasteners joints compatible with passive gripping based assembly techniques. Flexure design is accomplished taking into consideration the high yield assembly condition. This is described in section 4.1.
- Develop and implement bulk micromachining fabrication processes. The resulting high aspect ratio components are $2^1/_2$D in geometry. The fabrication process is described in section 4.3.
- Employ already existing automated microassembly techniques to assemble multiple microrobot prototypes. The microassembly procedure is described in greater detail in section 4.4.
- Develop and implement packaging techniques to integrate micromechanical modules with electronic module.

This micromanufacturing procedure allows the use of simple fabrication process while focusing on design for assembly and packaging as described in the following sections.

4.1 Design of Microsnapfasteners for High Yield Assembly

4.1.1 HYAC Lemma

Design presented in this dissertation is implemented so as to concurrently satisfy device functionality requirements and the constraints imposed by the manufacturing process involved. This pertains to both component and system level design. Assembly ‘yield’ is a metric

adopted to quantify successful manufacturing of the microrobot prototypes. A high yield assembly condition (H.Y.A.C) encompassing the various stages of the micromanufacturing procedure adopted is given by

$$\sigma_{1\alpha}^2 \geq \sigma_{2\alpha}^2 + \sigma_{3\alpha}^2. \qquad (4.1)$$

Where, $\sigma_{1\alpha}$ is the standard deviation of combined error tolerance designed into the part and the error in fabricating that component along 'α' dimension, $\sigma_{2\alpha}$ is the error in post fabrication detachment of the component from the substrate or de-anchoring the component and $\sigma_{3\alpha}$ is the error in manipulation, assembly and packaging. Assuming that all processes of positioning microparts in the workspace is normally distributed, a 99% assembly yield can be guaranteed upon satisfying the condition outlined in equation (4.1).

The H.Y.A.C. condition basically states that the combined uncertainty of locating microparts and the end-effector in the workspace should be smaller than the snap-fastener misalignment design threshold that guarantees a successful assembly operation.

4.1.2 Micro part design for compliance based assembly

Microassembled joints incorporated into the microrobots use multiple serial/parallel instances of 2½D component assembly with micro snapfasteners. For instance, figure 4.1 depicts the insertion of a 2½D rigid part A into a compliant part B along the X direction. This single step assembly process can be modeled using a force equation given by:

$$F_{ABi}(r) = f_{ri}(\Delta x, \Delta y, \Delta\theta, \mu, \bar{a}). \qquad (4.2)$$

where i=x,y are the two components of the insertion force, Δx, Δy are misalignments between the parts in the insertion direction and perpendicular to it, $\Delta\theta$ is angular misalignment around the Z direction, μ is the coefficient of friction, $\bar{a}$ is a parametric vector describing the part geometry, and $r = r_0 ... r_f$ is a insertion regime parameter describing the contact (one-point, two point, chamfer crossing, and insertion snap).

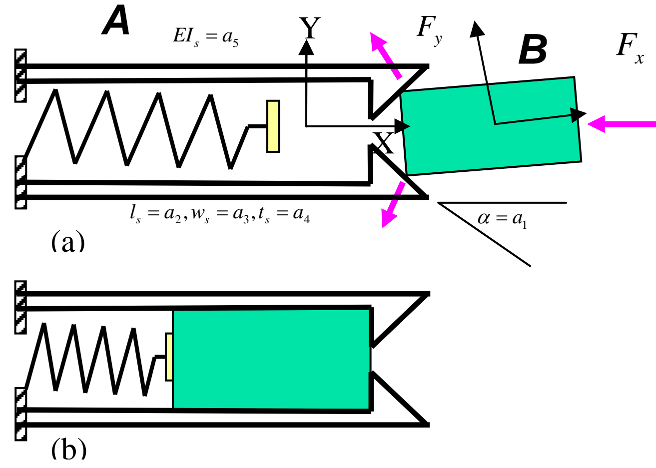

Figure 4.1 Microsnapfastener FBD. (a) Free body diagram depicting the insertion of rigid part B into compliant snap-fastener A, shown in a two-point crossing state; (b) assembled condition.

To design an appropriate snap-fastener, the geometry design vector $\bar{a}$ is chosen such that for all misalignments in y and θ below a given design threshold $\Delta y \le \sigma_{1y}, \Delta\theta \le \sigma_{1\theta}$, we have:

$$\text{Min}\,(F_{ABx}(r_j), j < f\,),\ \text{Max}\,(F_{ABx}(r_f)) \text{ and}$$

$$F_{ABy}(r_j) \le F_{yield}, j \le f\,, \tag{4.3}$$

where F_{yeild} is the yield strength of the microstructure. In other words, the snap-fastener design criterion is based on minimizing the insertion force, and maximizing the retention force without breaking the structure.

The misalignment design thresholds σ_1 are chosen in conjunction with the part manufacturing tolerance, part B positioning tolerance prior to assembly with respect to the substrate, and the manipulator positional accuracy holding part B with respect to the substrate. Specifically, a misalignment tolerance below $3\sigma_{1y}$ and $3\sigma_{1\theta}$ should guarantee a 99% assembly yield.

4.2 Design Example

As an example of fastener design, consider the connector in figure 4.2, which is

assembled using a lateral insertion operation of a vertical MEMS part into a socket. The dominant forces that act upon the microparts during assembly are (1) Insertion force (force along X axis) required to assemble the part and (2) retention force (force along Z axis) with which the MEMS part is retained by the joint after assembly. These forces depend on 1) socket cantilever stiffness 2) parts interference due to design geometry 3) coefficient of friction and 4) positional accuracy during insertion.

The snap arm in Figure 4.3 can be represented as a cantilever beam with length ‘l’, width ‘b’ and height ‘h’, while δx and δy are the cantilever end deflections during assembly and θ is the guide angle.

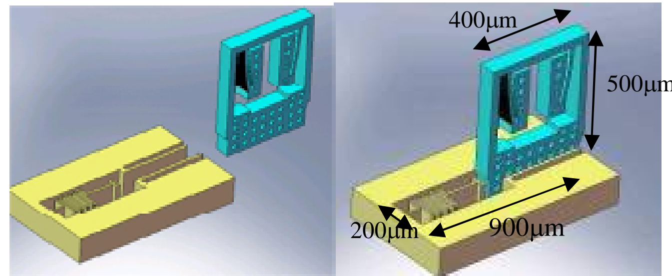

Figure 4.2 Design of microsnap fastener and micro part.

The horizontal component of the force due to deflection of socket arms (cantilever bending) is denoted by F_{in}^{a} and the force due to spring stiffness is F_{in}^{b}. The cantilever deflection force can be written as:

$$F^{a}_{in} = F_{ABx}(r_1) = \frac{6EI\delta y}{(L-\delta x)^3(\mu\cos^2\theta - 0.5\sin 2\theta)} \quad . \tag{4.4}$$

where ‘E’ is the Young’s modulus of silicon E= 160GPa, ‘I’ is the moment of inertia about the neutral axis, ‘b’ = 100 μm is the thickness of the microsnapfastener, ‘h’ is the arm height, ‘L’ the arm length, ‘δy’ = deflection due to bending, θ is the “snap angle” and ‘μ’ is the coefficient of static friction. F_{in}^{b} is determined using FEA simulation and verified experimentally using a SensorOne ® AE-800 series micro force sensor. As shown in figure 4.4, the maximum force obtained is 24mN.

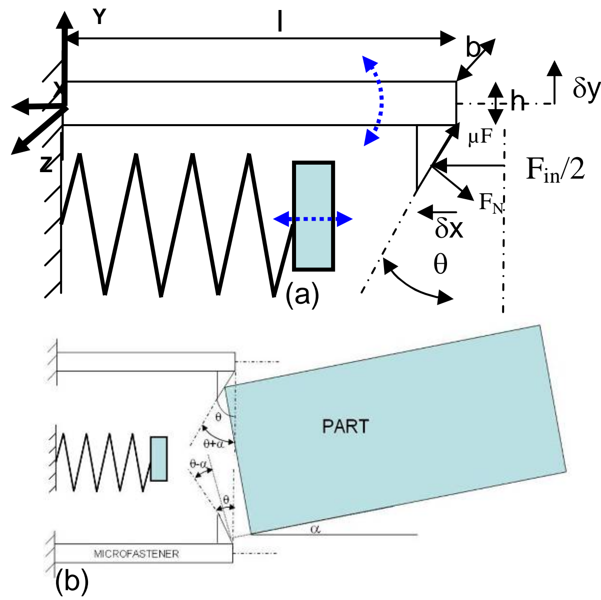

Figure 4.3 Microsnapfastener design. (a) Micro fastener modeled as a spring+ cantilever (b) - fastener misalignment with part.

'L', 'h' and 'θ' make up the design vector $\bar{a}$ from equation 3.2. By varying these parameters, the resulting insertion and retention forces are compared. The design goal is to reach the highest retention force level while minimizing the insertion force. Thus, the design parameters are varied and an optimal design is chosen. The parameter values associated with this design 'L'=600µm, 'h'=10 µm and 'θ'=75º results with the following insertion force variation: F_{in}^{a} =14.5mN and F_{in}^{b} =25mN. The retention force is given by:

$$F_{ret} = \mu F_{in}^{b} + F_{in}^{a}. \tag{4.5}$$

The F_{in}^{b} term includes the friction factor as shown in equation 4.5. During insertion, a misalignment in the angle between the part and the arm's neutral axis is also a possible cause for variation in forces. This misalignment arises due to the tolerance between the MEMS part width and the socket width between the two cantilever arms. For the current design, this tolerance was 10 µm. The part has a length of 100 µm. Hence the maximum angular misalignment permitted is α=5.712 degrees. This misalignment angle adds to the 'θ' parameter on one of the arms and subtracts from the same on the opposite arm.

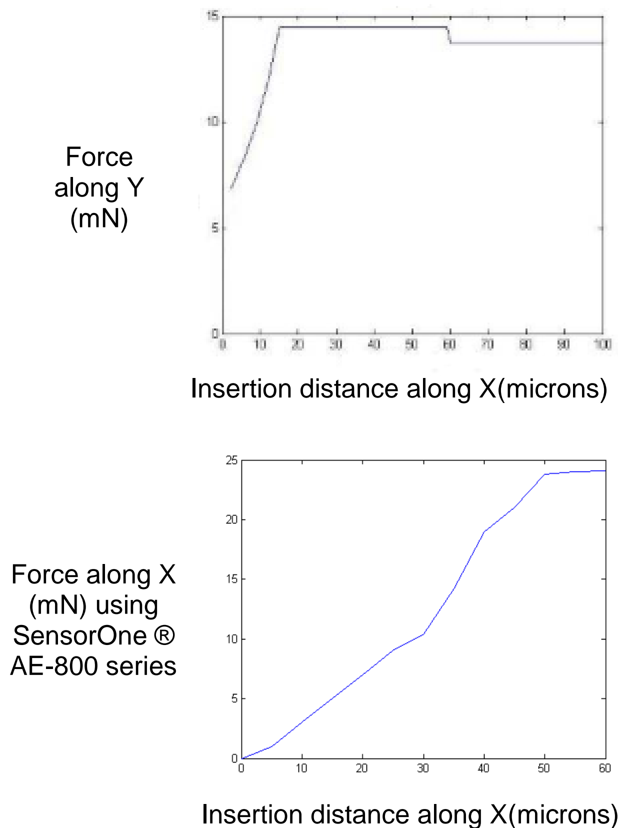

Figure 4.4 Force variation during microassembly, Insertion force (Y axis) variation for varying cantilever parameters versus insertion distance (X axis). (a) Low insertion & high retention forces (b) Experimental force insertion measurement

Tolerance along the direction of insertion (σ_{1x}) is provided by the spring pushing the part against the snap arms thus compensating any misalignment along that direction.

4.3 Fabrication

Most microfabrication techniques used in the fabrication of MEMS involve processing the top surface of a wafer made of or supporting the appropriate material on it. The resulting top-down fabrication process results in parallel or batch fabrication of multiple components or parts with feature control only on the top surface, i.e. the XY plane. The processing on the perpendicular Z direction is limited to straight through cuts. These components are thus called $2^1/_2$ in dimension or $2^1/_2$D. Many of these processes are carried forward from the CMOS IC

industry and involve using dry or wet chemical etching process to add or remove materials. There also exist non conventional processing techniques such as using laser or ultrasound. Majority of the microrobot components referred to in this dissertation were fabricated using bulk micromachining of Silicon using the Deep Reactive Ion Etching process [93]. The choice of material was based on the preference to use relatively simple batch fabrication techniques. The process flow is shown in figure 4.5.

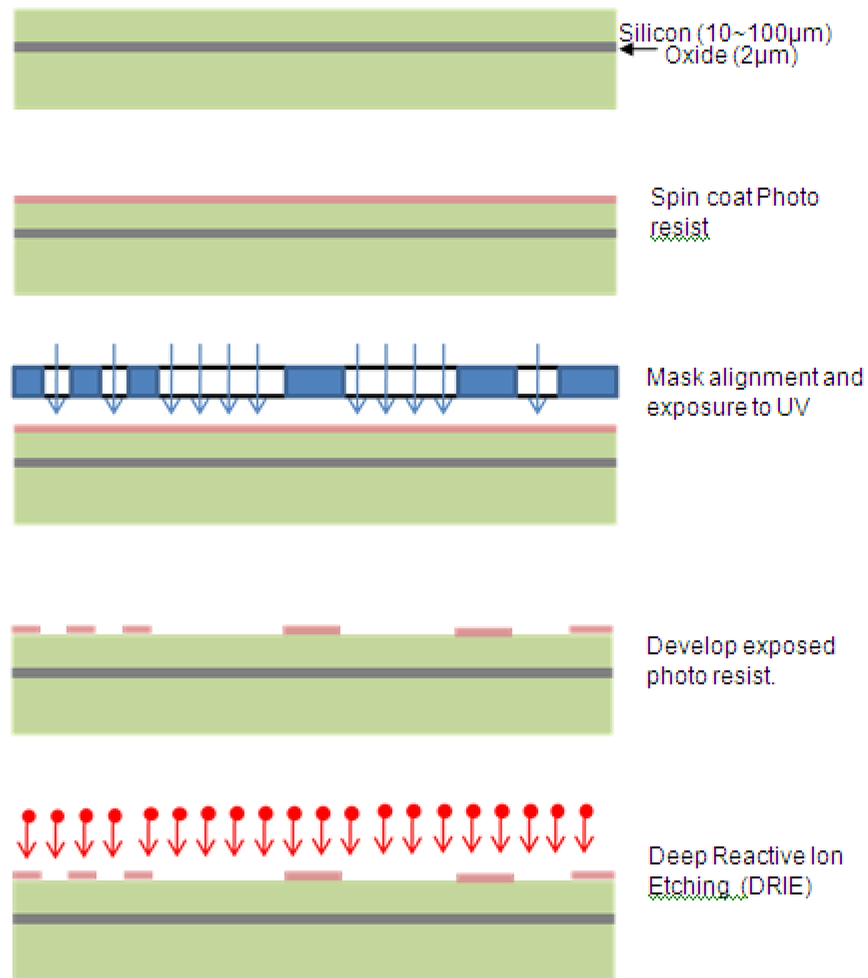

Figure 4.5 SOI Device Layer Microfabrication Process.

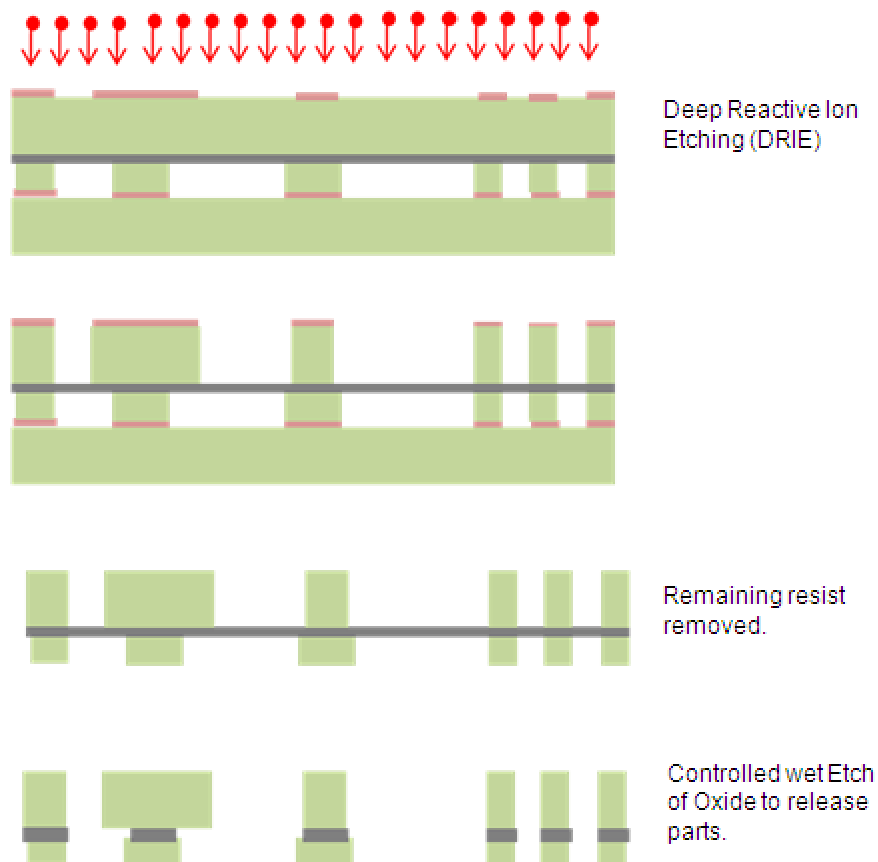

Figure 4.6 SOI Handle Side Microfabrication Process.

The parts are fabricated out of a SOI (Silicon On Insulator) wafer. A SOI wafer consists of one layer of Silicon Dioxide sandwiched between two layers of Silicon. As shown in the figure 4.5, the process is started with device side of the wafer, which is usually between 2~100 microns thick. The surface of the device side is coated with 3~4 microns of positive photo resist and using a mask aligner, the design layout is transferred onto the resist. Figure 4.6 shows an example of layout. The next process involves dry etching of the exposed Silicon surface which results in a high aspect ration etching of this layer all the way until the oxide layer is reached.

The process is repeated on the other side of the wafer, called the handle layer. The thickness of this layer ranges between 250 ~ 400 microns in thickness. Prior to this process, the device side that was etched earlier is bonded to a support wafer made of Silicon. This is

required to add mechanical strength to the wafer which is weakened considerable by the etching process.

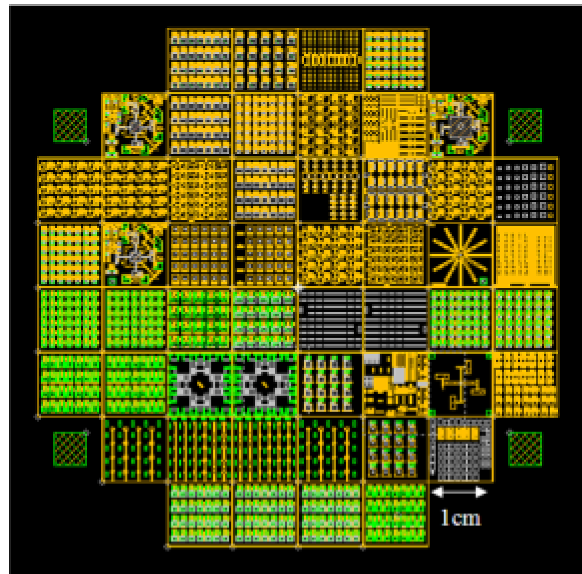

Figure 4.7 Design layout for a 4" wafer.

The handle layer is etched all the way through until the oxide layer is reached. Following this, the remnant photo resist is removed using plasma etching. The underlying oxide layer is partially etched using Hydrofluoric acid. This results in the controlled release of micro components, which are ready for the downstream processes such as assembly and packaging. In order to facilitate this process, rectangular openings (etch holes) shown in figure 4.7 are incorporated into the design

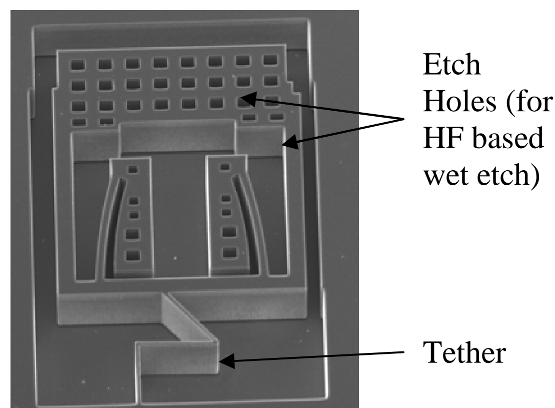

Figure 4.8 $2^1/_2$D part.

At the end of the fabrication process, these parts are released from the substrate with a tether constraining them to the wafer surface to maintain part location. A micropart fabricated using this process outlined and tethered to the substrate is shown in figure 4.7. Prior to microassembly, the tether is broken using the same robotic end effector that is used to pick the part. Tether breaking causes misalignment in the position of the part on the substrate. Unreleased device layer walls fabricated around the part act as hard-stop locators to limit this misalignment along directions X,Y, and θ.

The outlined fabrication process results in planar $2^1/_2$D parts. The $^1/_2$ D refers to the extrusion of the planar design along the normal axis. This means that microscale features can only be defined in the plane of the die and machined to a fixed depth. Microactuators, revolute joints etc, can thus only move in the plane of the die. The resulting MEMS devices consist of minimal mechanical functionality along out-of-plane direction. Microassembly refers to the post fabrication re-orientation of components. The use of assembly in micromanufacturing thus allows the formulation of complex 3D devices and the integration of parts from differing fabrication techniques into a single system (heterogeneous MEMS).

When the scope of this discussion is the limited to bulk micro machined joints, two categories arise: flexure joints and assembled joints.

,

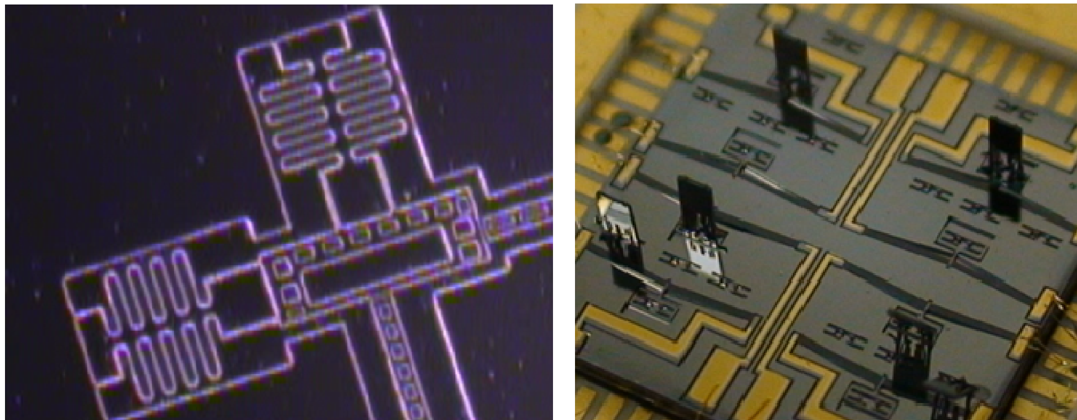

Figure 4.9 Microrobot Joints. Left- Flexure joints, Right-Assembled joints.

Figure 4.8 shows examples of the two joint types. Monolithic flexural springs shown in figure 24 (left) are mainly used as revolute joints supporting a shuttle mass. Link formation between such joints is used in the design of micro robots to achieve dexterity and work volume requirements. Figure 4.8 (right) shows six assembled joints. The parts assembled stand out of plane at almost 90 degrees with respect to the substrate surface.

Figure 4.10 Assembled 3D Microflyer Mechanism (ARRIcopter project at ARRI).

Assembled revolute joints carry many advantages over flexural counter-parts. An advantage is that they are not limited in their motion. For example, the ARRIcopter microflyer shown in figure 4.9 consists of several revolute joints. The continuous rotary motion required by the rotors cannot be realized using flexure joints.

The challenge in microassembly arises due to the fact that interaction between micro parts is dominated by surface forces as opposed to volumetric forces that dominate the macro scale. Hence assembly strategies should implement control over these dominant surfaces forces such as stiction or adhesion as opposed to gravity. The most common assembly strategy applied to the micro robots presented in this dissertation uses assembly using micro snapfasteners mating with rigid relatively rigid components.

4.4 Microassembly

Microparts are passed between end-effectors and substrate or other assemblies, but because large field of view visual information cannot be obtained at high resolutions, more than one robot is necessary in the assembly cell. To assemble 2 ½ D microparts, the number of

DOFs for all robots must add to at least 6 independent joints. This number should exceed 6 if redundancy/increased dexterity or increased workspace is necessary.

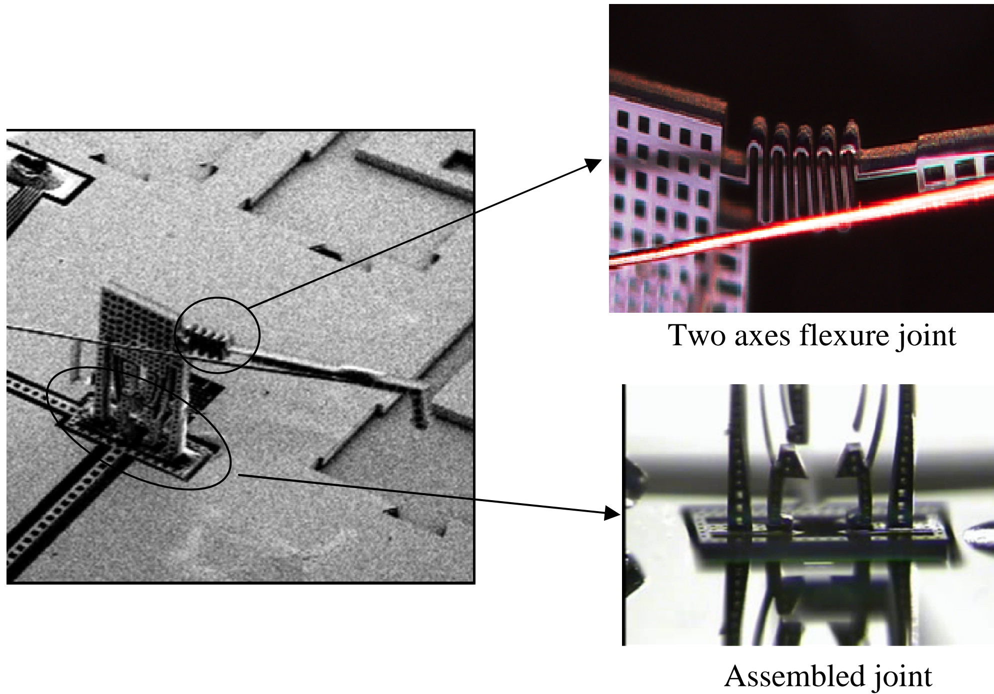

Figure 4.11 Combination of monolithic and flexure joints.

For our assembly cell, μ³, we use a configuration with 4 DOFs on the gripper carrying manipulators, and 5 DOFs on the substrate carrying manipulator as shown in figure 4.11. Furthermore, each robotic chain is composed of at most 3 independent rotational DOFs and 3 independent translational DOFs so that we can decompose the translational and rotational calibration. Because we will be assembling 2½D microparts, a terminating roll DOF in the robotic chain and a programmable remote center of rotation of the end-effector is required for part rotations of 90 degrees.

Force and visual feedback from the end-effector for close-loop control is not necessary during automation, but it is necessary during calibration. An appropriate approach utilizes weak-calibration by means of vision from multiple microscopes and a “hand-to-eye” configuration

(because the microscope FOV is limited). While the configuration of μ³ is not unique, the desired functionality is accomplished with minimal hardware.

The workcell precision is accomplished via well-known statistical methods of kinematic calibration for end-effector frames from all the robots sharing the workspace. More information on this microassembly station can be found in the following publications [94-95].

4.5 Tolerance Analysis and Experimental Verification

This section presents experimental verification of the high yield assembly condition (H.Y.A.C) described in equation 3.1. A tolerance analysis determining the average misalignment due to the fabrication reveals $\sigma_{1xyz\theta P}$ and that during detethering is used to determine $\sigma_{2xyz\theta P}$. The subscript "P" refers to the variance defined when the part is on the substrate and prior to any manipulation. A typical image used for location analysis is shown in Figure 4.12. This particular micro part has moved after release to a location that contacts a hard stop.

Square etch holes distributed on the part (on top end and in the gripping region) are mapped with a reference corner to determine the XYθ location of the part. Figure 4.13 illustrates an image of a detethered part obtained using a Veeco® NT1100 surface profiler.

Using this technique, we measured misalignments during ten detethering operations and found:

$$\sigma_{2xP} = 1.12\mu m, \sigma_{2yP} = 1.8\mu m \text{ and } \sigma_{2\theta P} = 0.1^\circ. \quad (4.6)$$

Figure 4.14 shows the coordinate transformation between the part pick pose from the substrate and the part insertion pose into the snap-fastener. As a result of this transformation, σ_{2yP} changes into σ_{2za} and σ_{2xP} changes into σ_{2xa}. For simplicity let us denote σ_{2xyza} as σ_{2xyz} .

With knowledge of the calibration map, we now can simply servo the joint axes of robots M_1 and M_3 to position the end-effector of M_1 to detether the MEMS die at die coordinates P. The automated detethering process is followed by part pickup, robot pose reorientation, and part insertion into the snap-fastener. Figure 4.14 shows the compliant gripping location on the part.

We now use the H.Y.A.C lemma outlined in section 4.1 to prove the high yield eligibility of the detethering, part pickup and assembly sequence.

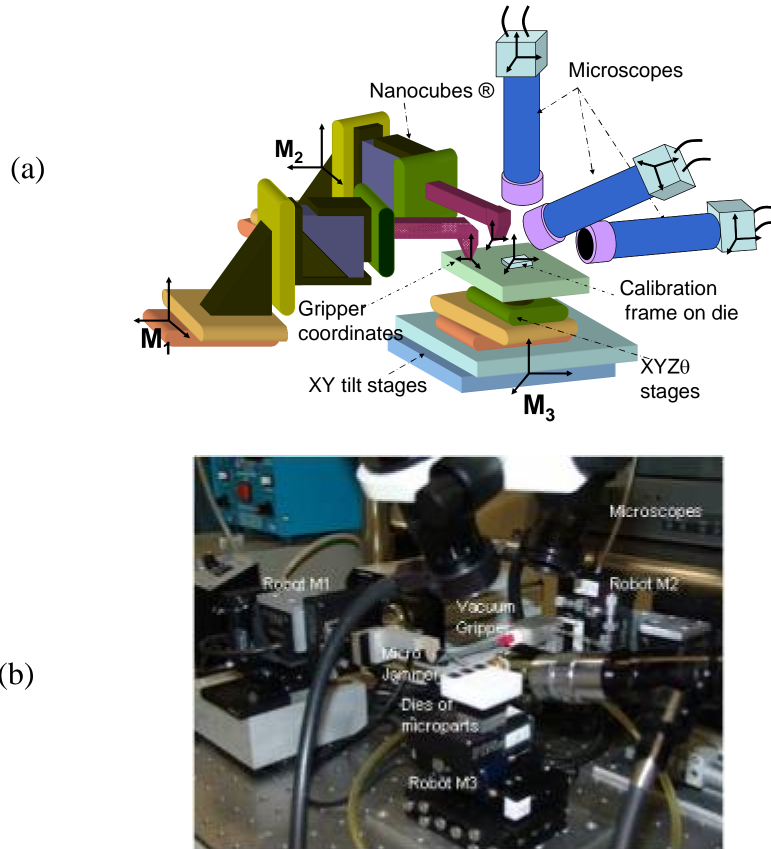

Figure 4.12 Microassembly Platform (a) Schematic diagram of μ^3 (meso-micro-nano) platforms with micro grippers; (b) Kinematic representation of the multirobot system.

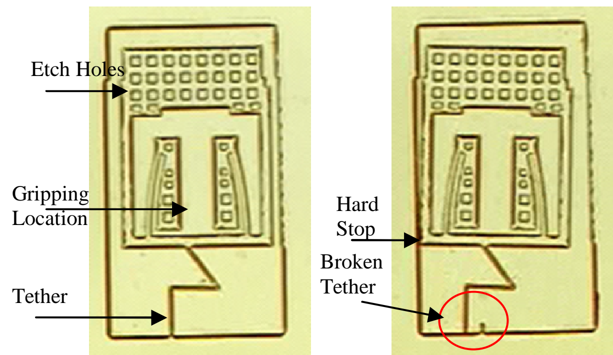

Figure 4.13 Part on substrate. (a) before detethering ;(b)after detethering.

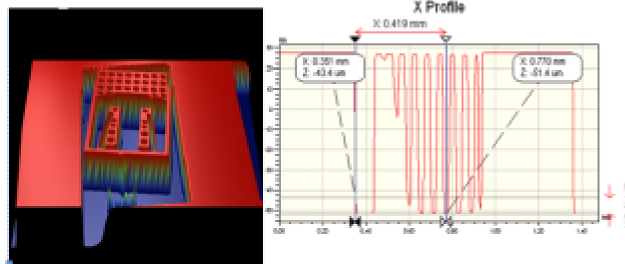

Figure 4.14 Surface profile data of the released and detethered micro part.

Referring to figures 4.14 and 4.15, the compliance based pickup of the part compensates the misalignment along the X_P axis and rotation θ about the Z_P axis. For part pickup, the H.Y.A.C. condition requires that:

$$\sigma_{1xyzP}^2 \ge \sigma_{2xyzP}^2 + \sigma_{3xyzP}^2 \quad . \tag{4.7}$$

The numerical values of uncertainties along X_P are:

$\sigma_{1xP} = 3.3\mu m$ $\sigma_{2xP} = 1.12\mu m$ and $\sigma_{3xP} = 2.64\mu m$.

$$\sigma_{1xP}^2 = 11.08 \ge \left(\sigma_{2xP}^2 + \sigma_{3xP}^2 = 8.224\right) \tag{4.8}$$

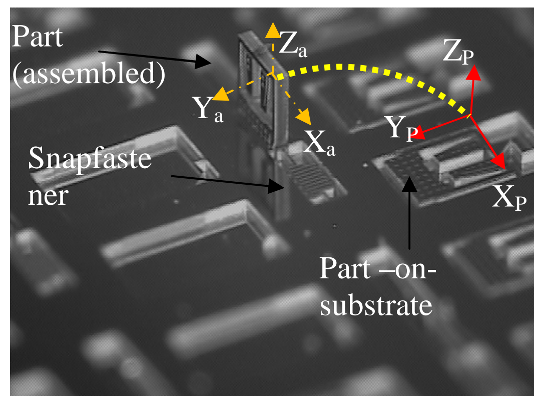

Figure 4.15 Coordinate system transformation between part-on-substrate and assembly condition.

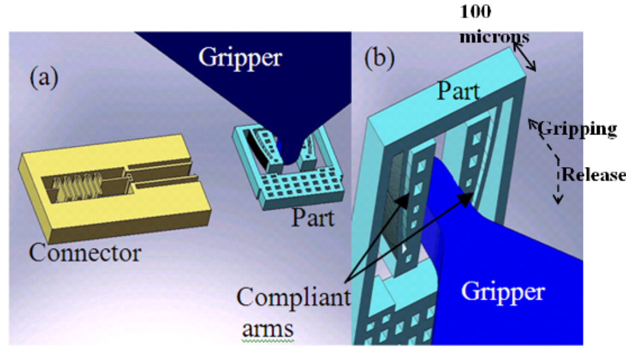

Figure 4.16 Microassembly. (a) Assembly scene (b) Compliant gripping on part.

σ_{1xP} value is derived from the fillet radius in the gripper that centers the detethered part during pickup.Similarly,

$\sigma_{1yP} = 5\mu m$, $\sigma_{2yP} = 1.8\mu m$ and $\sigma_{3yP} = 2.64\mu m$.

Hence,

$$\sigma_{1yP}^2 = 25 \geq \left(\sigma_{2yP}^2 + \sigma_{3yP}^2 = 10.17\right) \tag{4.9}$$

The uncertainty $\sqrt{\left(\sigma_{2yP}{}^2 + \sigma_{3yP}{}^2\right)} = 3.19\,\mu m$ is transformed into σ_{2z}. Referring to the gripping direction shown in figure 4.14 and figure 4.14, gripper insertion into part during pickup is along Z_P and the parts are 100µm thick. For successful pickup, $\sigma_{1zP} = 3.33\mu m$. Furthermore, $\sigma_{2zP} = 0$, since the part is always supported along Z_P by the substrate and $\sigma_{3zP} = 1\mu m$. Thus,

$$\sigma_{1zP}^2 = 11.08 \geq \left(\sigma_{2zP}^2 + \sigma_{3zP}^2 = 1\right). \tag{4.10}$$

and $\sqrt{\sigma_{2zP}^2 + \sigma_{3zP}^2} = 1$ is transformed into σ_{2y} during part insertion into the connector.

Next we look at the part-connector assembly scenario and check for agreement with H.Y.A.C. The connector design tolerance σ_1, the part misalignment tolerance σ_2, and the manipulator positional accuracy σ_3 are:

$$\sigma_{1x,y} \le 3.3\mu m, \sigma_{2x,y} \le 1\mu m, \sigma_{3x,y} \le 2.64\mu m.$$
$$\sigma_{1\theta} \le 2.38^{o}, \sigma_{2\theta} \le 0.75^{\circ}, \sigma_{3\theta} \le 0.75^{o}. \qquad (4.11)$$

and, $\sigma_{2_z} \le 3.19\mu m, \sigma_{3_z} \le 1\mu m$.

This means that if an end-effector is positioned with repeatability σ_{3y} and $\sigma_{3\theta}$ relative to the substrate, the assembly yield will be over 99% since the H.Y.A.C. from equation 5 is satisfied:

$$\sigma_{1xy}^2 = 10.89 \ge \sigma_{2xy}^2 + \sigma_{3xy}^2 = 8.79 \ . \qquad (4.12)$$

$$\sigma_{1\theta}^2 = 5.65 \ge \sigma_{2\theta}^2 + \sigma_{3\theta}^2 = 1.125. \qquad (4.13)$$

Figure 4.16 shows an array of eight micro assemblies fastened to the substrate using consecutive insertions.

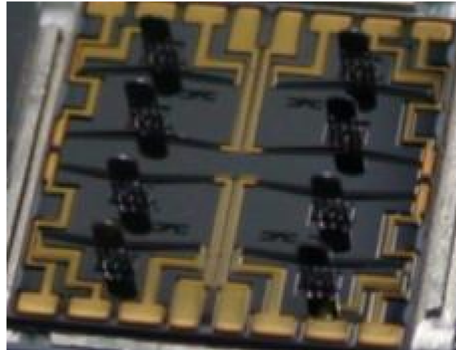

Figure 4.17 Array of parts assembled using the μ^3 system.

4.6 Packaging

4.6.1 Packaging Requirements

Microrobots presented in this dissertation impose various requirements on the packaging process. These robots will be operated under controlled environments, such as inside a clean room, under an Atomic Force Microscope or under high vacuum conditions such as inside a Scanning Electron Microscope (SEM). Thus, they do not need to be hermetically sealed to avoid contamination. However, they impose other requirements which are detailed for both robot types.

The microcrawler robot is designed to execute untethered operation. The power supply module consists of a battery and electronic circuitry. This module is carried in the form of a back-pack that allows untethered operation of the microrobot. Thus, packaging includes the integration of the micro mechanical module with the electronics module and the battery. This is depicted in figure 4.17. As shown, the backpack and the substrate are structurally attach using solder and wires are drawn to establish electrical interconnections.

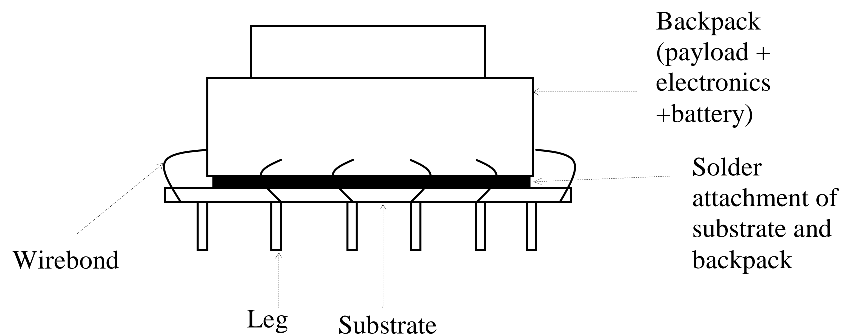

Figure 4.18 Microcrawler line diagram with backpack.

The resulting packaging requirements imposed are:

- Design of the backpack modules so as to minimize its weight and restrict its volume relative to that of the micro mechanical assembly (substrate and legs).
- Design of electrical interconnects between various electronics modules and between the power module and the MEMS substrate.
- Bonding the MEMS substrate to the backpack electronics.

More details on backpack design are outlined in chapter 5 with an example of the ARRIpede microcrawler. The manipulator type microrobot is designed for articulated and dexterous nano manipulation operations. Unlike the crawler, this microrobot does not require untethered operation. However, it requires establishing electrical interconnects at the end of the serial/parallel chain. The packaging requirements imposed by this microrobot type can be summarized as

- Design of electrical interconnects between the power supply module and the MEMS substrate.
- Bonding the MEMS substrate onto a power regulator circuit.
- Establish electrical interconnects for powering probes, specialized tips, and other end-effectors located at the Tool Center Point (TCP) of the micro robot.

4.6.2 Manual Packaging Setup

In order to accomplish microrobot packaging and satisfy requirements outlined in section 4.7.1, a 10 degree of freedom packaging station has been configured. This top-down packaging setup shown in figure 4.18 consists of three Cartesian robots with a total of 9 prismatic degrees of freedom and one rotation. Two of these robots (R_1, R2) are used to hold end effectors for manipulation and the third robot (R_3) is used to position the fixture on which packaging is executed. This manual packaging system also consists of two high magnification cameras.

4.6.2.1 Die Attach

R_1 is used to manipulate a vacuum nozzle used to grip the MEMS substrate. The backpack (crawler) or the power regulator circuit (manipulator) is fixtured on R_3. R_2 is used to dispense bonding material such as Ultra Violet (UV) light curable high viscosity epoxy. With this setup,

- R_2 dispenses Ultra Violet (UV) light curable high viscosity epoxy at the location where the MEMS die will be attached to the backpack.
- Following this R_1 places the die onto the backpack and the package is flooded with UV light for bonding the two modules.

4.6.2.2 Wire Bonding

Following die attachment, electrical interconnects using 30~120 µm Cu wires are drawn between the PCB and the MEMS die as shown in the figure 4.19.

- R_1 is fitted with an electrostatic microgripper for wire manipulation. A solder bump is attached on the PCB in order to compensate for the height mismatch between the pads electric contact pads on the surface of substrate and PCB.

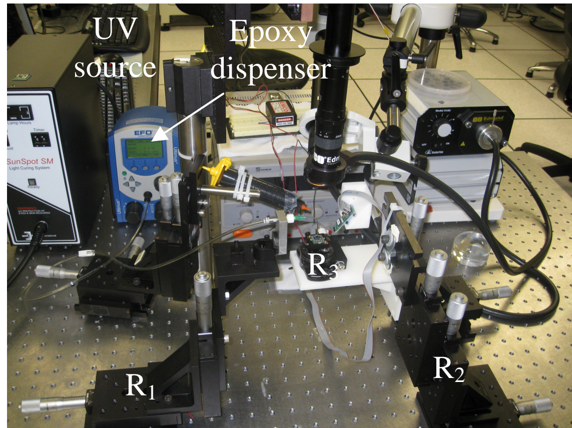

Packaging setup

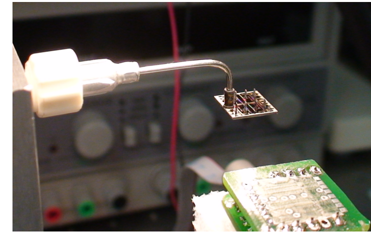

Vacuum handling
of MEMS die

Figure 4.19 Microrobot packaging setup.

- Next, conductive silver epoxy is dispensed on the bump and the pad on substrate using R_2.
- Following this, the stripped Cu wire is gripped by the R_1 robot, aligned to the two spots of silver epoxy and brought in contact with them. At this time, adhesive force between the epoxy and Cu wire takes over and the wire is fine aligned between the two pad locations.
- Following this, UV curable epoxy is dispensed at the location where the Cu wire is attached to the solder bump. Dispensing UV epoxy over the MEMS substrate was found unnecessary.

The above process is repeated 8~16 times in order to wire bond 4~8 actuators. Figure 4.20 shows one pair of completed interconnects.

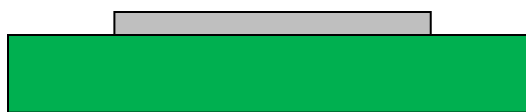

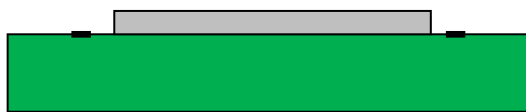

Dispense electrically conductive epoxy
on PCB pads.

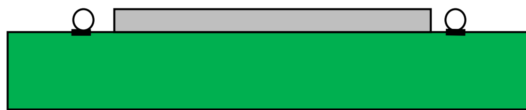

Assemble 500 micron solder bumps
on epoxy using electrostatic

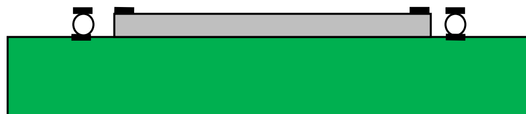

Dispense electrically conductive epoxy
on top of bumps/MEMS pads.

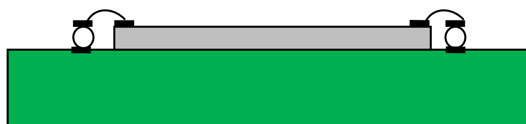

Assemble wire using microgripper.

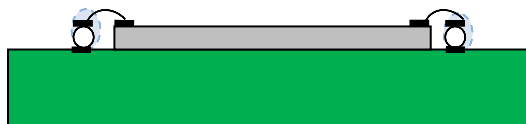

Dispense UV curable epoxy to enhance
joint strength.

Figure 4.20 Wire bonding technique.

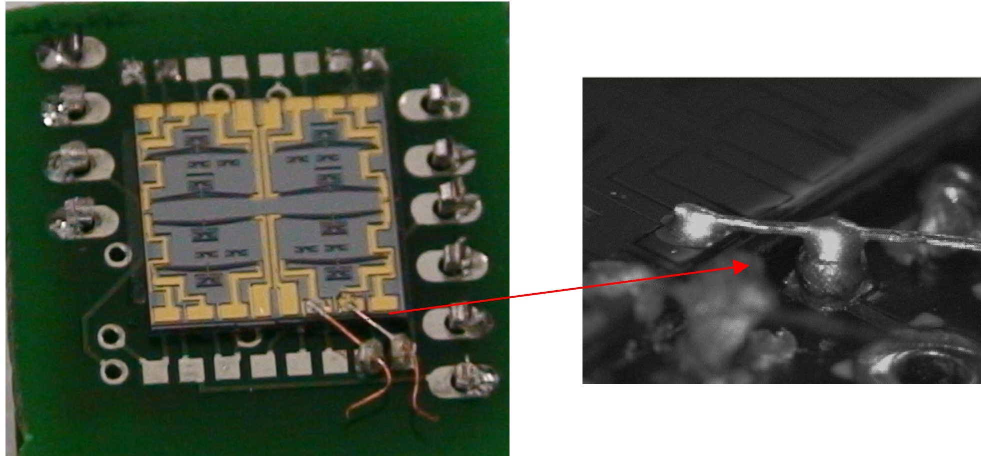

Figure 4.21 Completed wire bond.

4.7 Automated Microsystems Packaging

4.7.1 Overview and System Architechture

The manual packaging technique outlines in section 4.7.2 is useful for prototyping and proof-of-concept. When high volume packaging is required, an automated system capable of die-scale assembly and packaging needs to be configured. To facilitate this, a multi-scale top down assembly and packaging system called the M^3 was configured, shown in figure 37 (*Please refer to APPENDIX B for detailed information on hardware configuration of the M^3 system*). The M³ (Macro-Meso-Micro) is a reconfigurable, multiscale, multirobot system. In order to package microsystems comprising of micro and meso scale parts with different assembly tolerances, the M³ workcell has been designed to meet the following design requirements:

- Use task-oriented control to attain fine positioning, e.g. use direct measurements for closing the loop on precision positioning tasks. This ensures that some manipulators need not be overly accurate in open loop in order to accomplish a given task.
- Allow for the addition and removal of new manipulators in the workcell, and for changing of end-effectors, and other tools as required by specific assembly tasks.

- Require that the range and bandwidth of the fine motion actuator be greater than the resolution and resonant frequency of the coarse motion robot. This requirement is needed in order to achieve vibration suppression at the smallest scale of interest.
- Achieve necessary assembly precision through a combination of fixtures, calibration and servoing in a progression sequence, later referred to as the *RRA precision rules*.
- Use grippers and/or fixtures to constrain parts at all times during the manipulation process. Thus, gravity plays no role during assembly.
- Use a supervisory software architecture that integrates hybrid control systems within a single PC via Labview® and Matlab®. This allows for ease of programming, usage of standard industry tools, ease of reconfiguration, and monitoring of different tasks.

Prior to assigning system resources to accomplish tasks (e.g. manipulators, tools, and sensors), the assembly tolerance budget is established through a combination of simulations and experiments.

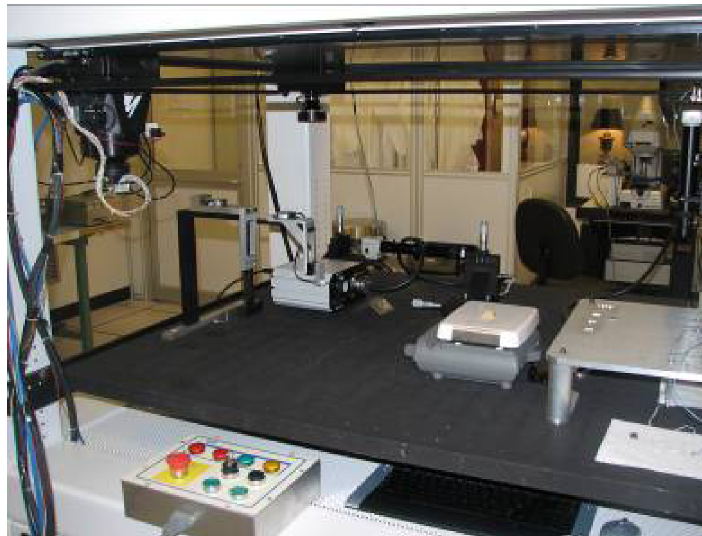

Figure 4.22 M^3 assembly and packaging station.

This budget represents the misalignment between parts that still allows assemblies to complete successfully. Then, the repeatability and accuracy of the entire manipulator chain (e.g. not just the joint actuators) is directly measured. Finally, the position of all parts in the

workspace is carefully mapped and the assembly and packaging process is choreographed through a plan.

The tolerance budget and robot end-effector precision capabilities determine the choice between calibration (open-loop operation), servoing (closed-loop operation), and fixturing (uncalibrated operation) according to the following simple design rules described below:

4.7.2 Qualitative design rules

> ***Rule 1:*** Fixtures can be used to locate objects in the assembly workspace only when the manipulator accuracy is smaller than the required part assembly tolerance.
>
> ***Rule 2:*** Calibration can be used to locate objects in the workspace only if the repeatability of the manipulator is smaller than the part assembly tolerance.
>
> ***Rule 3:*** Servoing (for instance visual servoing) on the relative position between parts and tools can be used only if the resolution of the manipulator is smaller than the part assembly tolerance.

The M³ design approach is illustrated in Figure 4.22, including two iterative loops that generate improvements based on accuracy measurements until the necessary assembly yield is reached. This paper describes in detail the “quasi-static accuracy and yield improvement” loops, containing design and experimental statistical validation of the end-effector precision according to measures defined in the subsequent section. At the end of this loop, statistics on the quasi-static positioning accuracy and assembly yields are obtained. Note that the assembly yield is not the same as the final product yield, as it is achieved at low, un-optimized speeds, and it depends on whether stacked assemblies are reliably bonded. Products will undergo an additional “process yield improvement loop”, that refers to tuning processes such as bonding and sealing that drive the reliability of the product.

This section presents quantitative “RRA-rules” which are used to assign appropriate precision tasks to the M³ robots.

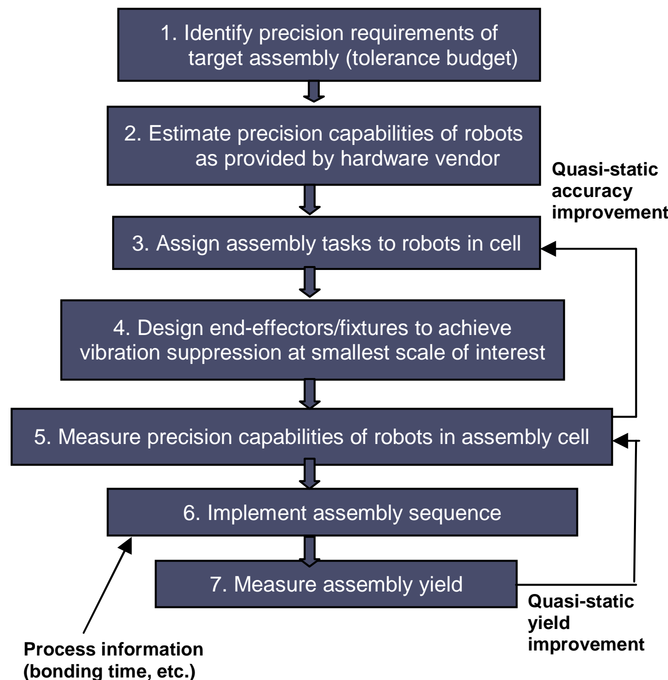

Figure 4.23 Schematic diagram of methodology for designing a multiscale assembly system such as the M³.

These rules are placed in a context of slightly reformulated precision concepts such as fixturing, calibration, servoing, repeatability, resolution and accuracy. We found it useful to revisit these statistical definitions and present them from the point of view of how they are utilized during the operation of a precision robotic cell that changes end-effectors, and frequently recalibrates position of grasped parts. The definitions *combine* the sensor position and measurement uncertainty into the robot accuracy, repeatability and resolution. All definitions assume that Gaussian distribution assumptions are observed for sources of uncertainty in the system. The resulting RRA-rules will be dependent on the variance of these uncertainties.

The M³ system is used to manipulate objects using multiple end-effectors and fixtures with respect to a global coordinate frame of the workcell (frame [0]). A **fixture** F is a rigid mechanical part restraint that can be either fixed in the workspace, or attached to a robot end-

effector. Fixtures have local Cartesian coordinate frames [F], with origin $\{O_F\}$, and relative orientation matrix [^F_0R] or alternate roll-pitch-yaw angles θ_F, φ_F, ψ_F from the base frame. The relative pose of the fixture is known within a certain tolerance, e.g. a Gaussian distribution with covariance σ_{Fk}, where k is the respective degree of freedom, $k\in\{x,y,z,\theta,\varphi,\psi\}$. Without loss of generality, we assume that the fixture position uncertainty is consolidated using the fixture frame covariance (e.g. the part is located with arbitrary accuracy with respect to frame [F]).

Definition 1: **Fixturing** of a part P refers to setting its position relative to fixture F at a mean nominal location with respect to frame *[F]*, with *no* uncertainty. However, the part will have a set of N features (edges, points, surfaces) with the tolerances of feature $i=1\ldots Q$ given by σ_{Pki}.

A **robot** R with M degrees of freedom can be defined by a base coordinate frames $[R_0]$, joint parameters $q=\{q_j, j=1...M\}\in R^M$, and end-effector fixture frame $[R_F]$. The overall end-effector frame uncertainty is normally distributed and joint-dependent, with variance $\sigma_{Rki}(q)$ along DOF k.

A **sensor** S performs measurements of all or some degrees of freedom for part features in the workspace with respect to a sensor frame [S]. The sensor frame localization uncertainties are σ_{Sk}, and its measurement uncertainty of feature i on part P is given by σ_{SPki}. If the sensor does not measure all dimensions of a given feature, the corresponding uncertainty is infinite.

Definition 2: **Calibration** of robot R carrying an end-effector and a part P refers to taking repeated measurements of a set of features on the part using sensor S at a set of different robot poses $\{q_j\in R^M, j=1...N\}$. By collecting the set of N measurements, part feature locations can then be estimated for any robot joint vector using a forward kinematic map $K_N: R^M \rightarrow R^6$. This is typically done by a least squares fit on the data to calculate the kinematic parameters. Of course, 6 DOF parameterizations will have rotation singularities, and the mapping is a homogenous transformation, e.g. a member of $R^3 \times SO(3)$ instead of R^6. However, because microassembly deals with "small-scale" translations and rotations, working with local nonsingular parameterizations in R^6 is a reasonable assumption.

We speak of the **calibration error** as the uncertainty value of the forward kinematic map averaged over the set of all features: $\sigma_{Kk}(q)$. This uncertainty depends on the number of measurements N, the number of features Q, and the sensor uncertainty for all measurements, e.g.

$$\sigma^2_{calibration_k}(q, N, Q) = E[\tilde{K}(q, N, k, \sigma_{SPki}, Q)]\,. \tag{4.14}$$

Both the robot *repeatability* and its *accuracy* can be measured by calibration with respect to a stationary sensor S as follows:

Definition3: We define **accuracy** by powering up the robot at its origin, and moving it to a predefined joint coordinate vector in order to present part feature *i* to one (or more) sensors. We then return the robot at its origin and power it off, and repeat the measurement. Thus, the robot accuracy on axis *k* will be bounded by:

$$\sigma^2_{accuracy_k}(q) \le \min_S \left(\sigma^2_{SPki}(q) + \sigma^2_{Sk} + \lim_{N\to\infty} \left(\frac{1}{N} \sum_{j=1}^{N} (\Delta k_j)^2 \right) \right), \tag{4.15}$$

where Δk_j is the variation in measurement j of the k-th DOF about its mean.

Definition 4: We define **repeatability** as follows: with power on, move the robot between two predefined, but arbitrary points that correspond to two respective joint coordinate vectors, one of which is measured through a sensor. Thus, the robot repeatability on axis *k* will be given by its relative position with respect to the sensor through the bound:

$$\sigma^2_{repeat_k}(q) \le \min_S (\sigma^2_{SPki}(q) + \lim_{N\to\infty} (\frac{1}{N} \sum_{j=1}^{N} (\Delta k_j)^2))\,. \tag{4.16}$$

The difference between the accuracy and repeatability, as defined here, is the fact that the positioning of tools, parts and robots is referenced to hardware fixtures, as opposed to direct sensor measurements, respectively. With these preliminaries, the following result is obvious:

Lemma 1: "Positioning through calibration" is defined as the uncertainty in the

robot/part position as calculated through an estimated forward kinematics map. Because the forward kinematics map was measured by repeated motion and measurement of a part feature, the calibration error has an upper and a lower bound:

$$\sigma^2_{accuracy_k}(q) \geq \sigma^2_{calibration_k}(q, N, Q) \geq \sigma^2_{SPki} \tag{4.17}$$

By increasing the number of calibration experiments and features observed, we can reduce the calibration error to levels close to the feature measurement accuracy, e.g.

$$\lim_{N,Q \to \infty} \sigma^2_{calibration_k}(q, N, Q) = \sigma^2_{SPik} \ . \tag{4.18}$$

Lemma 1 is due to our assumption that measurement uncertainties have Gaussian distributions and the Central Limit Theorem.

Definition 5: **Servoing** with the parts refers to adjusting the position of a feature on the part based on feedback from the sensor used to measure that feature. In a precision assembly cell, servoing (regulation) of the feature vector to zero can be accomplished using an approximate sensor based Jacobian function J_R: $R^M \to R^{6xM}$ by setting joint increments for robot R as:

$$\Delta q = -\lambda J_R^{-1}(q_o) k_{SPi}, \tag{4.19}$$

where k_{SPi} is the 6D pose of feature *i* on part *P* as measured by sensor *S*, $\lambda > 0$ is a positive small constant, and q_0 is a constant joint vector "close" enough to the actual joint vector. Note that this servoing algorithm works, "locally" around q_0, as is the case with small joint variations during microassembly. The Jacobian can be estimated numerically, or by differentiation of the forward kinematics map K obtained after calibration.

Definition 6: We define the **resolution** of the manipulator as the minimum increment $\sigma_{resolution} = min\{\Delta k\}$ that the manipulator can execute. Thus, the following result can be shown:

Lemma 2: The precision attainable through servoing is bounded either by the

manipulator resolution, or by the sensor uncertainty, e.g.

$$\sigma_{servo_k}(q) \leq \max(\sigma_{resolution_k}, \sigma_{SPki}) \tag{4.20}$$

Lemma 2 is a result of that fact that if small increments of the joint angles are given by equation (6), and because $\Delta k = J_R(\theta)\Delta q$, it follows that

$$\Delta k = -\lambda J_R(q) J_R^{-1}(q_o) k_{SPi} \approx -\lambda k \,, \tag{4.21}$$

leading to *k* converging to zero. However, a true zero will not be obtained, either because the manipulator cannot execute a small enough step, *Δk*, or because *k*=0 below the minimum resolvable accuracy of the sensor.

Using these definitions and lemmas, we are now ready to formulate quantitative "RRA" rules, by providing options for the use of calibration, fixturing, and servoing in the workspace. Assume that we wish to position a feature i on part P_1, at the location of feature j on part P_2 with a tolerance "budget" Δk_{12} along each DOF *k*. We use fixture F_1 for part P_1, and end-effector fixture F_2 located on a manipulator R to constrain part P_2. Assume that the uncertainty of locating feature i on part P_1 is known, and denote it by σ_{P1k}, for all *k*. By the same token, we denote the positional uncertainty of feature j located on part by σ_{P2k}.

Rule 1 (Use of fixtures during assembly): Using robot R, position feature j of part P_2 to coincide with feature i of part P_1 (this procedure is sometimes called teaching the place position of part P_2 with robot R). The two features coincide at joint vector q_{12}. Since now we will be changing parts P_1 and P_2 for repeated assemblies, the total uncertainty in the relative positioning of features is given by:

$$\sigma^2_{acc_k} = \sigma^2_{accuracy_k}(q) + \sigma^2_{P1k} + \sigma^2_{P2k} \,. \tag{4.22}$$

Therefore, if we assume that part tolerances are sufficiently small, and if $3\sigma_{accuracy_k} < \Delta k_{12}$, then robot R will succeed in the assembly operation over 99% of the time when it returns to location q_{12}. In addition, the use of fixtures will result in the minimum

assembly time, because only one measurement is necessary, at the expense of an added fixture to the system.

Rule 2 (Use of calibration during assembly): Assume that we have performed calibration for degree of freedom k of a feature located on part P_2, yielding a calibration error $\sigma^2_{calibration_k}(q)$. Since we now have a forward kinematic map, we can use inverse kinematics to obtain the joint coordinate q_{12} that will accomplish the needed relative pose between P_1 and P_2. Therefore, if

$$\sigma^2_{cal12_k} = \sigma^2_{calibration_k}(q) + \sigma^2_{repeat_k}(q) + \sigma^2_{P1k} + \sigma^2_{P2k}, \quad (4.23)$$

and if $3\sigma_{cal12_k} \leq \Delta k_{12}$, then robot R will succeed the assembly operation by returning to location q_{12} with a yield greater than 99%. Since the calibration error can be made arbitrarily close to the sensor resolution by increasing the number of calibration points, and if we assume that this value and the part tolerances are much smaller than the robot repeatability, we can conclude that if $3\sigma_{repeat_k} < \Delta k_{12}$, then a calibration sequence can be found to guarantee an assembly yield greater than 99%. In this case, the use of calibration is required before every assembly operation, and therefore it will result in a lower throughput.

Rule 3 (Use of servoing during assembly): Assume that we are performing visual servoing using two distinct features *i*, and *j* located on parts P_1 and P_2, respectively. If we can measure the relative position of the features along axis k *simultaneously*, and if $3\sigma_{servo_k}(q) \leq \Delta k_{12}$, then robot *R* will succeed the assembly operation by servoing on the relative distance between features with a yield greater than 99%. $\sigma_{servo_k}(q)$ is the resolution of the positioning system along k^{th} axis. Because servoing consists of several iterative steps, the assembly time will be larger than using fixtures, but will be faster than calibration.

4.8.3 Inverse Kinematics for MEMS die attach

After robot calibration, the position of all tools and parts in the workspace can be

expressed with respect to a common coordinate frame. As a result, we can perform assembly with a precision given by:

$$\sigma^2_{cal_k} \geq \sigma^2_{spk} + \sigma^2_{repeat_k}, k \in (x, y), \tag{4.24}$$

$$\sigma^2_{cal_\theta} \geq \sigma^2_{repeat_\theta}, \tag{4.25}$$

and the robots can now be used in open-loop for operations such as insertion, die pick and place, preform pick and place via inverse kinematics.

One of the assembly operations is to align and attach the MOEMS die to the carrier. Inverse kinematics is used to calculate the required pose for the robot R_2 after it has picked the die as follows:

- The camera on manipulator R_1, images the three optical fiber feed-through holes on three sides of the carrier. These locations are computed using camera S_1 and the R_1 kinematics to be at global coordinates (X_{pj}, Y_{pj}, Z_{pj}), where $1 \leq j \leq 3$.
- A MEMS die held by R_2 is presented to camera S_1, which images the center of the three DRIE trenches corresponding to the carrier holes.
- Because not all features of interest on the MEMS die fit within the microscope field of view, an image "stitching" technique is needed in order to express the location of trenches on the MEMS die in platen coordinates. In pixel coordinates, these points are at (P_{xi}, P_{yi}). For example, equation (15) calculates the location of the center of trenches 1 and 2 as (X_{pi}, Y_{pi}), $I = 1,2$. However, these points cannot be imaged in the same CCD pixel frame at high magnification. In order to simulate an infinite FOV for the CCD, i.e. to derive the (X_{p2}, Y_{p2}) vector in the same CCD frame as (P_{x1}, P_{x1}), we calculate the value of (P'_{x2}, P'_{x2}) using (X_{c1}, Y_{c1}) i.e. robot R_1 location when imaging trench 1 from:

$$\begin{bmatrix} P'_{x2} \\ P'_{y2} \end{bmatrix} = M_1^{-1}\left[\begin{bmatrix} X_{p2} \\ Y_{p2} \end{bmatrix} - \begin{bmatrix} X_{c1} \\ Y_{c1} \end{bmatrix}\right]. \tag{4.26}$$

This calculation is repeated for the third trench template and we can eliminate the need to perform kinematic identification for every trench.

- A constrained least squares problem is solved to find the joint coordinates of the R_2 manipulator minimizing the die-carrier error pose. This consists of finding *Xo, Yo, and θo* such that :

$$\min_{X_0, Y_0, \theta_0} \sum_{j=1}^{3} \left(\begin{bmatrix} X_{pj} \\ Y_{pj} \end{bmatrix} - \begin{bmatrix} X_0 \\ Y_0 \end{bmatrix} - \begin{bmatrix} k_1 \\ k_2 \end{bmatrix} - R(\theta_0) \left(M_1 \begin{bmatrix} p_{xij} \\ p_{yij} \end{bmatrix} + \begin{bmatrix} t_1 \\ t_2 \end{bmatrix} \right) \right)^2, \tag{4.27}$$

where $R(\theta_0) = \begin{bmatrix} \cos(\theta_0) & -\sin(\theta_0) \\ \sin(\theta_0) & \cos(\theta_0) \end{bmatrix}$. By assigning

$z_1 = X_0$, $z_2 = Y_0$, $z_3 = \cos(\theta_0)$, $z_4 = \sin(\theta_0)$, the inverse kinematics problem reduces to a constrained LSE:

$$\min_{\substack{z_1, z_2, z_3, z_4 \\ z_3^2 + z_4^2 = 1}} \sum_{j=1}^{3} \left(\begin{bmatrix} z_1 \\ z_2 \end{bmatrix} + \begin{bmatrix} c_{1j} & c_{2j} \\ c_{2j} & -c_{1j} \end{bmatrix} \begin{bmatrix} z_3 \\ z_4 \end{bmatrix} - \begin{bmatrix} v_{1j} \\ v_{2j} \end{bmatrix} \right)^2, \tag{4.28}$$

Where,

$$\begin{aligned} C_{1j} &= p_{xij} r_{11} + p_{yij} r_{12} + t_1, \\ C_{2j} &= p_{xij} r_{21} + p_{yij} r_{22} + t_2, \\ \nu_{1j} &= X_{pj} - k_1, \\ \nu_{2j} &= Y_{pj} - k_2. \end{aligned} \tag{4.29}$$

The constrained LSE has an exact solution that can be found using Lagrange multipliers and the eigen values of a residual matrix. However, for ease of implementation, we used a numerical solution instead, based on the LSQNONLIN function of MATLAB®.

- Finally, the calibration and inverse kinematics solutions must be verified against the required die place accuracy. The MEMS die can be aligned to the carrier within an accuracy of 35 μm in *X* and *Y*, and 0.12° in *θ*, which is well within the original die-to-carrier tolerance requirement. The accuracy calculation is based on comparing the offset of center-point location on the trench with respect to the centerline of the fiber feed-through hole, namely the distances dX_1, dX_2, dY_1.

Table 4.1 R_1 Calibration Results, Camera (Mm) & Pixel Coordinates.

Point	X_c	Y_c	P_x	P_y
1	100	100	421	221.5
2	99.25	100	428.116	374.431
3	99.75	100	423.271	273.455
4	99.75	100.25	372.772	272.852
5	99.25	100.25	377.798	373.624

4.8.4 Visual Servoing

For some of the assembly operations, namely the fiber-in-trench insertion, the required tolerance falls below the lower bound of the error involved in calibration. For example, the tolerance permitted in assembling the optical fiber to the MEMS die is 4 μm. This is below the error of 9.87 μm incurred in calibration of robot R_2. To accomplish fiber insertion using visual servoing of robot R_2 the following sequence of steps were employed:

- Using an inverse kinematic solution, the fiber is inserted into the feed-through hole inside the carrier.

Table 4.2 R_2 Calibration Results, Translation In Mm, Angles In Degrees & Pixel Coordinates.

Pt	X_o	Y_o	θ	P_x	P_y
1	599.021	305.327	77.498	421.634	222.729
2	599.493	305.327	77.498	425.685	325.611
3	599.493	304.751	77.498	308.367	323.351
4	599.493	304.751	77.14	396.221	161.525
5	599.153	304.751	77.752	245.757	368.669
6	598.499	306.001	77.746	497.827	235.384
7	598.499	305.002	77.453	366.04	105.449
8	599.743	304	77.002	282.732	155.685

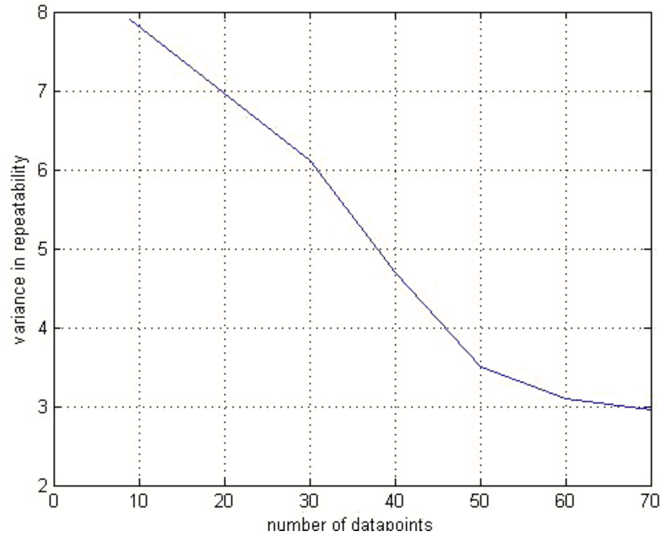

Figure 4.24 Decrease in calibration error (σ_2) with an increase in the number of calibration points.

Table 4.3 Experimental (X,Y) Data (µm) Showing Die To Carrier Misalignment

Experiment	dX_1	dY_1	dX_2
1	34.8	27.12	-31.7
2	-36.26	27.19	-35.82
3	-34.42	-32.18	33.04
4	37.38	23.01	34.1
5	33.82	-23.82	34.91

- The tip of the optical fiber guided through via points into the DRIE trench. These via points and offsets between them are defined using image patterns as shown in Figure 4.24.
- Next step requires an image based Jacobian relating changes in image features (pixels) to corresponding change in robot encoder space as shown in equation 4.30. The pixel error vector $[\Delta P_x, \Delta P_y, \Delta\theta]'$ is used to calculate the required joint actuation vector $[\Delta X_o, \Delta Y_o, \Delta\theta_o]'$.
- Robot R_2 is commanded to execute the positioning correction given by $[\Delta X_o, \Delta Y_o, \Delta\theta_o]$

- The above outlined procedure is executed in a loop to guide the fiber to follow a trajectory defined by imaging the trench and fiber repeatedly.

X_o, Y_o, and θ_o are the joint coordinates of robot R_2, and X_p, Y_p and θ_p be the position and orientation of the fiber tip in global coordinates. The relationship between the pixel measurements using the zoom camera (P_x, P_y) and the location of the fiber in global coordinates is determined. The R_2 manipulator carrying the fiber gripper is calibrated using equations (4.26)-(4.29) to determine the corresponding kinematic parameters:

$[k_1, k_2, t_1, t_2]$= [-156.379, -68.2652, -64.8079, -141.7786],

$[P_{xinit}, P_{yinit}]$ = [123.792, 129.495], and

M_1=[0.011654, -0.000094011; 0.00016128, -0.011695].

These constants are used to calculate the image Jacobian corresponding to R_2 from equation:

$$\begin{bmatrix} \Delta P_x \\ \Delta P_y \end{bmatrix} = M_1^{-1} \left[\begin{bmatrix} \Delta X_o \\ \Delta Y_o \end{bmatrix} + \Delta\theta_o \begin{bmatrix} b_1(\theta_o) \\ b_2(\theta_o) \end{bmatrix} \right], \tag{4.30}$$

in which,

$$\begin{bmatrix} b_1(\theta_0) \\ b_2(\theta_0) \end{bmatrix} = \begin{bmatrix} -\sin(\theta_0) & -\cos(\theta_0) \\ \cos(\theta_0) & -\sin(\theta_0) \end{bmatrix} \left[M_1 \begin{bmatrix} P_{xinit} \\ P_{yinit} \end{bmatrix} + \begin{bmatrix} t_1 \\ t_2 \end{bmatrix} \right]. \tag{4.31}$$

Equation 4.31 can now be rearranged as an image Jacobian:

$$\begin{bmatrix} \Delta P_x \\ \Delta P_y \\ \Delta\theta \end{bmatrix} = J \begin{bmatrix} \Delta X_o \\ \Delta Y_o \\ \Delta\theta_o \end{bmatrix}, J = \begin{bmatrix} M_1^{-1} & M_1^{-1} \begin{bmatrix} b_1(\theta_o) \\ b_2(\theta_o) \end{bmatrix} \\ 0 \quad 0 & 1 \end{bmatrix}. \tag{4.32}$$

Because angle variations are small in microassembly, we can approximate the Jacobian around the origin of the rotation axis of R_2, (θ_o~=0). Based on the calibration parameters:

$$J = J(0) = \begin{bmatrix} 85.817 & -0.68985 & -114.62 \\ 1.1835 & -85.816 & 509.31 \\ 0 & 0 & 1 \end{bmatrix}. \tag{4.33}$$

The overall fiber insertion process can be decomposed into several steps assigned using the *RRA rules*. First, the insertion of the fiber into the carrier can be accomplished via both calibration as well as fixturing because the tolerance budget exceeds the accuracy of robots R_2 and R_3. We chose calibration over fixturing in the case of motion along X, Y and θ because these DOFs are available to the manipulators. At the same time, we chose fixturing in the case of motion along Z and φ because these DOFs are not available to our robots. Finally, the insertion of fibers into the MEMS trench requires a combination of fixtures and visual servoing due to a much tighter tolerance budget.

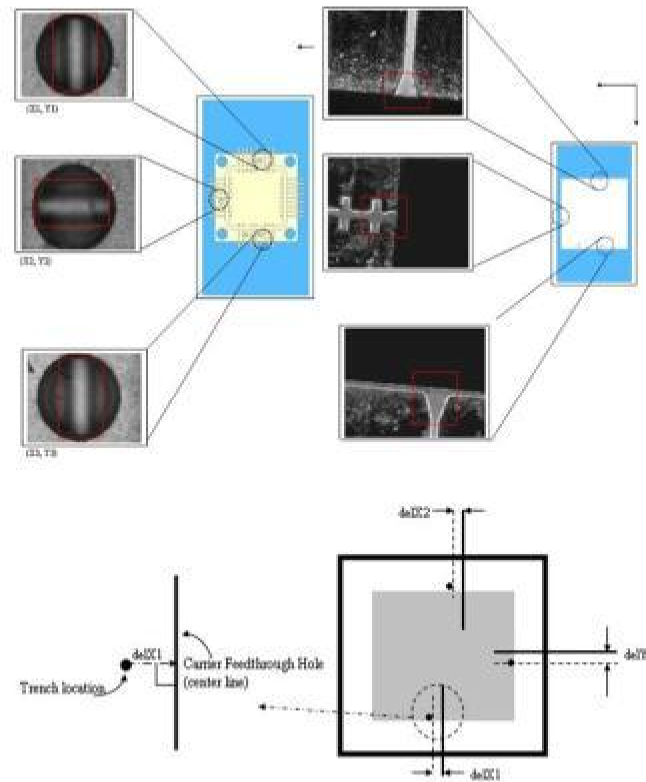

Figure 4.25 Die to carrier misalignment calculation based on imaging of three carrier feed-through holes and three DRIE trenches on the MEMS die.

CHAPTER 5

ARRIPEDE MICROCRAWLER

The mobile microrobot configuration and manufacturing details outlined in chapters 3 and 4 are exemplified using the “ARRIpede” microrobot described in this section.

5.1 Microrobot description

The ARRIpede is an assembled micro crawler designed as a mobile base used to support and transport parts and assemblies in the nano factory. Figures 5.1-5.2 show version 1 prototypes. The micro mechanical part of the robot consists of an array of electrothermal actuators and wire bonds between the substrate and the electronics backpack. The current version design occupies a volume of 12 x 12 x 10 mm^3 and weighs 6g including the power electronics and a Li-Polymer battery. All actuators are fabricated to undergo single degree of freedom prismatic motion.

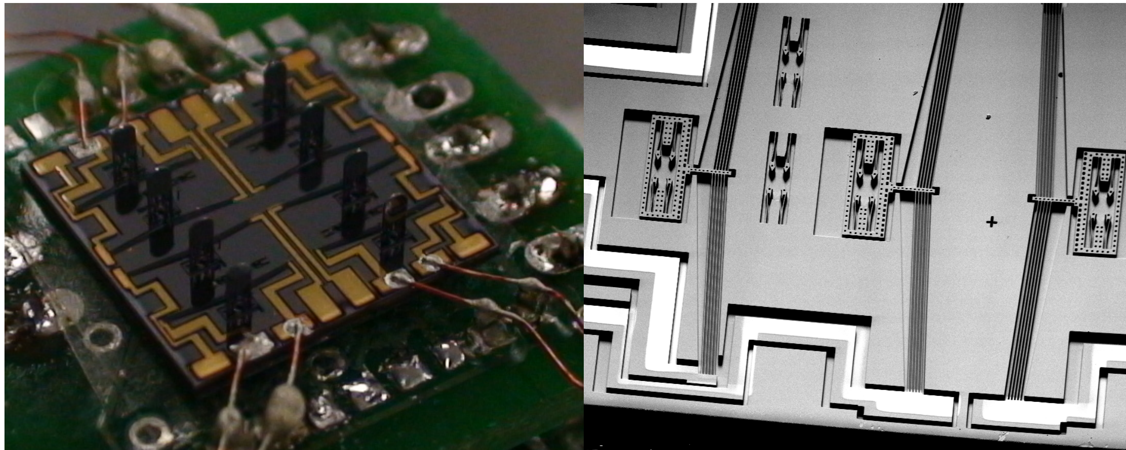

Figure 5.1 Left-ARRIpede belly up with 8 legs; Right-SEM image of prismatic joint.

The prismatic joint consists of a microsnap fastener attached to the electro-thermal actuators shuttle. Silicon legs assembled to these microsnap fasteners move back and forth to create a stick and slip crawling motion. The first ARRIpede prototypes were designed to consist

of 4, 6 and 8 actuated legs. Figure 5.2 shows solid models and pictures of the robot and a microscope image of the leg and joint.

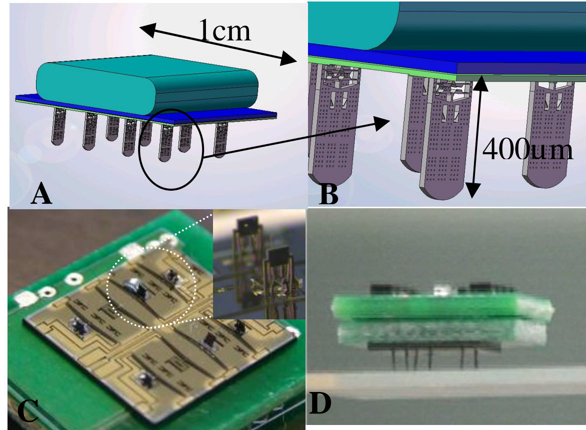

Figure 5.2 ARRIpede description (a) ARRIpede Microcrawler solid model showing legs. b) Leg assembly with thermal prismatic joint; c) Inverted ARRIpede microcrawler carrying electronics backpack; d)Microcrawler carrying a 4g payload.

5.2 Motion Principle and Prismatic Joint Design

The principle of motion is based on stick-and-slip, and can be understood by referring to Figure 5.3 (f~h). When actuated, the joint causes the robot body to move by a distance X_1 and the leg to slips by X_2^a in the opposing direction. The leg remains in this state until the joint is powered down, after which the leg is pulled back by the native stiffness of the actuator to a new position X_2^b. The magnitudes of displacements X_1,X_2^a and X_2^b depend on design and environmental parameters such as friction, actuator characteristics and factors such as robot mass, the number of legs, actuation cycle etc.

The ARRIpede legs consist of assembled MEMS parts such as an actuated socket, the leg joint and a boot. The first ARRIpede prototype was constructed without the boots. The body~leg joint assembly includes a compliant microsnap fastener. These micro snapfasteners are used to mechanically interconnect microparts, or to fixture them to a substrate. Relative large friction forces generated in grippers and assembly "sockets" firmly hold parts during and after assembly. In addition to elastic deformation and friction, the socket is reinforced with UV

curable high viscosity epoxy so that it has a much higher force and moment carrying ability.. For a 4/6/8 legged ARRIpede, the Chevron actuator is designed for a large horizontal displacement, up to 50µm. It consists of seven pairs of 15 µm wide, 1mm long and 100 µm thick beams. The beams are separated by 10 µm and form an angle of 3.5°to the shuttle arm that connects to the socket. The assembled socket displacement was experimentally characterized using a Veeco ® DMEMS optical profiler. Electrothermal MEMS actuators have a first order dynamic transfer function between the input power and displacement. Our designs exhibit a current draw of approximately 50mA at 10V inputs, 18 µm steady-state displacements, and 250mA at 19V with 48 µm displacements. The measured actuator bandwidth is dictated by thermal effects (as opposed by mechanical resonance), and was measured to be 50 Hz.

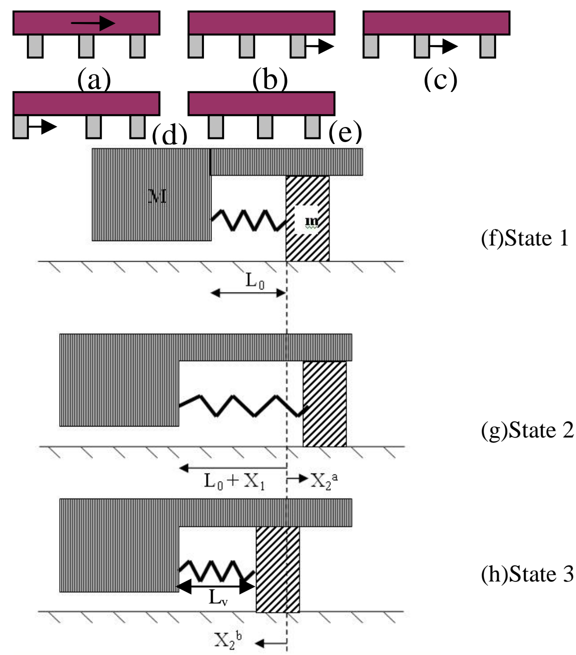

Figure 5.3 ARRIpede wave gait over one step. (a)~(e) depict complete robot and figures (f)~(h) refer to a single leg.

5.3 Microfabrication and Assembly

The ARRIpede mechanical components fabrication is accomplished using Deep Reactive Ion Etching on Silicon on Insulator Wafers. Figure 5.4 shows the layout drawing of the belly and the legs. Post fabrication, the legs are detethered from the substrate and assembled onto the belly substrate using $2^1/_2$D assembly procedure described in chapter 3.

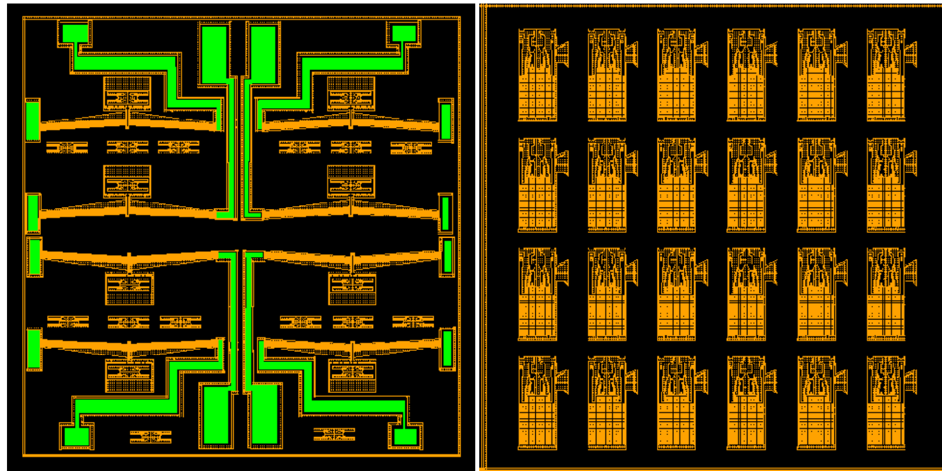

Figure 5.4 ARRIpede layout diagram using LASI®.

5.4 Backpack Electronics

The thermal actuator used in this microcrawler, typically required up to 15V at 200mA during actuation. If we actuate all legs simultaneously, we would impose a high power consumption rate for the robot. As a result, we divided every cycle of the carrier PWM signal into sequence of high frequency (1 kHz) pulses sent to different actuators. However, at any given instance of time there is current flowing to only one actuator, and the load on the power electronics is reduced by 1/N, where 'N' is the number of active legs, at a cost of $1/\sqrt{N}$ to the amplitude of motion. A DSP microcontroller (PIC33F) circuit is used to generate the required input actuation profile and generate the leg sequence to perform the wave gait.

The ARRIpede microrobot power module and control electronics are carried by the microrobot as a "backpack". This consists of a 3.7V, 600mA-hour Lithium Polymer battery that

weighs 1.1g and measures 1cm x 0.8 cm x 0.4 cm. The voltage regulator shown in figures 5.5 measures 1.2cm x1.2 cm and weighs 1.1g. It consists of a Switch Mode Power Supply that can supply up to 27V output from the 3.7V battery. The current regulator circuit weighs 0.7g and can supply 300mA current switched into 8 channels (actuators).

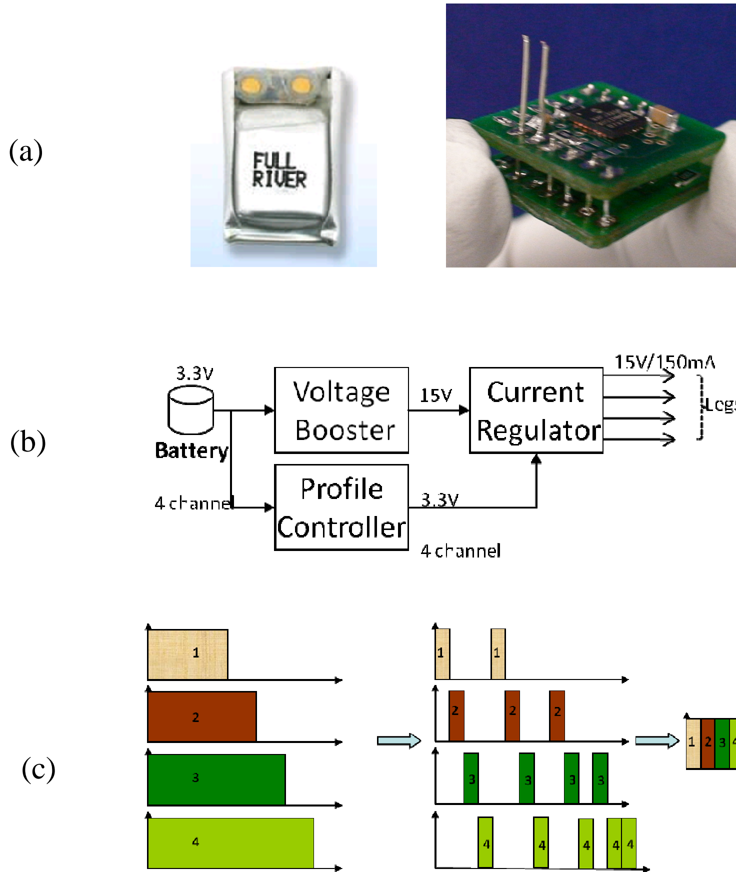

Figure 5.5 Electronics Backpack. (a) Backpack components (b) Power supply schematic; (b) High frequency multiplexing of input pulses to the ARRIpede.

The total power consumption is thus equivalent to one electrothermal actuator, e.g. 500 mW maximum. The current draw from a supercapacitor, or from a lithium polymer cell such as the LP30 FR Bahoma rated at 3.3V/30mAh would then be 180mA. This implies that the battery would run out after 10 minutes of untethered microrobot operation. However, the run-out time

can be increased by a factor of 100 by operating the microcrawler at lower speeds (around 0.3 mm/s) using only 5mW power draw.

In order to accommodate the high frequency multiplexing of the actuator array , the dynamical model of the microrobot is re-represented as a discrete vector field nonholonomic dynamical model that predicts robot trajectories with high frequency multiplexing of power between all the legs.

5.5 Leg joint strength estimation

In this section we describe experiments with the ARRIpede leg assembly to determine leg joint strength. We use a SensorOne® AE-800 series micro-cantilever for our experiments. This sensor was mounted onto the μ^3 M_1 robot, and pushed against an assembled leg to obtain force measurements as shown in the figure 5.6 (a,b). During these experiments, the average joint strength of the epoxy bonded joint was measured to be 28.5mN. The joint strength influences the maximum payload carrying capacity of the robot. Figure 5.6(c) shows a leg misaligned by up to 1° during assembly. The component of the robot mass + payload acting perpendicular to this joint is given by:

$$F_h = \frac{M}{N} g\cos(\theta). \quad (5.1)$$

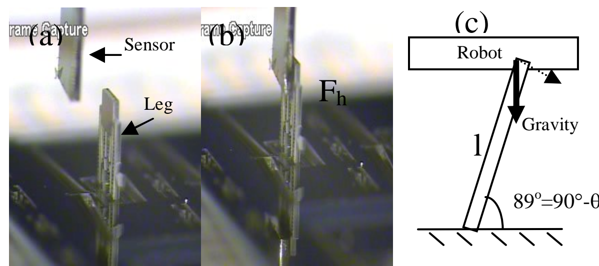

Figure 5.6 Joint strength determination. (a), (b) Microforce sensor measuring joint strength of ARRIpede; (c) Microrobot weight acting on a misaligned leg.

5.6 Packaging

As outlined in section 4.7.2.2, ARRIpede packaging includes the integration of the micro mechanical module with the electronics module and the battery. A detailed model of the package is illustrated in figure 5.7. Figure 5.8 shows a picture of the electronics backpack. The first version of the completed package measures a total volume of 17x17x15mm^3 and weighs 4.5g including the battery. The backpack shown consists of a voltage booster, current regulator, and controller circuits. In designing this package, the total number of SMD (surface mount device) components to be accommodated were 27.

In order to minimize the micro robot span (area from the top), the electronics modules were stacked on top of each other vertically. The PCB stack is supported and electrically interconnected using vertical standoff's as shown. The controller module and the voltage booster module were integrated on two sides of the same board while the second board is designed with regulator circuit on one side with room for attaching the substrate on the other side.

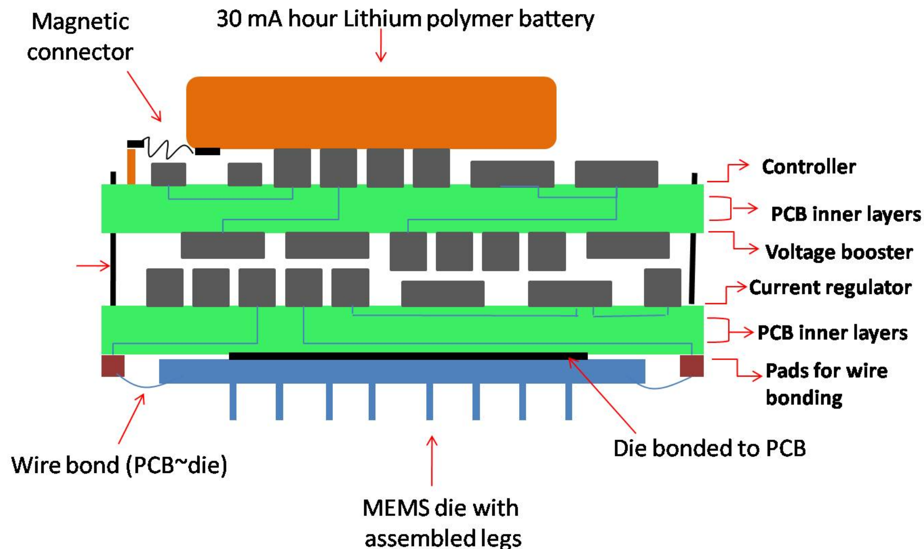

Figure 5.7 Complete ARRIpede Package.

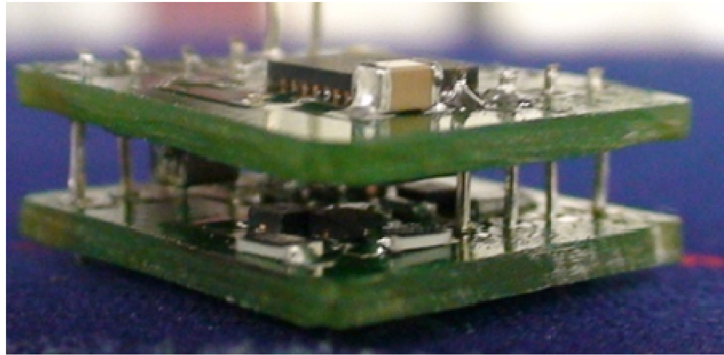

Figure 5.8 Electronics Backpack.

5.7 Gait and dynamic analysis

5.7.1 ARRIpede Gait

The ARRIpede is programmed to execute a 'wave' gait, according to the following sequence:

- In the first step, all joints are actuated concurrently. Due to the relatively large power consumption of individual actuators, we multiplex the same output current to each actuator. The joints are deactivated one after the other in a sequence. The leg is retracted due to slip.
- The dynamics of this repeated action cause the robot body to move forward and the leg to slip in the backward direction.

Referring back to the static force conditions outlined in section 3.4, gives a better understanding of the wave gait. The conditions described are also used as factors in deciding the type of actuation technology to be designed.

5.7.2. Dynamics

The ARRIpede parameters used for dynamic analysis using a lump model consists of: *M,* the mass of the robot payload (not including the mass of the legs); *m*, the mass of each of the *N* legs; L_o, the unactuated prismatic joint length; L_v, the net distance following depowering

when the legs return to equilibrium; X_1, the displacement of the microrobot with a single step taken; $X_2(=X_2^a+X_2^b)$, the total slip at each leg during a single step, where X_2^a is the slip backward during actuation, and X_2^b is the slip due to retraction when the joint is deactivated; K, the actuator stiffness; μ_{1d} and μ_{1s}, the coefficients of dynamic and static friction between the robot leg and surface on which the robot walks; μ_{2d} and μ_{2s}, the coefficients of dynamic and static friction between the microsnap fastener socket and the robot belly; B_1, the damping coefficient between the leg and the floor; B_2, the damping coefficient between the socket and the robot belly. Referring to figure 5.3, there exist three states of equilibrium during the ARRIpede gait:

- **State 1**: The joints of the microrobot are in an "un-actuated" state.
- **State 2:** '*N*' prismatic joints are actuated simultaneously.

  In this case, the equations of motion for the body with a Coulomb friction model can be written as:

$$Mx_1 + B_1x_1 + NK(x_1 + x_2{}^a - (L_o - L_V)) = \mu_2 Mg\,sgn(x_1 + x_2^a), \tag{5.2}$$

  and the equilibrium condition for the leg becomes:

$$mx_2^a + B_2x_2^a + K(x_1 + x_2{}^a - (L_o - L_v)) = \frac{(\mu_1 + \mu_2)Mg}{N} sgn(x_1). \tag{5.3}$$

- **State 3:** The legs are retracted one after the other and thus an equilibrium position is reached between the friction forces and the stiffness of the actuator. In this case:

$$mx_2^b + B_2x_2^b + K(x_1 + x_2{}^b - (L_o - L_v)) = \frac{(\mu_1 + \mu_2)Mg}{N} sgn(x_1). \tag{5.4}$$

Formulating the friction model at all states, it is important to consider both the absolute velocity of the leg and the relative velocity of the leg with respect to the body, and also the static and dynamic friction conditions. This determines the existence of static or dynamic friction forces at the leg~floor interface and leg~body interface.

Denoting: $a_1 = sgn(x_1 + x_2), a_2 = sgn(x_2)$, define:

$$F_{2_push} = NK(x_1 + x_2 - L_v) + B_1 x_1, \tag{5.5}$$

$$F_{1_push} = NK(x_1 + x_2 - L_v) + NB_2 x_2. \tag{5.6}$$

We can then separate the following friction conditions:

- **Case(i):** if $abs(x_2) > \varepsilon; (\varepsilon \approx 0)$

$$F_{fri_1} = -a_2 \mu_{1d} (M + Nm) g. \tag{5.7}$$

This is the case when the leg is either slipping in state 2 or retracting in state 3. Also,

$$\text{if } abs(x_1 + x_2) > \varepsilon \Rightarrow F_{fri_2} = -a_1 \mu_{1d} Mg. \tag{5.8}$$

This is the case when there is relative motion between the body and leg. Finally, if case (i) is not valid at any given time, then:

$$F_{fri_2} = (F_{2_push} - \frac{M}{m} F_{fri_1} + \frac{M}{m} F_{1_push})(1 + \frac{M}{m}). \tag{5.9}$$

- **Case (ii):** if $abs(x_2) = 0$,

i.e., when leg is stationary, and if $abs(x_1 + x_2) > \varepsilon$, then the robot is moving forward, therefore we need to use the dynamic coefficient of friction:

$$F_{fri_2} = -a_1 Mg \mu_{2d},$$

$$F_{fri_1} = F_{1_push} - F_{fri_2}. \tag{5.10}$$

However, if $abs(x_1 + x_2) = 0$, denote:

$$F_{fri_2} = F_{2_push}. \tag{5.11}$$

- **Case(iii)**

If this force is greater than the static friction force, i.e. if $abs(F_{fri_2}) > \mu_{2s} Mg$, then

$$F_{fri_2} = -a_2 Mg \mu_{2d}, \tag{5.12}$$

$$F_{fri_1} = F_{1_push} - F_{fri_2}. \tag{5.13}$$

Finally, at any given time, if:

$$abs(F_{fri_1}) > \mu_{1s}(M + Nm)g, \tag{5.14}$$

Then, we can use the dynamic coefficient of friction to evaluate the friction force between the leg and the surface underneath:

$$F_{fri_1} = -a_1(M + Nm)g\mu_{1d}\,. \tag{5.15}$$

Upon actuation, the robot moves forward by a distance X_1, while the leg slips backward X_2^a. After this, the leg is retracted by a distance X_2^b when the joint is deactivated. It is to be noted that with the exception of the first step, the distance $X_2^a = X_2^b$ during the subsequent steps, the legs slip and retract by the same distance.

The ARRIpede dynamics has been simulated to determine an optimum configuration for the microrobot and evaluate the effect of different gaits. For the simulation, the microrobot payload was 3.8g (button battery-mass=0.9g, electronics-mass=1.8g, MEMS die-mass =1.1g), the joint stiffness was 185N/m, derived from a FEA electro-thermo-mechanical simulation of the thermal actuator and validated experimentally, viscous damping at the joints was 0.1Ns/m, N=6 (number of legs), and the coefficients of friction at the leg-floor interface and at the joint-body interface are considered as variables.

Figure 5.9 shows the variation in robot step size with varying friction coefficients. The coefficients are equal if the robot slides across a silicon surface. In simulation we pick a static friction coefficient to be slightly higher than the dynamic ones. The coefficients of static and dynamic friction are same at the leg~body and leg~ground as the ARRIpede was experimentally validated for motion control on silicon surfaces. From figures 5.9(a) and (b), we observe that with increased friction there is a reduction in the amount of leg retraction after each forward motion. This reduces the robot speed. An input frequency of 45Hz at 10V with six legs, coupled with friction coefficients of 0.4 and 0.33 for static and dynamic friction results in a displacement of 18.5 μm/step. This is in close agreement with the actual microrobot displacement under similar conditions listed in Table 5.1. For input conditions of 25V/180mA, and actuation frequency of 65Hz, the stick-slip model results in step size of 43μm and a velocity of 2.795

mm/s. However, such a high velocity imposes high power requirements from the electronic backpack and additional energy conservation techniques are needed

5.8 Experimental Characterization

This section describes experimentation to validate the ARRIpede concept. An inverted prototype with 6 legs as a conveyor, and manipulated a 4 cm X 4 cm X 1mm silicon die as a payload (figure 5.10). This payload weighs approximately the same as a robot supporting its own weight (4g). The microcrawler legs are actuated under varying amplitudes and frequencies to control the position of the payload. Referring to figure 5.10, the product of the amplitude with the frequency of actuation, which gives a measure of the leg velocity, is used as the control parameter to steer the robot. For example, when looking towards the direction of motion, consider the case when the legs on the right are actuated at higher velocity than the legs on the left, i.e.

$$A_1 f_1 < A_2 f_2, \tag{5.16}$$

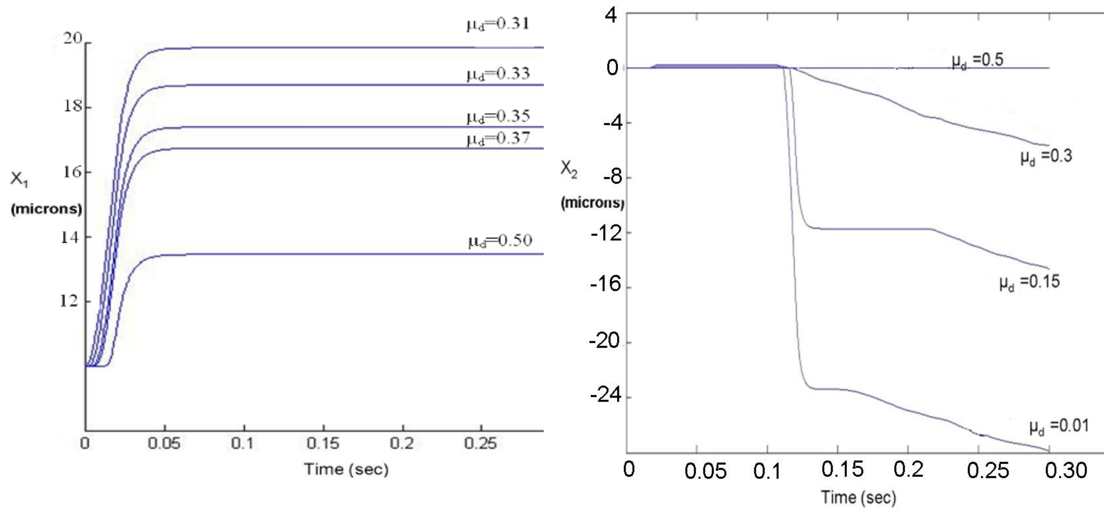

Figure 5.9 ARRIpede microrobot displacement per cycle for different friction models. The drift observed in X_2 is a numerical artifact and is overcomes by the execution of a subsequent step in the gait sequence.

where $A_{1,2}$ represent the amplitude of motion, and $f_{1,2}$ represent the frequency. Differential velocity between the two sides results in the robot steering left. The rationale for the amplitude-frequency product controlling the velocity of the robot is counterintuitive, since electrothermal actuators are nonlinear. As a result, we expected that at frequencies close or higher to the thermal bandwidth (50Hz), the attainable velocities are proportional to the square of the amplitude-frequency product. This effect was compared with experimental data shown in Table 5.2. A maximum, unpredicted 1.55mm/s speed was recorded in case #5 when actuated at 135Hz and 10V.Figures 5.12(a,b) show X and Y displacement for the following conditions of ARRIpede leg velocity:

- All legs are actuated to move with the same velocity. We experimented with combinations of frequency and amplitude resulting in the similar velocities and verified experimentally the resulting displacement of the robot.
- The set of legs on the left are actuated at higher frequency-amplitude products leads to steering towards the right.
- The set of legs on the right are actuated at higher frequency-amplitude products leads to steering towards the right. The amount of drift steering is similar.

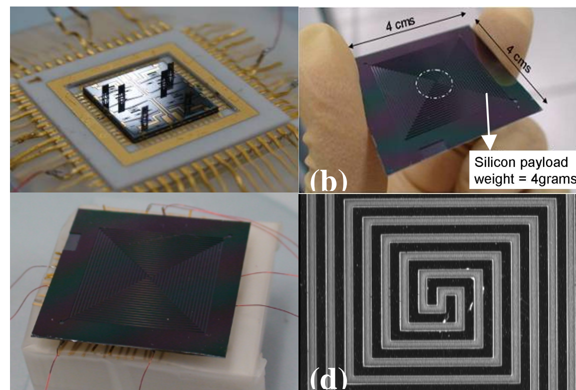

Figure 5.10 Experimenting payload conveyance on ARRIpede with belly-up position. (a) ARRIpede in belly-up position with six legs,(b) Silicon payload,(c) Payload on the legs,(d) 0.7X zoom-in view of the feature on the payload used for tracking.

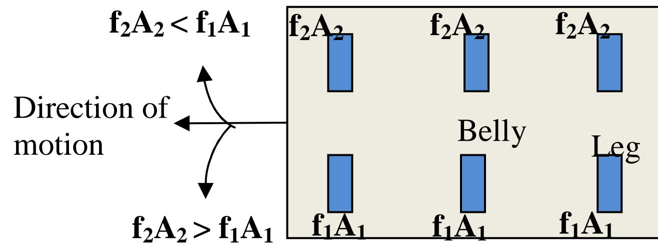

Figure 5.11 ARRIpede in a six legged configuration. The leg velocity given by A_1f_1(amplitude.frequency) is controlled to steer the microcrawler and compensate lateral drift during straight line motion.

During these experiments micro scale features located on top of the payload are tracked using a 0.7X microscope lens, and using IMAQ® machine vision software we determined their location. These features are fabricated using the SOI DRIE process on the silicon payload. Figure 5.12 and 5.13 show end positions reached by the vision template during the different actuation cycles, including drive forward, steer left and right.

Table 5.1 Robot speed results from vision data for forward motion, and the effect of the amplitude-frequency product.

#	A_1=A_2 (Volts)	f (Hz)	$(Af)^2$	Forward Velocity (mm/s)	Velocity from simulation (mm/s)	$\frac{Af}{\sqrt{V}}$
1	10	f1=f2=15	22500	0.365	0.312	410
2	10	f1=f2=45	202500	0.84	0.832	535
3	15	f1=f2=30	202500	0.83	0.810	542
4	10	f1=f2=90	810000	0.74	0.790	1216
5	10	f1=f2=135	1,822,500	1.55	0.648	870

Table 5.2 ARRIpede steering data.

#	A_1(V)	f_1(Hz)	A_2(V)	f_2(Hz)	$(A_1f_1)^2$	$(A_2f_2)^2$	ω rad/s
1	10	45	10	30	202500	90000	0.062
2	10	45	10	15	202500	22500	0.075
3	10	15	10	45	22500	202500	0.078
4	10	30	10	45	90000	202500	0.057

The input voltage has a 20% duty cycle and is modulated between legs on a 1 kHz carrier and therefore, the effective frequency content is above the thermal resonance even for

case #1 in table 4.2. From the results, it can be seen that the velocity is not quite linear in the frequency-amplitude product, and that the robot velocity at 90Hz is lower than the one at 45Hz.

Clearly, additional factors, such as un-modeled thermal actuator effects, and bending mechanical resonance might come into play to account for the discrepancy. From the simulation results in figure 5.9, for the case when the robot is crawling over a surface with dynamic friction coefficient of 0.31, the body is displaced by approximately 20 μm per cycle. This amounts to a displacement of 9 mm in 10 seconds which is close to the experimentally determined displacement in case #2.

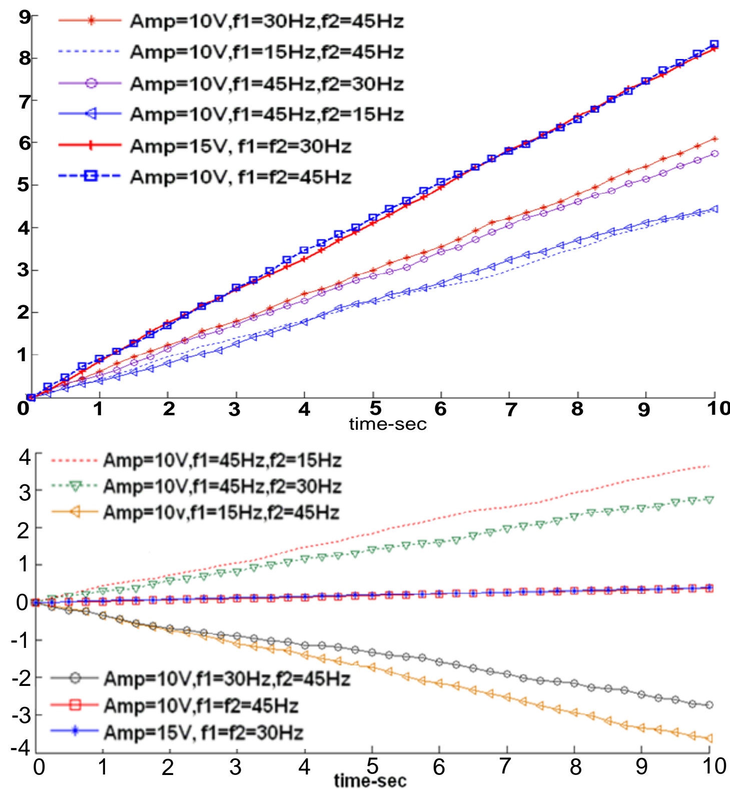

Figure 5.12 Displacement profiles. (a) ARRIpede forward motion along X (mm) for varying amplitude and frequencies (b) Drift sideways along Y axis (mm).

5.9 Modified Dynamics for Closed Loop Control

State vector representing the ARRIpede position in a planar world coordinate frame is:

$$q_{body} = \begin{bmatrix} q_{body_trans} \\ q_{body_rot} \end{bmatrix} = \begin{bmatrix} X_c & Y_c & \theta_c \end{bmatrix}^T, \quad (5.17)$$

where, (X_c,Y_c) are the Cartesian coordinates of the center of the robot and 'θ_c' is its orientation. In addition to the position of its body, the robot consists of N legs, which displace relative to the body. Their positions relative to a coordinate frame fixed onto the robot body is:

$$q_{legs} = \begin{bmatrix} q_1 & q_2 & ,,, & q_N \end{bmatrix} = \begin{bmatrix} x_1 & x_2 & x_3 & . & . & x_N \\ y_1 & y_2 & y_3 & . & . & y_N \\ \theta_1 & \theta_2 & \theta_3 & . & . & \theta_N \end{bmatrix}, \quad 1 \quad (5.18)$$

where q_i represents the state of leg i. Referring to figure 5.14, denoting the actuation direction as x_i, and due to the fact that the prismatic electrothermal actuators are designed with high stiffness along the y_i and θ_I directions it is safe to assume.

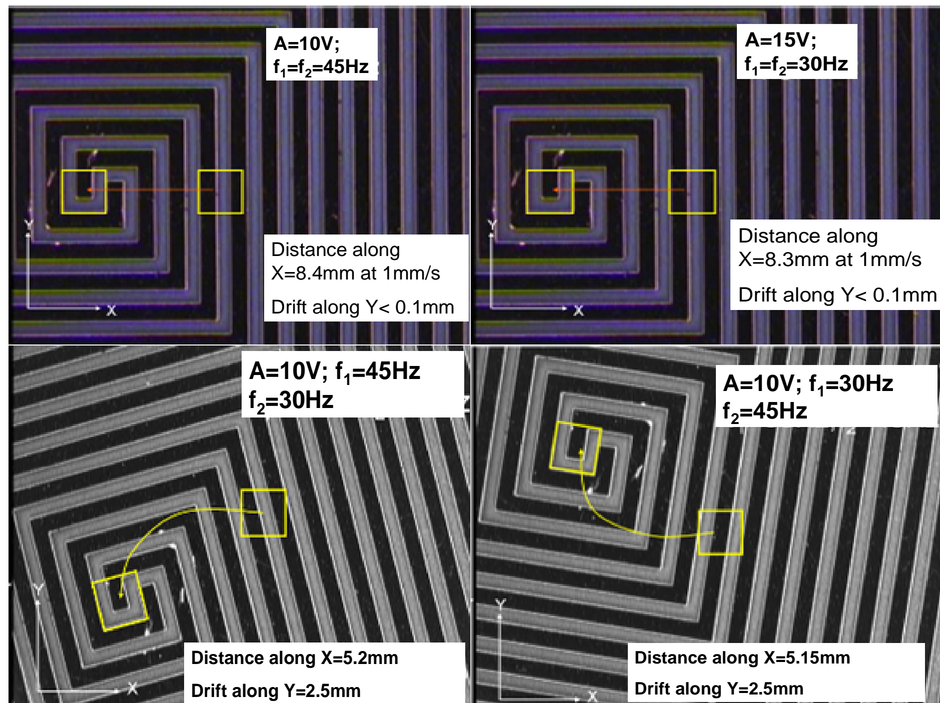

Figure 5.13 Payload tracked in conveyor mode. (a) ,(b) Forward motion for varying amplitude and frequencies with constant amplitude-frequency products; (c) -steering left,(d) steering right- with mismatched actuation frequencies

$$y_i(t) = const, i = 1..N, \text{and}$$
$$\theta_1 = \theta_2 = ... = \theta_N = const \approx 0 \quad (5.19)$$

Next, a quantitative relationship between the actuation pattern in the leg array and the resulting motion of the body is derived. The ARRIpede leg model can be represented by the free-body diagram in figure 5.14 a, with a resulting equation of motion given by equation (5.20):

$$m_{leg}\ddot{q}_{leg(i)} + m_{leg}g[(\mu_{d1_c} + \mu_{d2_c})q_{leg(i)} + (\mu_{d1_v})\dot{q}_{leg(i)} = \psi_i(A_k f_a f_m),$$

(5.20)

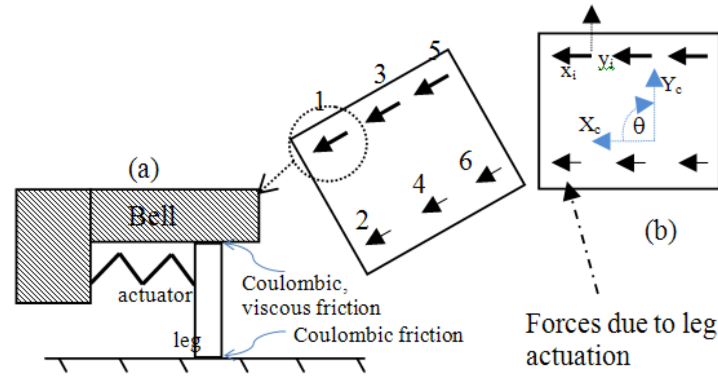

Figure 5.14 Revised model description. (a) ARRIpede leg~belly and leg~ground interface and types of friction (b): Vector fields controlling robot orientation; legs depowered in the sequence shown 1~6.

where 'm_{leg}' is the mass of each leg, 'μ_{d1-c}'and 'μ_{d2-c}' are the Coulombic friction coefficients between the leg~belly and leg~ground respectively, μ_{d1-v}' is the coefficient of viscous friction , '*Ψ'* is the force generated due to the electrothermal expansion of the actuator and 'τ' is the net force generated by the 'i^{th}' leg during one actuation cycle.

The force *Ψ* generated at specific electrothermal actuator locations is controlled by the input signal amplitude, gait frequency and the frequency at which the PWM's are multiplexed as shown in equation (5.21):

$$F_{ki} = \psi_i(A_i, f_{ai}, f_{mi}), \quad (5.21)$$

and can be represented by a first order transfer function as shown in equation 5.22.

$$F_{ki}(s) = \frac{b}{s + 2\pi f_{mi}} A_{ki}^{2}. \tag{5.22}$$

The basis for equation (5.22) is due to the fact that the thermal bandwidth of electrothermal actuators is typically an order of magnitude smaller than the first mechanical resonant mode and can often be represented using a first order pole transfer function. Also, the actuation displacement profile follows a nonlinear quadratic profile proportional to the square of the amplitude due to Joule heating effects. This relationship and the constant 'b' can be fitted to the force model shown in equation 5.20 using experimental data.

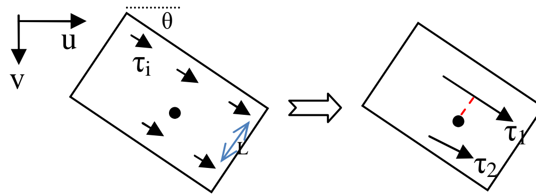

Figure 5.15 Representation of net force with respect to the center of mass.

The net force and moment at center of mass due to the discrete force field is the resultant of leg forces on the left and right sides of the robot, respectively:

$$\tau_1 = \sum_{i=1}^{N_{left}} \psi_i \ , \tau_2 = \sum_{i=1}^{N_{right}} \psi_i \ , \tag{5.23}$$

in which N_{left} and N_{right} are legs on either sides of the center of mass. The linear force and angular torque acting on the robot body due to two vectors τ_1 and τ_2 can be represented by:

$$\tau_{lin} = \tau_1 + \tau_2, \tau_{ang} = \frac{L(\tau_1 - \tau_2)}{2}, \tag{5.24}$$

where L is the distance between the two longitudinal arrays of legs as shown in figure 5.15. The robot dynamics can be recovered using the Euler Lagrange approach and reduces to a second order differential equations with kinematic constraints given by:

$$m_{body(3x3)} \ddot{q}_{body} = R_{3x2} \begin{bmatrix} \tau_1 \\ \tau_2 \end{bmatrix} + \begin{bmatrix} \sin\theta_c \\ -\cos\theta_c \end{bmatrix} \lambda \tag{5.25}$$

$$m_{body(3x3)} = \begin{bmatrix} m_{body} & 0 & 0 \\ 0 & m_{body} & 0 \\ 0 & 0 & I_{zz} \end{bmatrix}; R_{3x2} = \begin{bmatrix} \cos\theta_c & \cos\theta_c \\ \sin\theta_c & \sin\theta_c \\ \frac{L}{2} & -\frac{L}{2} \end{bmatrix}, \tag{5.26}$$

where, 'λ' is a Lagrange multiplier, R_{3x2} transforms the forces from the local coordinate frame to the body shown in equation 5.26 . From equations 5.24 to 5.26, we can write:

$$\ddot{x}_c = \frac{\tau_{lin}}{m_{body}} \cos\theta_c + \frac{\lambda}{m_{body}} \sin\theta_c,$$

.

$$\ddot{y}_c = \frac{\tau_{lin}}{m_{body}} \sin\theta_c + \frac{\lambda}{m_{body}} \cos\theta$$

$$\ddot{\theta}_c = \frac{\tau_{ang}}{I_{zz}}. \tag{5.27}$$

If v and w are the linear and angular velocities of the mobile robot in global frame, their relation to the robot body coordinates becomes:

$$\dot{q}_{body} = \begin{bmatrix} \cos\theta_c & 0 \\ \sin\theta_c & 0 \\ 0 & 1 \end{bmatrix} \begin{bmatrix} v \\ w \end{bmatrix}, \tag{5.28}$$

Differentiating equation (62) we get,

$$\ddot{x} = -v\dot{\theta}_c \sin\theta_c + \dot{v}\cos\theta_c.$$
$$\ddot{y} = v\dot{\theta}_c \cos\theta_c + \dot{v}\sin\theta_c. \tag{5.29}$$
$$\ddot{\theta}_c = \dot{w}.$$

Comparing equations 5.27 and 5.29 we can represent the dynamic variables as shown in equation 5.30;

$$\begin{bmatrix} \dot{v} \\ \dot{w} \\ \dot{x}_c \\ \dot{y}_c \\ \dot{\theta}_c \end{bmatrix} = \begin{bmatrix} \frac{1}{m_{body}} \\ 0 \\ 0 \\ 0 \\ 0 \end{bmatrix} \tau_{lin} + \begin{bmatrix} 0 \\ \frac{1}{I_{zz}} \\ 0 \\ 0 \\ 0 \end{bmatrix} \tau_{ang} + \begin{bmatrix} 0 \\ 0 \\ v\cos(\theta) \\ v\sin(\theta) \\ w \end{bmatrix}, \tag{5.30}$$

Equations 5.29~5.30 represent the revised dynamics of the ARRIpede crawling. The advantage of this 5th order model over the previous model is that it allows implementation of closed loop control. This model was simulated using MATLAB/Simulink. A custom designed pulse generator block allows control of input parameters [A_{left}^2, A_{right}^2, F_{left}, F_{right}] and is also designed to perform the high frequency multiplexing of the signals. By varying the input frequency and amplitude across six legs pulsing at 1000Hz, the resulting trajectories are shown in figure 5.16. For this simulation, the microrobot mass is assumed as 4g (including mass of the backpack electronics) and the number of legs is 6. The deactivating sequence of the legs during the wave gait also influences the trajectory followed. For example, in figure 5.16 the ARRIpede trajectory when all legs are actuated at 45 Hz and 15V shows a slight lateral (left side) drift.

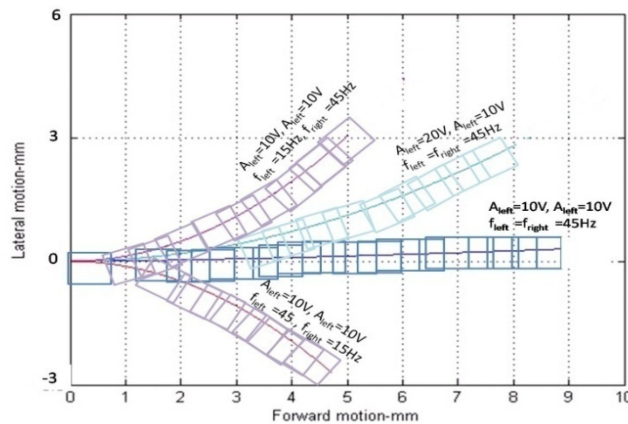

Figure 5.16 ARRIpede simulated motion for varying input amplitudes and frequencies.

5.10 Motion Control

The hierarchical control structure for ARRIpede is shown in figure 5.17. The controller consists of two loops, the coarse control loop and the fine control loop, each relaying position feedback over different precision regimes. The two control schemes and factors that govern switching decisions are highlighted in sections 5.10.1 and 5.10.2.

5.10.1 Coarse tracking controller

The coarse control of the ARRIpede body can be accomplished using a proportional LQR controller that tracks a desired trajectory with gain 'k_{coarse}' combined with a high

magnification optical microscope camera placed vertically above the body for feedback. The camera tracks fiducials marked on top the robot with a resolution of 2μm at a magnification of 4.5X. When used at 1X magnification, the associated field of view is 1cm x 0.8 cm and thus the range of motion that can be detected is limited to this. The range can be extended by mounting the microscope on a XY gantry.

5.10.2 Fine tracking controller

The low resolution drawback of the coarse controller can be enhanced using a Keyance LK-G10® laser displacement with 10nm displacement resolution. In future experiments, this will allow evaluation of the ARRIpede positioning precision The range of motion that can be sensed is 2mm with a working distance of 10mm. Three displacement sensors measure incremental motion along X and Y axes. In order to reflect the 30μm laser spot, we assembled mirrors vertically off the ARRIpede belly.

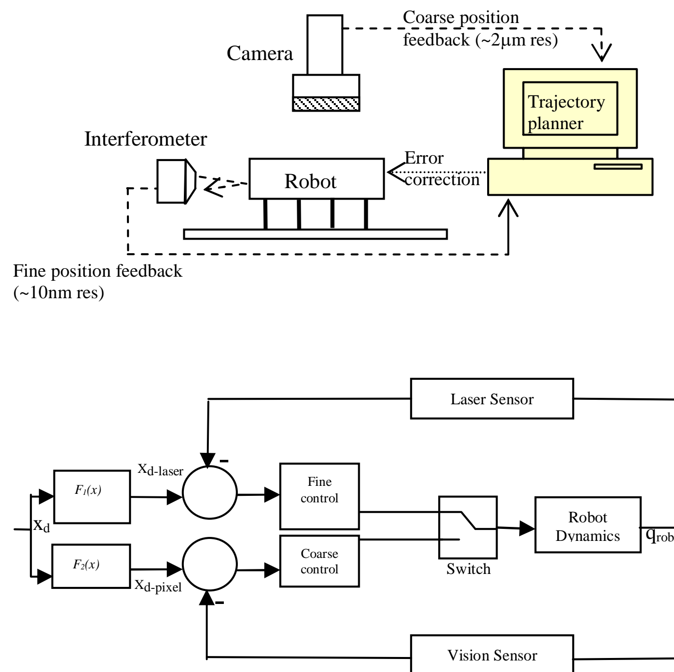

Figure 5.17 Experimental verification of displacement profile; (a) Hardware setup diagram, (b) Coarse Fine Controller Implementation

The factors governing the decision to use either of these sensors can be listed as follows:

- Range of motion: The high magnification CCD camera covers a higher range of motion (~1cm^2 in XY) when compared to the displacement sensor (4mm^2).
- Resolution: The Keyence displacement sensor detects a motion resolution of 10nm, when compared to the 2µm pixel accuracy of the CCD.
- Feedback rate: The data acquisition and processing rate achievable using a CCD based vision system is limited to 15fps while the displacement sensor can measure upto 75MHz.

5.10.3 Trajectory Tracker

A Linear Quadratic Regulator (LQR) trajectory tracker is used for implementing closed loop control. The trajectory tracker stabilizes a nonlinear variation time-varying system about the desired (feedforward) trajectory [101]. The desired trajectory is derived from the path planner described in the previous section and the tracking controller then guarantees that the system will follow the desired trajectory. For ease of notation, we replace the state vector notation 'q_{body}' with a simple 'q'. The discrete form of the linearized system equation is:

$$\delta q(k+1) = A_d(k)\delta q(k) + B_d(k)\delta u(k); \delta q(0) = 0, \tag{5.31}$$

Where, A_d and B_d are the discrete versions of the state and input Jacobian variational matrices of (5.32):

$$A_d(k) = \begin{bmatrix} 0 & 0 & 0 & 0 & 0 \\ 0 & 0 & 0 & 0 & 0 \\ \cos\theta(k) & 0 & 0 & 0 & -v(k)\sin\theta(k) \\ \sin\theta(k) & 0 & 0 & 0 & v(k)\cos\theta(k) \\ 0 & 1 & 0 & 0 & 0 \end{bmatrix}, \; B_d = \begin{bmatrix} 1/m_{body} & 0 & 0 & 0 & 0 \\ 0 & 1/I_{zz} & 0 & 0 & 0 \end{bmatrix}^T. \tag{5.32}$$

The control law can be expressed as a feed forward control (which would drive an ideal system along the desired trajectory) and a feedback part that regulates the (non ideal) linearized system to zero. Thus we can represent the control law in discrete form as:

$$u(k) = u_f(k) + K(k)(q_d(k) - \hat{q}(k)), \tag{5.33}$$

Where $u(k) = [\tau_{k_lin}\ \tau_{k_ang}]$ is the discretized closed-loop leg force signal, $u_f(k)$ is the nominal path-planned input, K(*k*) is a LQR matrix gain, $q_d(k)$ is the desired state of the microrobot generated through simulating the nominal model with the feedforward input $u_f(k)$, and $\hat{q}(k)$ is the estimated microrobot state estimate resulting from measurements. In order to calculate the LQR gain, we define a state-input cost function given by,

$$J = \frac{1}{2}\sum_{k=0}^{\infty}(q^T(k)Q.q(k) + u^T(k)Ru(k)) , \tag{5.34}$$

A standard Ricatti iteration can be used to calculate the gain matrix K(k):

$$K(k) = [B_d(k)P(k+1)B(k) + R(k)]^{-1} + B_d(k)P(k+1)A(k)$$

$$P(k) = A_d(k)P(k+1)[A(k) - B(k)K(k)]^{-1} + Q(k) , \tag{5.35}$$

Where, *P*(k) is the end configuration weighting matrix, *Q*(*k*) is the configuration weighting matrix and *R*(*k*) is the control weighting matrix. Figure 5.18 depicts a control block diagram implementing the linear quadratic regulator. The desired input can be the trajectory generated from the path planner described in section 5.7 or any other desired trajectory (straight line or turning). The feed forward inputs are $[\tau_{lin}\ \tau_{ang}]$. Figure 5.19 shows simulation results comparing the open and closed loop performance.

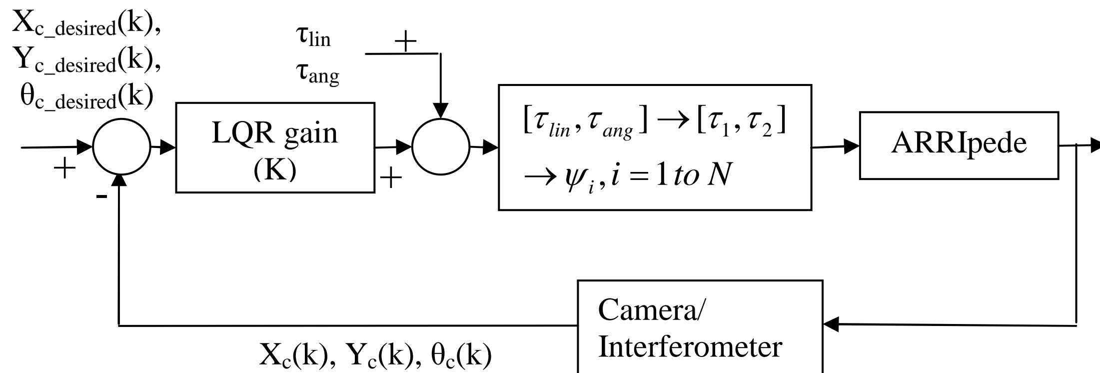

Figure 5.18 Control Block Diagram of the LQR Controller.

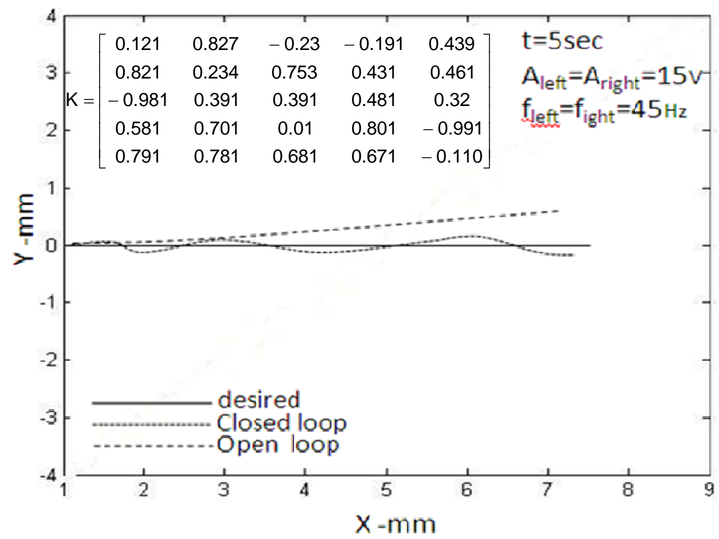

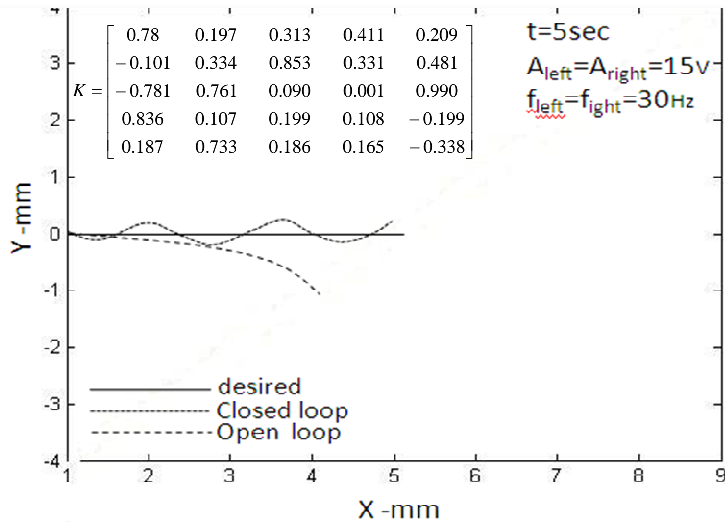

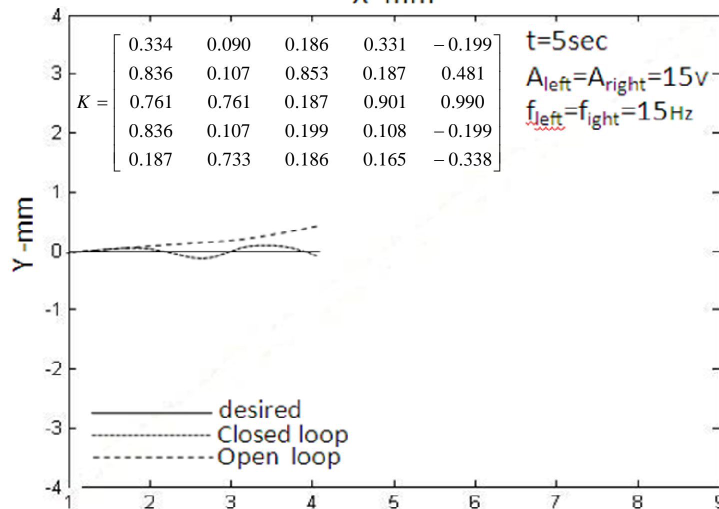

Figure 5.19 LQR controller simulations at various actuation frequencies.

5.11 Precision Measurements

Following successful manufacturing, the microrobot precision is determined using an interferometer-based experimental setup shown in figure 5.20. The precision metrics to be determined included the open and closed loop positioning repeatability of the microcrawler and the actuation resolution of the electrothermal actuators. As shown in figure 5.20, the precision measurement setup included interferometers measuring the displacement along X and Y. The sensors chosen were Keyence LK-G10 series with a measurement resolution of 10nm and a range of 2mm. The sensors were aligned to reflect light off the ARRIpede legs and thus measured the robot displacement in $XY\theta$ as well as the displacement resolution of individual legs. As shown in figure 5.20, the measured parameters include incremental motion ΔX and ΔY. Using this technique, the angle of rotation and the radius of center of rotation are given by

$$\Delta\theta = a\tan\left(\frac{\Delta x}{\Delta y}\right) \quad , \tag{5.36}$$

$$R = \frac{1}{2}\left(\Delta x^2 + \Delta y^2\right)^{1/2} \operatorname{cosec}\left(\frac{\pi}{2} - \theta\right) \quad . \tag{5.37}$$

The LQR controller was implemented for a pre-determined and time invariant gain matrix ‘K’. The controller is implemented via National Instruments hardware and a Labview VI. In order to record positioning data, the robot actuators were driven to operate between 15 to 1005Hz in steps of 15Hz, and at each step actuated 10 times for 10 seconds. The variance in the actual positions reached indicates the repeatability. Figure 5.20 b shows the variation of the robot repeatability along the X plane of motion.

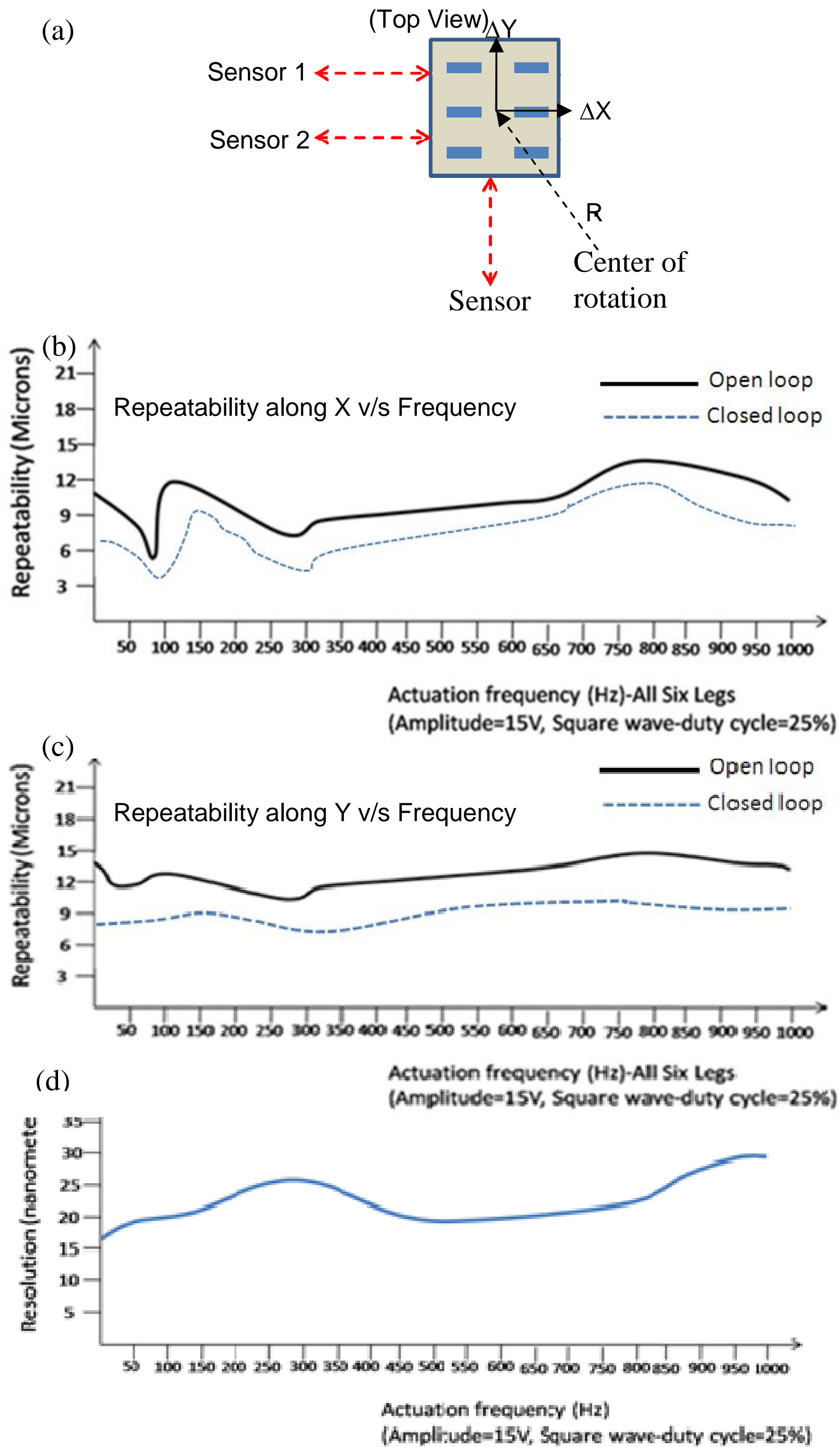

Figure 5.20 ARRIpede precision measurements. (a) Setup; (b) Repeatability along X; (c) Repeatability along Y; (d) Electrothermal actuator resolution.

As seen from this repeatability plot, the robot is repeatable within a range of 3μm at 75Hz to around 15μm at 1005Hz. Thus, while operating close to its thermal bandwidth, the robot is repeatable to within a single step. This finding is very encouraging particularly with the goal to manufacture this robot for nano positioning applications and actuator resolution with actuation frequency. Furthermore, the motion resolution of the robot is around 20 nm, close to the measurement resolution of the interferometer setup.

CHAPTER 6

ARTICULATED FOUR AXIS MICRO ROBOT (AFAM)

6.1 Introduction

The AFAM is a unique 3D micro robot designed for micro and nano manipulation tasks. In its present version the robot spans 3x2x1 mm^3 with a measured work volume of 50x50x75μm^3. Designed to incorporate in-plane actuator banks coupled with in-plane and out-of-plane transmission systems, this micro robot is capable of atleast 100mN force output along all three axes with four degrees of freedom (X, Y, Pitch, Yaw). This robot is repeatable to 100nm along

A Scanning Electron Microscope (SEM) image of microrobot is shown in figure 6.1. For clarity in understanding the working principle, a solid model is shown in figure 6.2. Referring to this figure, two sets of in-plane XY actuator stages drive the micro robot's 4 DOF. The poses of the tool coordinate point (TCP) are obtained via two prismatic (X_{TIP}, Y_{IP}) and two revolute (φ_{pitch}, ψ_{yaw}) motions. In the design evaluated in this paper, the *XY* stages are identical, and occupy a total span of 3mm x 2mm. One of the stages (arm drive stage) drives a microsnap-fastener on which a 800μm tall flexure arm is vertically assembled. The actuator pair on this stage displaces the base along axes denoted by X_D and Y_D, the subscript '*D*' representing direct coupling to the base.

The second *XY* stage pulls a 30 μm thick, 3.2mm long "*cable*" that is bonded to the flexure arm on the other end. The actuator pair on this stage drives a vertical flexure arm via the cable, along axes denoted by X_C and Y_C. The XY stages comprise of Chevron (V shaped) type electrothermal actuators coupled through flexures. Four independent pose parameters of the TCP can be achieved through a combination of planar motions by these actuators. A summary of a typical actuation sequence for the robot and the resulting motion at the TCP is outlined in

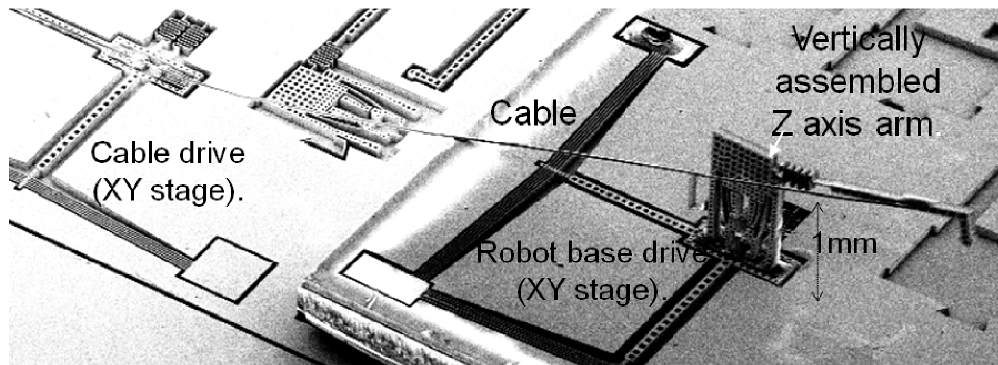

Figure 6.1 Scanning Electron Microscope of the AFAM.

Table 6.1 Actuator to joint relationships.

Actuator powered	Joints Actuated (including coupling)
X_D	Mostly Pitch(φ), Some Yaw (ψ)
X_C , X_D	Mostly X, Some Y
Y_D	Mostly Yaw (ψ) , Some Pitch(φ),
Y_C , Y_D	Mostly Y, Some X
X_C , X_D, Y_C , Y_D	X,Y
X_D, Y_D	Pitch(φ),Yaw (ψ)

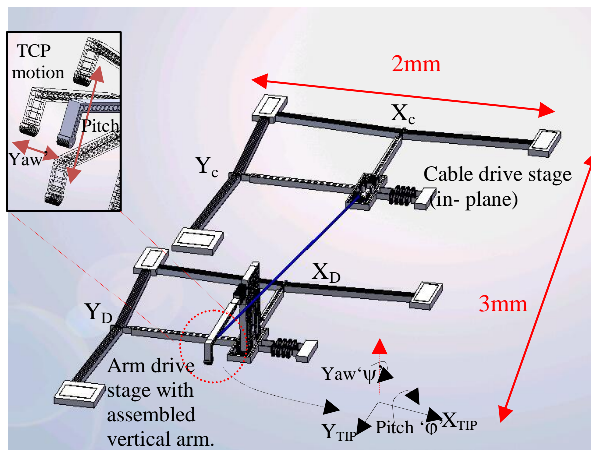

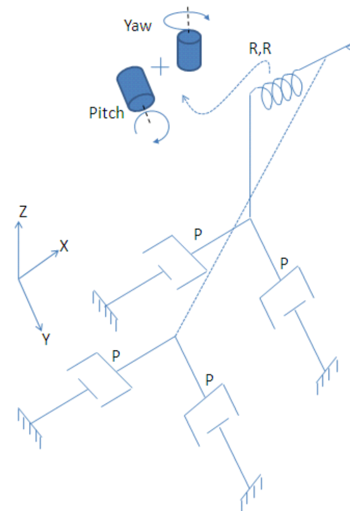

Figure 6.2 Solid model of the microrobot and DOF notation and Kinematic Representation (P:Prismatic; R: Revolute).

table 6.1. Pure translational motion along X_{TIP} and Y_{TIP} requires that both X_C and X_D or Y_C and Y_D be actuated by the same displacement. Vertical TCP motion is a result of the pitch motion of the arm through the cable when X_C and X_D are not actuated by the same displacement.

6.2 Design Methodology

The design steps for the first version of the microrobot are outlined in figure 6.3. A chevron beam electrothermal actuator is designed to produce the required planar deflections, while maintaining its torsional stiffness. Torsional stiffness (Nm^2/rad), the product of the modulus of rigidity with the torsion constant gives a measure of the angular deflection induced per unit length due to unit moment applied.

We incorporated a coupled XY flexure stage into the design and a Z axis flexure on the vertical arm based on the TCP displacement and the actuation inputs from the XY stage. The XY stage must provide enough support and stiffness to allow controlled displacements for the Z axis arm, including sufficient stiffness against reaction torque due to the vertical arm pitch and yaw motion. Finally, the cable length, diameter, angle to Z-arm and attachment location along the cantilever length were selected in order to maximize transmission of the force generated by in-plane actuators. In practice, this sequence may be iterated multiple times to suit a specific force or displacement requirement at the tool tip.

The two *XY* stages driving the microrobot joints were designed with the following requirements:

- To allow a large displacement of the center stage in the plane of the die.
- To resist out of plane bending torques when the pitch and yaw axes are actuated.
- To maximize the retention force of the assembled out of plane arm in the snap-fastener socket.

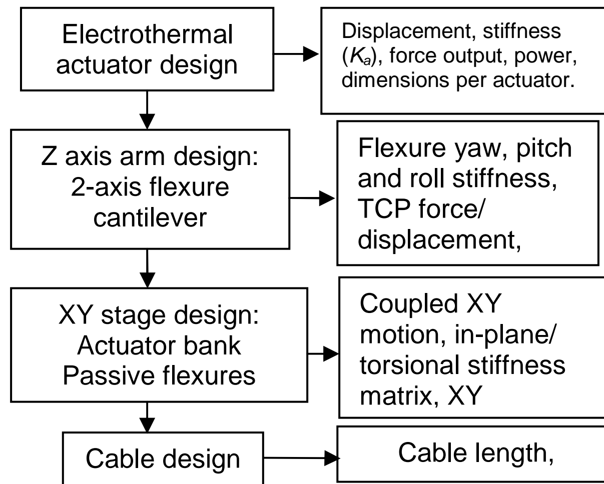

Figure 6.3 Microrobot design sequence and parameters.

The electrothermal Chevron actuators are designed for a horizontal displacement of up to 50μm. They consist of seven pairs of 15 μm wide, 1mm long and 100 μm thick beams. The beams are separated by 10 μm and form an angle of 3.5° to the shuttle arm that connects to the socket. Our designs exhibit a current draw of approximately 50mA at 10V inputs, 18 μm steady-state displacements, and 250mA at 19V with 48 μm displacements with a stiffness of 180N/m with a maximum operating voltage of 20V with current draw of 280mA. The measured actuator bandwidth was 45Hz, and is dictated by thermal effects (as opposed by mechanical resonance). The actuators produce up to 50mN of force output at maximum voltage inputs. At the center of the X_DY_D stage is a micro snap-fastener shuttle, designed to receive an out-of-plane assembly of the vertical Z axis arm.

The shuttle is supported at two ends by the actuator bank and at one other end by passive in-plane flexure springs as shown in figure 6.4 (top). The flexures add to the torsional stiffness of the shuttle and they are designed for varying number of turns *n*, width of each coil *w* and the number of these flexural elements in the XY stage *N*. This choice of *XY* stage design including the actuator and passive flexure design was optimized for maximizing the shuttle displacement and maintaining the required torsional stiffness along the shuttle pitch, yaw and roll axes using Finite Element Analysis. Figure 6.5 shows *XY* displacement and stiffness along

the pitch direction for different iterations of the design. Figure 6.5(a) shows the displacement for n=8, w=10μm and N=2; figure 6.5(b) shows displacement for n=6, w=10μm and N=4, and figure 6.5(c) is displacement profile for n= 4, w=10μm and N=2. Ideally, the shuttle motion should be planar, along two DOFs, and each actuator should control its own DOF. However, due to the fact that the two actuators are both connected to the shuttle, its XY motion is coupled, resulting in undesirable drift along the orthogonal axis. The size of the actuator arms, and the stiffness of the springs have been selected close to decoupling, and then experimentally evaluated using a microscope. For the fabricated design these were 0.26 N-m^2/rad along the pitch and roll axes and 0.12 N-m^2/rad along the yaw axes (e.g. case a). Coupling compensation using kinematic identification of the microrobot XY and Z stage was carried out experimentally after fabrication and assembly as described in section IV.

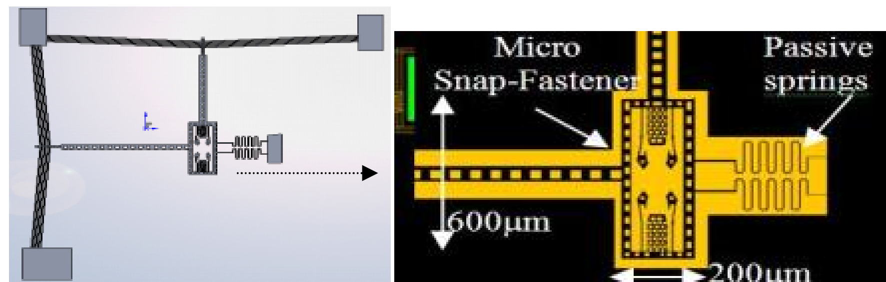

Figure 6.4 XY stage design.

The diagram of the Z axis arm of the microrobot, along with its flexure is shown in figure 6.6. The lower end of the arm is a pair of flexures with the Zyvex snap-fastener design, and is used for assembly onto the $X_D Y_D$ shuttle stage. It also includes a compliant region used for gripping the part for pickup with a “jammer” during assembly, and a guide to release the gripper after mating with the snap-fastener. The upper part of the Z axis arm contains a two degree of freedom flexure supporting a 800 μm horizontal cantilever arm. The flexure consists of 8 spring turns, which together are 400μm long, 150μm wide and 100μm deep with a stiffness equal to 90N/m along the pitch φ axis, and 140N/m on the yaw ψ axis.

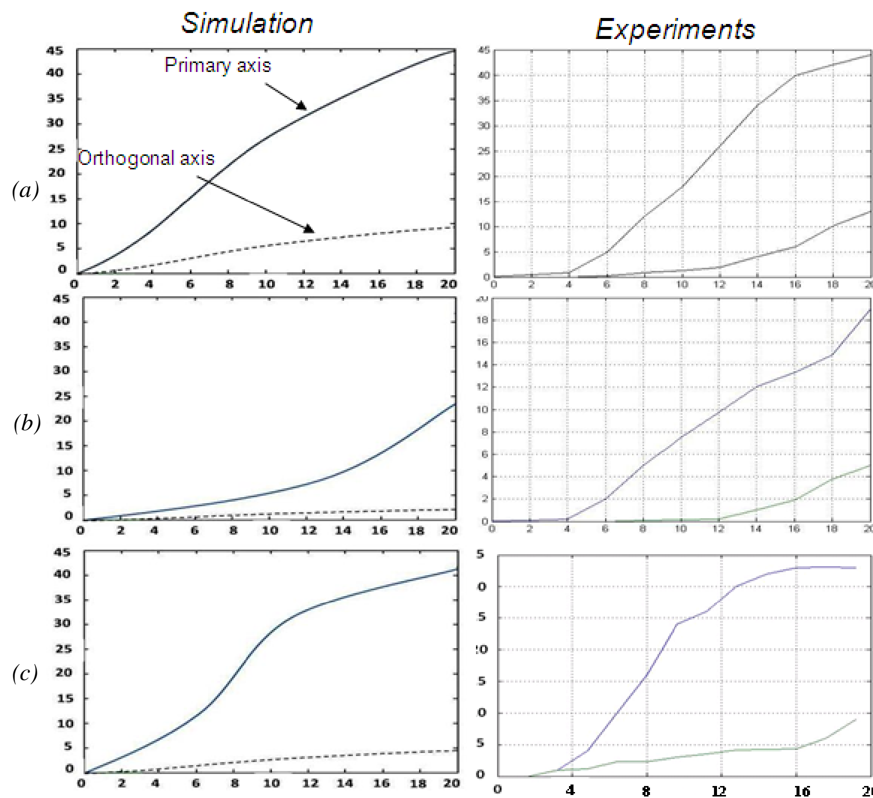

Figure 6.5 XY Stage performance evaluation using FEA and experiments. (a)~(c) left column: Simulated axis and coupled axis motion profile for various flexure parameters-(a): Higher displacement (45 microns) and low torsional rigidity(0.26 N-m^2/rad); (b) Medium deflection (40 microns) and medium torsional rigidity (0.38 N-m^2/rad); (c) Low deflection (24 microns) and high torsional rigidity (0.5 N-m^2/rad); right column- experimentally measured displacements.

The length of the cable and its point of attachment on the arm constrains the angle at which forces are transmitted through the cable. The deflection produced at the cable attachment point P is amplified at the TCP by a factor of L_o/d, while the output force is reduced by the same factor. Thus a smaller d is desired if we want to obtain higher TCP displacement outputs, while a larger d is needed for higher force outputs. FEA analysis on the Z axis arm was conducted to determine, the optimum cable angle, the distance d from the end of the arm and cable length that results in maximum force output at the point P along the $-Y_P$ axis. This also ensures maximum deflection of the cantilever with the TCP. Maximum force is transmitted when this angle is 45°. At this angle, the cable needs to be attached at a distance d=200 μm from the tip for maximum force and displacement transmission. After determining the cable angle and d, we determine the cable length L_c using:

$$L_C = \frac{L_X - d}{\cos\theta}, \qquad (7.1)$$

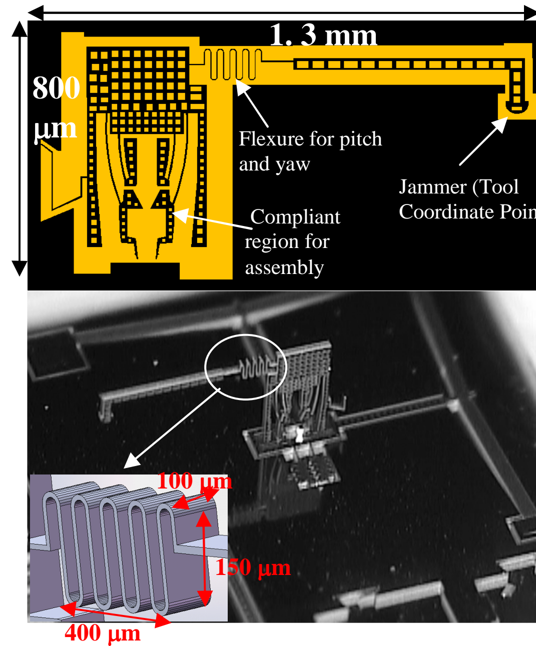

Figure 6.6 Z axis arm.

where L_x is the distance between the center of the XY stage driving the cable and the tip of the z axis arm projected onto the plane of the die, $d=200\mu m$ and $\theta=45^o$. Using equation 7.1, we determine $L_c=3.2mm$.

6.3 Fabrication & Assembly

6.3.1. Fabrication

Fabrication procedure included Deep Reactive Ion Etching (DRIE) on Silicon on Insulator (SOI) substrates with a 100μm thick device layer to fabricate all robot links, joints and actuators, with the exception of the cable transmission. More details on the fabrication procedure is described in chapter 4. The cable made of Copper and 30μm was purchased off the shelf and cut to the required length using a EXCIMER 248nm laser.

6.3.2. Z Stage and Cable Assembly

Post fabrication, the Z-arm is picked up, rotated by 90 degrees, and vertically assembled by means of compliant snap-fastening, resulting in the design depicted in Figure 6.6. The microassembly operation is automated using the μ^3 system located at UT Arlington's Texas Microfactory. More information on the snap-fastener design and assembly methodology can be found in chapter 4. Once assembled, the joint strength of the *Z*-arm is increased using UV curable epoxy dispensed at the joint. The joint strength before failure is evaluated extensively in the past, and exceeded 100mN when loaded in the weaker Y direction. After bonding, the stiffness of this joint will be much larger than the robot's remaining flexures, so it can be described as "rigid".

The cable used in constructing the first version of the microrobot is a 30μm diameter Copper wire with PVC coating. This provides added strength, and the cable behaves more as a tight rod, rather than a flexible tether. The cable was gripped using a Femto Tools® FT100 electrostatic microgripper mounted on the terminal roll degree of freedom on one of the robots in the μ^3 system. Using machine vision through a microscope, the cable was oriented at approximately 45 degrees with respect to the die and the two ends of the cable are epoxy bonded to the microrobot. The cable assembly is depicted in figure 6.7.

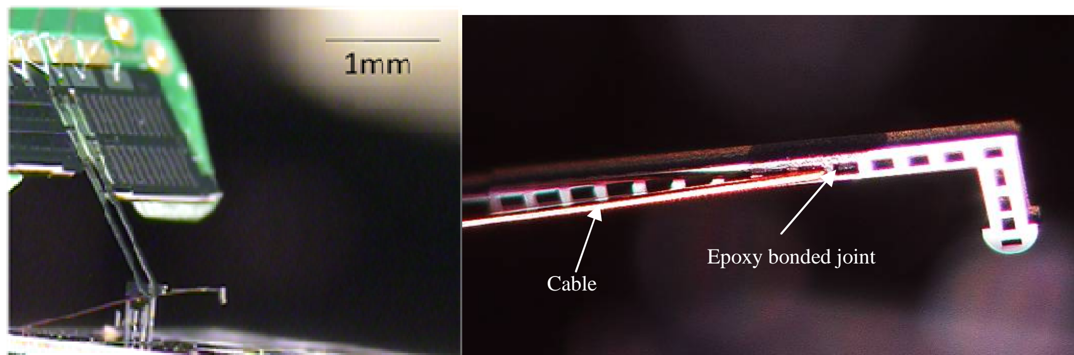

Figure 6.7 Cable assembly.

6.3.3. AFM probe mounting

In order to investigate and demonstrate possible applications of the microrobot in a nano manipulation scenario, we mounted a Veeco ® DP-10 AFM probe onto the TCP, as shown in figure 6.8. The probe is attached to a custom designed micro-fixture designed with a triangular groove that fits the thin arms of the AFM cantilever. Following this, epoxy is dispensed along the groove to bond the probe. The robot TCP ~ fixture assembly is accomplished using a compliant snap fastener. The probe attachment fixture and completed assembly are shown in figure 6.9.

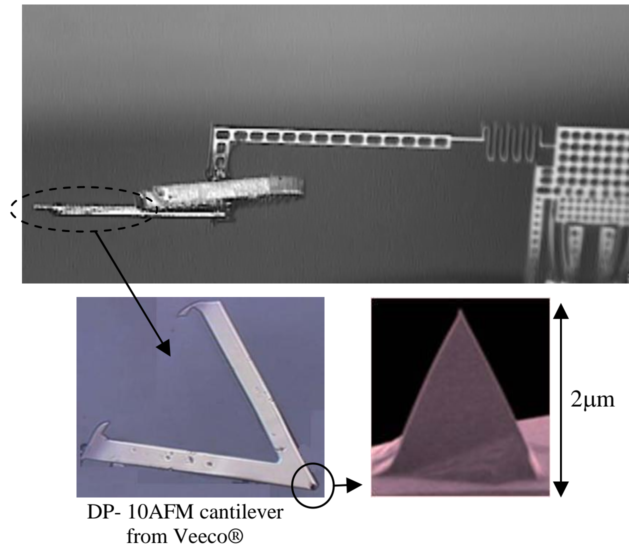

Figure 6.8 AFM probe mounted onto microrobot using a micro fixture.

6.4 Experimental Characterization

6.4.1 Work Envelope Measurement

Post assembly, the microrobot workspace volume, e.g. the volume in 3D space reached by the TCP, is measured experimentally. When the four actuators are sequentially swept from zero to their maximum displacement position, the robot TCP passes through the 3D shape shown in figure 6.9. Using two high zoom camera views mounted perpendicular to the TCP, we

recorded the locations reached. As shown in the figure, the workspace volume is not a parallelepiped, but shows a reduction in the achievable vertical displacements towards the end of the shuttle maximum horizontal displacement. The wedge shaped work volume can be attributed to the parallel configuration of this microrobot with the cable and the vertical arm driven by the two XY stages.

The knowledge of the workspace allows us to plan various assembly tasks using the end effector.

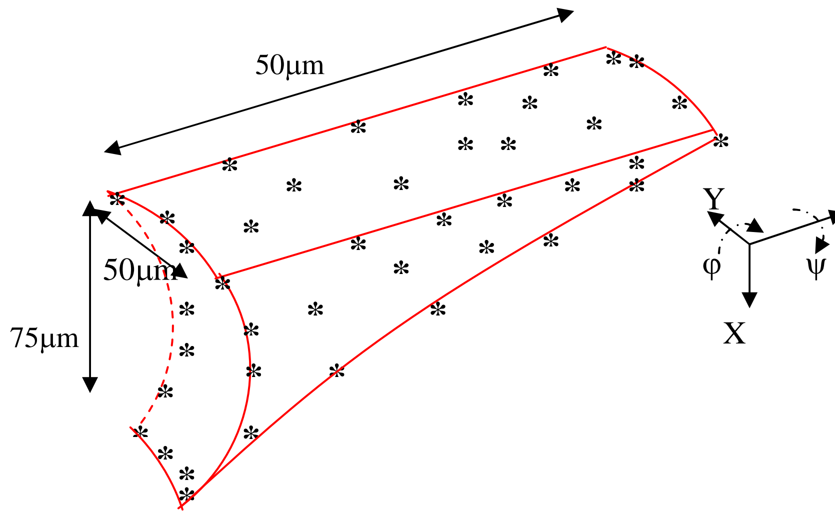

Figure 6.9 Microrobot work volume evaluation (points mark locations reached during volume sweep).

6.4.2. System Jacobian

The four degrees of freedom of the microrobot are highly coupled and it is necessary to establish its kinematics that relates inputs at the actuator level to the corresponding output motion of the tool coordinate point. The data used to determine the work volume is also used to approximate the microrobot Jacobian. In order to characterize the motion of the TCP, the four actuators are powered using various voltages, and using two high magnification microscopes (10X and 4.5X) we tracked the motion output of the features. The top view camera was used to measure Y and yaw while the side view camera measures X and pitch. Some of the data recorded is shown in table 6.2.The TCP velocity in global coordinates relates to the individual actuator inputs by a robot Jacobian J, given by:

$$\begin{bmatrix} \Delta X_{tip} & \Delta Y_{tip} & \Delta\varphi & \Delta\psi \end{bmatrix}^T = J\begin{bmatrix} \Delta X_D & \Delta Y_D & \Delta X_C & \Delta Y_C \end{bmatrix}^T. \tag{7.2}$$

Table 6.2 Sample measured displacement data at TCP.

X_d Y_d X_c Y_c (Volts)	Side View ΔX, $\Delta\varphi$	Top View ΔY, $\Delta\psi$
0 0 0 0	0 μm ,0°	0 μm ,0°
20 0 0 0	-25 μm ,11.1°	7.1 μm ,2.3°
20 0 20 0	-45.1μm, 1.7°	6.8μm, 0°
0 0 0 20	8.1 μm, 0°	27.1μm, 6.2°
0 20 0 20	0 μm ,0°	42.8μm, 0°
20 20 20 20	46.5μm, 0°	44.9μm, 0°
0 0 0 10	3.2 μm, 0°	12.2μm, 2.2°
0 10 0 10	0 μm ,0°	21.3μm, 0°
10 0 0 0	-12.1μm ,3.1°	3.1 μm ,0.9°
10 0 10 0	-23.1μm, 1°	3.8μm, 0°

The Jacobian is state dependent, but a simple approximation using a constant will still be useful for visual servoing. Using a total of 50 data points, the Jacobian entries in equation 7.2 are approximated through a linear data fit as:

$$J = \begin{bmatrix} 0.1 & 0 & -0.92 & 1.1 \\ 1.76 & 2.1 & 0.02 & 0.87 \\ 2.1 & 3.12 & -2.67 & 1.76 \\ 0 & 0.92 & 2.43 & 0.86 \end{bmatrix}. \tag{7.3}$$

Knowledge of the Jacobian allows implementing decoupled robot joint operation for the microrobot using a servoing command input:

$$\begin{bmatrix} \Delta X_D \\ \Delta Y_D \\ \Delta X_C \\ \Delta Y_C \end{bmatrix} = -hJ^{-1}\begin{bmatrix} X_f - X_i \\ Y_f - Y_i \\ \varphi_f - \varphi_i \\ \psi_f - \psi_i \end{bmatrix}, \tag{7.4}$$

where h is a scaling constant, and subscripts ‘i’ and ‘f’ represent the desired initial and final position of the TCP. This command input was used to generate drive input voltages in order to move the microrobot between repeated locations as described in the next section.

6.4.3 Preliminary Precision Evaluation

In order to evaluate its precision, the AFAM is fitted with an Atomic Force Microscope top. Using the derived system Jacobian, the end effector is driven to create a pattern of indentations on a Polymer surface. This setup is shown in figure 6.10. In this case, the pattern created are the letters ARRI. Another example is shown in figure 6.11, which is a 3x3 grid array. The actual indention pattern is compared to the desired one in ordered estimate micro robot accuracy and repeatability.

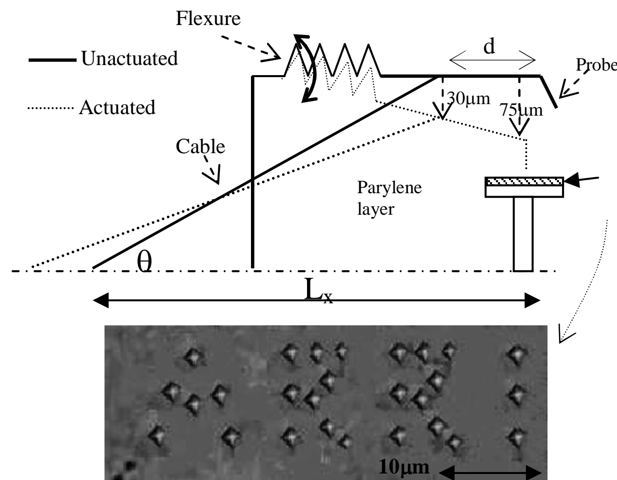

Figure 6.10 Indentations on a 2μm thick Parylene surface.

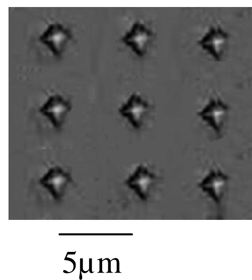

Figure 6.11 A 3x3 Nanoindentation grid for repeatability measurement.

6.4.3.1 Resolution

The positioning resolution of the AFAM is measured using a setup shown in figure 6.12. The setup uses two Keyence Lk-G10 laser displacement sensors. Measurement of prismatic

DOF (X,Y) requires one of the sensors to detect displacement along the corresponding axis and revolute DOF (pitch, yaw) requires the use of both sensors. The sensor resolution is 10nm. The setup in figure 6.12 shows the measurement of pitch resolution.

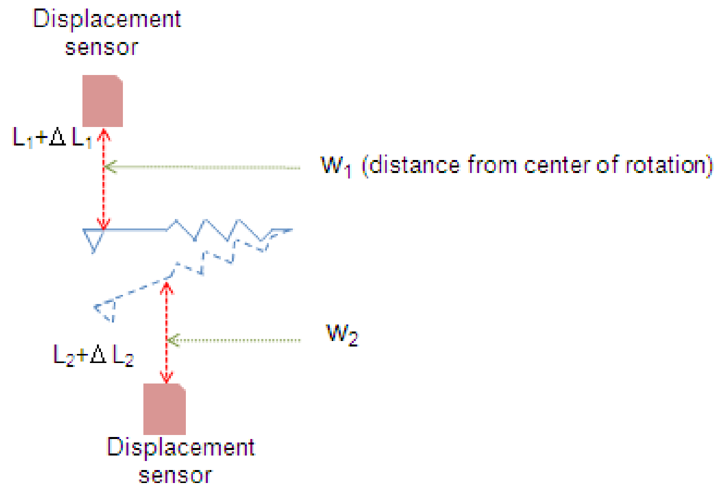

Figure 6.12 Resolution measurement setup.

As shown in the figure, one sensor is placed on top of the cantilever arm and the other below it, in the plane of motion. The pitch angle at any given time is given by

$$\phi = a\tan(\Delta L_2, \frac{\Delta W.\Delta L_2}{\Delta L_1 - \Delta L_2}); \text{where } \Delta W = W_1 - W_2. \tag{7.5}$$

ΔW is the lateral distance of separation between the sensors, ΔL_1, ΔL_2 are the incremental motion detected by the two sensors.

The voltage input to the X_D actuator is incremented between 10~30mV to obtain measurable deflection using this setup. Figure 6.13 shows the resolution variation ay various stages of actuation for all four degrees of freedom. As seen from this figure, the resolution along X and Y axes range between 50~110nm and between 0.02~0.04 degrees along pitch and yaw.

6.4.3.2 Repeatability

The repeatability is measured by repeating indentation patterns on a polymer (Parylene) layer. Figure 6.11 shows a 3x3 nanoindentation grid and figure 6.14 (bottom) shows

the letter R inscribed twice. After completing each instance of the letter, the polymer surface is shifted to make room for the next instance. This is done to allow the robot to start from the same point every time a new letter is inscribed. Repeatability at a specific location is measured by the variance in error in reaching that point. Thus, the repeatability map in XY world coordinates was determined. This is shown in figure 6.14 (top). The measured repeatability indicates a better repeatability in the order of 100nm closer to the origin which is also the zero position of the tip. The repeatability measured ranges between 100~210nm.

6.4.3.3 Accuracy

Accuracy refers to the error between the desired and actual point of indentation reached. In order to measure the accuracy of the AFAM,

- The letters ARRI are indented following a pre-determined order.
- For each indent, the AFM tip is brought back to the same starting point.
- Accuracy along XY (in world coordinates) is measured by averaging the error between desired location to actual location reached.

The difference between accuracy and repeatability in this case is that while accuracy refers to the absolute error between the desired ~ actual points of indentation, the repeatability is a measure of the variance in actual positions reached. The measured accuracy of the AFAM including all points reached is found to be 500nm.

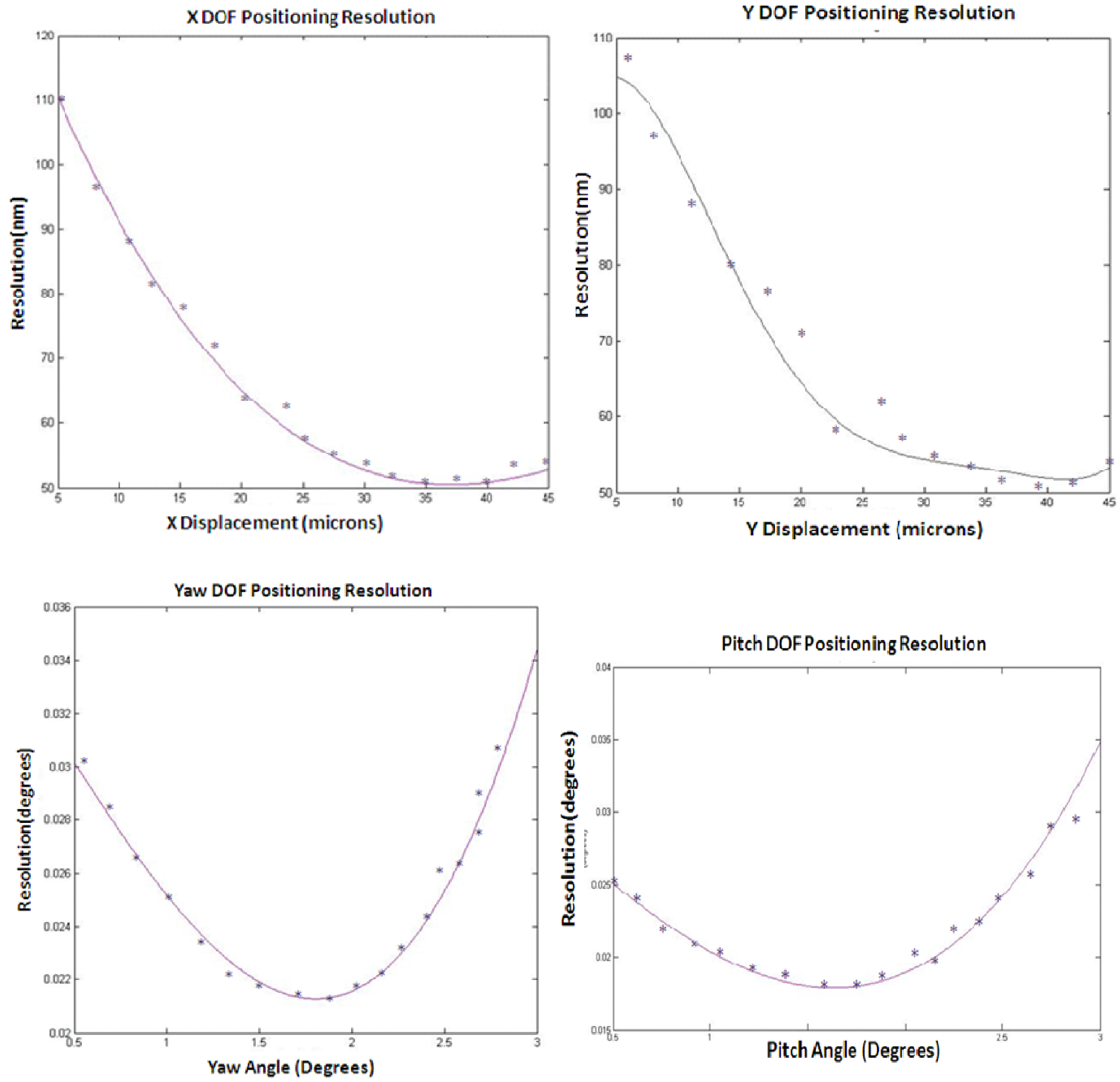

Figure 6.13 Resolution variations along four DOF's.

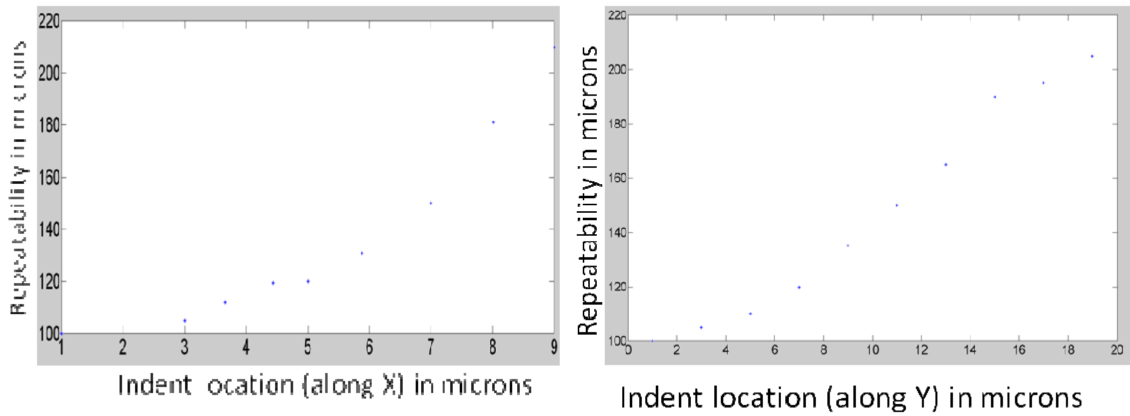

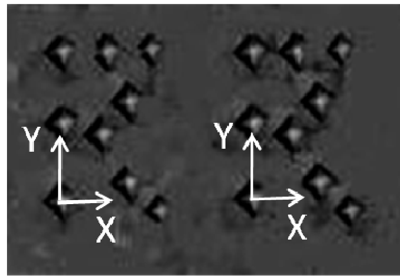

Figure 6.14 Repeatability measurement.

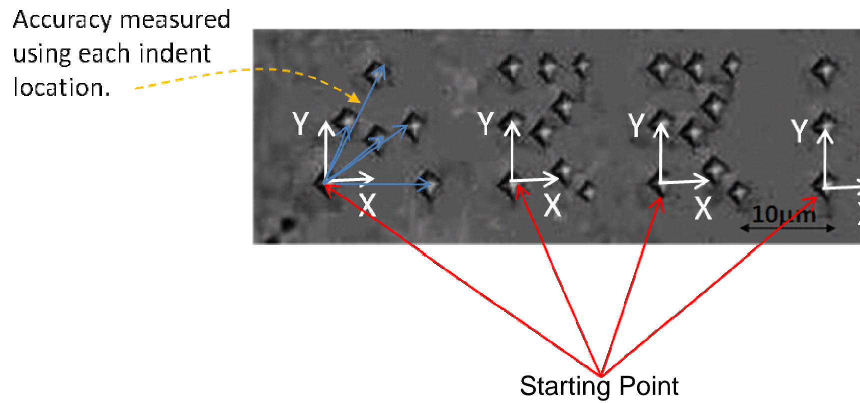

Figure 6.15 Accuracy measurements.

CHAPTER 7

CONCLUSIONS & FUTURE WORK

7.1 Conclusions

The conclusions from the work presented in this dissertation are outlined as follows:

- Bulk micromachined electrothermal actuators provide the best combination of actuation force and strain as required by microrobots for manufacturing applications. However, their application requires resolving high power consumption and heat dissipation challenges.
- Standard lithographic processes combined with micro assembly are a viable technique to manufacture micro robots. The variety of joints obtained using the above stated combination provides sufficient strength and dexterity required for micro and nano positioning applications.
- Assembled micro crawlers (such as the ARRIpede) with single degree of freedom joints are excellent candidates for mobile positioning needs. This conclusion is drawn from the high payload capacity and three degree of freedom stick slip motion exhibited by the ARRIpede micro robot.
- Positioning systems used in conjunction with probing for NEMS can be miniaturized to a few millimeters while still maintaining true 3D work volume and dexterity. This is exemplified using the AFAM micro robot.
- The ARRIpede and AFAM micro robots can be used as unit positioning modules in a nano factory. Multiple such units can be configured to form high throughput and high precision nano manipulation work-cells applied to NEMS manufacturing.

7.2 Future Work

The present work has demonstrated successful streamlining of micro manufacturing processes applied to micro robots, proof of concept for the ARRIpede and AFAM using

simulations and experimental characterization of version 1 prototypes. The results are extended to the cooperative application of these micro robots to configure a nano factory for hybrid nano manufacturing. Future work includes further improvising ARRIpede design and packaging leading to its untethered non holonomic motion control and trajectory planning for nano factory applications. Detailed kinematic and dynamic modeling of the AFAM will be used for improving precision specifications and alternate techniques to achieve out of plane motion transmission will be investigated for higher reliability. The AFAM application capability will be enhanced using a quick change adaptor design for operating a variety of tools.

A Nano factory can be configured for handling typical nanoparts such as nanotubes and nanowires using millimeters robots. A given task such as pushing them can be subject to parallel nanomanipulation using a combination of microrobots, possibly leading to increased throughput. The flow of parts and assemblies between manipulation modules is planned based on the following operating procedures:

- *All nano manipulation modules operate on calibrated open loop mode.* The micro robot Jacobian is used to repeatedly drive the probes through a pre-detetermined trajectory. The elimination of closed loop control decreases cycle time and results in increased throughput. This trajectory varies from between robots belonging to the same module and between different modules. The trajectories are product specific and include the inter play between manipulation and processing. For example, one module could be assigned the task of nanotube bending, which requires fixturing the nanotubes using probes and impinging a suitable gas (such as Oxygen) at the specific bend location. The operation of the nanomanipulation module is modeled as a stochastic process.
- Scanning modules which consist of high resolution scanning using SPM or imaging using SEM, monitor the state of the nano parts/assemblies before transfer between consecutive modules. Thus, the factory is housed within the SPM/SEM station. Due to the fact that the

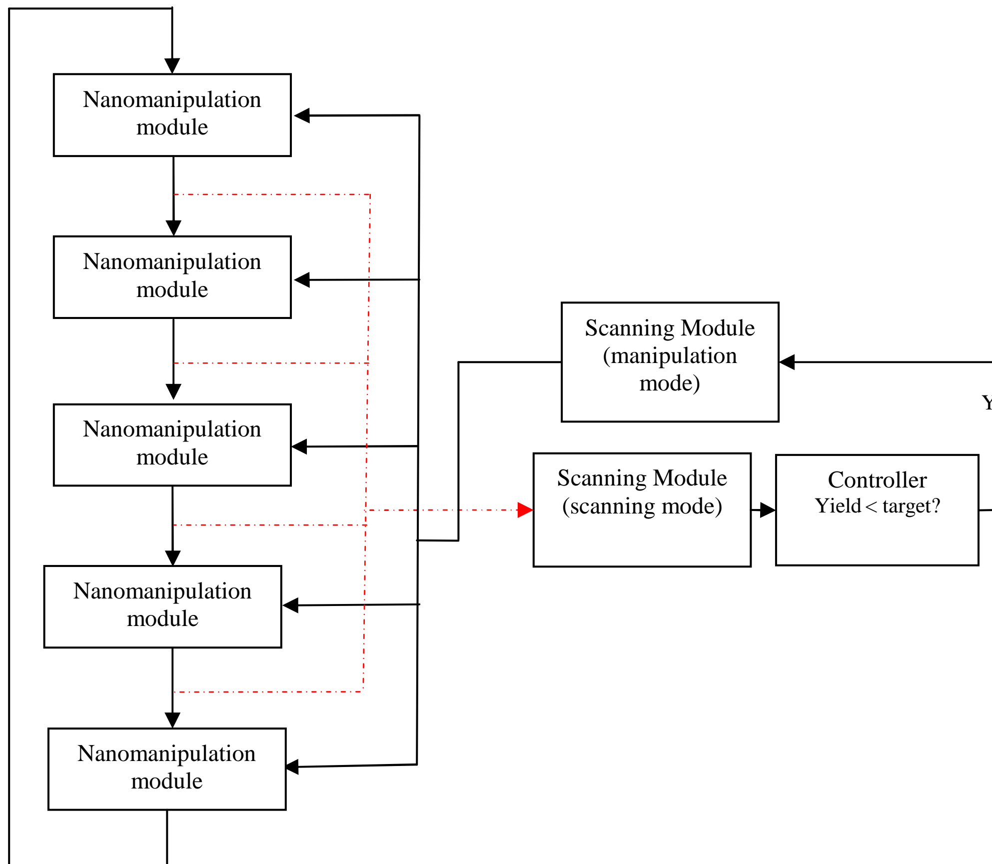

Figure 7.1 Controller for hybrid nano assembly.

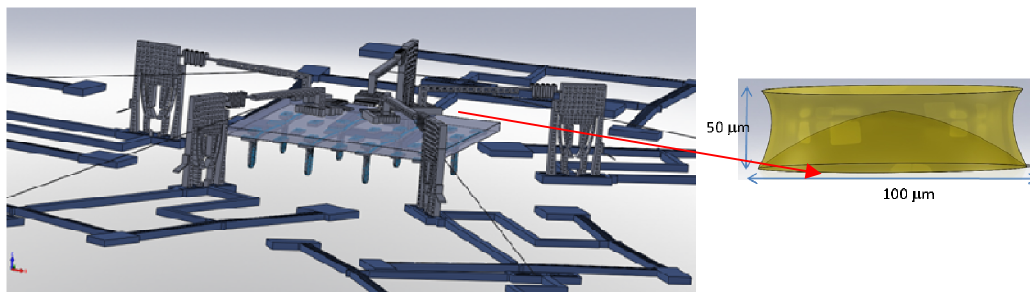

Figure 7.2 Work Volume of Nano Manipulation Workcell.

nano manipulation modules are not actively controlled, the scanning task also gives information on the yield of the preceding process.

- The availability of closed loop manipulation using the scanning module is employed as a secondary manipulation process if necessary. However, it is only when the high cycle time and low throughput resulting due to the closed loop serial operation is acceptable. A hybrid controller is used to execute this operating procedure and is outlined in figure 7.1.

The nano manipulation workcell can be configured multiple AFAM's as shown in figure 7.2. The specifications of the workcell are listed as follows:

- Total volume occupied:6mm$^{3.}$
- Number of micro robots: 6 (5 AFAM +1 ARRIpede).
- Degrees of freedom: 23 (20+3).
- Accuracy: ~200nm.
- Repeatability: ~100nm.
- Resolution: ~50nm.
- Force output: 100~150mN along XYZ axes.
- Work volume shown in figure59.

The ARRIpede can carry and support a minimum of 9g payload into this working envelope using 3dof crawling. Its design is optimized for stick slip motion on Si wafers and can carry the self assembly module consisting of Au colloidal particles, CNT, Si Nano-wires etc. The AFAM's carry individual probes or probe arrays for top down assembly.

APPENDIX A

SOI MEMS FABRICATION RECIPE

Details describing the fabrication procedure outlined in chapter 4 are presented in this appendix. This procedure relates to the use of fabrication equipment at ARRI's HPML and Stanford Nanofabrication facility. The fabrication procedure outlined here can be used to create high aspect ratio released and tethered MEMS components on 4 inch Silicon on Insulator (SOI) wafers. Both, device and handle sides of the wafer are subjected to Deep Reactive Ion Etching and wet etch as described. Released MEMS structures can be coated with metal using a shadow mask based deposition technique. The fabrication of the shadow mask is also outlined here.

A.1 Fabrication on the Device Side

- Using Headway or SVG-coat, coat 3microns PR without EB removal and pre-bake at 90deg C .for 200 seconds.
- The wafers need to be primed in YES oven prior to the above step.
- EV align -exposure time=3.2 seconds:
  a. Soft contact.
  b. Crome down.
  c. Roughly align wafer flat to bottom side of mask.
- Develop in SVG dev -do not post bake here.
- Immediate post bake in 110 deg oven for 30~45 minutes. ·
- Shift wafer to STSetch2 (used DEEP rcp on STSetch for 55mins this particular run):
  a. Vent system.
  b. Load wafer.
  c. Pump.
  d. Map wafers.
  e. Choose "Rakesh SOI" under recipe tab and select time to 32 minutes.
  f. Verify completed etch under microscope (sometimes also shows color change). ·
- Remove PR at Gasonics:

a. Make sure wafer flats are aligned to top/bottom of cassette.

b. Place wafer on bottom slot. ·

- Release in WBgen / Wbsilicide:

  a. 49% HF for 20 mins.

  b. DI water for 30 mins. ·

- Release in Wbsolv,

  a. IPA for 1hour (minimum

- Critical Point Drying:

  a. Keep wafer in IPA until CPD starts.

  b. Make sure sufficient LCO2 levels are maintained.

  c. Clean all containers used in CPD with IPA-wafer may get contaminated.

  d. Purge time =10 minutes. ·

A.2 Fabrication on the Handle Side

- Back Side Lithography:

  a. Remove PR using acetone.

  b. YES oven. c. Coat 10 micron PR with 120sec bake at 90deg.

  c. EV align-back side:

    - Choose back side recipe in EV align.
    - Choose cross hair for over-laying alignment marks (important).
    - Select soft-contact mode.
    - Intermittent exposure for 12 sec (6sec exp +15 sec wait + 6 sec exp).
    - Make sure to have layout pictures to aid alignment.
    - Make sure to have aligned wafer flat to bottom of mask during front side exposure.

- Develop for two minutes (LDD27W). ·
- Post bake at 110deg C for 60 mins (45 minutes min).

- Prepare a support wafer (350+ micron thick).

  a. YES oven.

  b. Coat 3micron PR without edge bead removal (imp). Do not bake at this time.

  - Place wafer (no PR on device side) on top of this and align flats as precisely as possible (mismatch will result in wafers not fitting into the fixture in STS).
  - Place wafers on hot plate at 105 deg C and using tweezers even out the gap between the wafers (careful not to tough pattern and too much pressure may break the SOI.

  c. Bake for 1 hour. ·

- Back Side Etch:

  a. Stsetch2 does not accept front side etched wafers for back side DRIE (conflicts underside cooling of wafer).

  b. Try using a handle wafer with the SOI wafer bonded using PR to ensure proper bond. The sandwiched wafers have to be heated on a hot plate while applying pressure with weight. This may result in compressing the PR layer on backside.

  c. The reduced PR burns up before the 400 microns thick silicon can be completely etched. ·

- Remove PR at gasonics:

  a. Place wafer on bottom slot.

- Release in WBgen / Wbsilicide:

  a. 49% HF for 20mins.

  b. DI water for 30 mins.

- Release in Wbsolv wet bench:

  a. IPA for 1hour (minimum). ·

- Critical Point Drying:

  a. Keep wafer in IPA until CPD starts.

  b. Make sure sufficient LCO2 levels are maintained.

  c. Clean all containers used in CPD with IPA-wafer may get contaminated.

  d. Purge time =10 minutes.

A.3 Shadow Mask Fabrication

The following procedure outlines fabrication of shadow masks used to deposit metal layers on released MEMS structures.

- Start with two 400 micron thick wafers.
- Heat at 150 deg C for 30 mins
- On one of them, coat 1.6 micron PR with 2mm EB removal (no prebake required).
- Sandwich the two wafers using the caoted layer of PR and align them to match the wafer flats. (as accurately as possible).
- Place the wafers on a hot plate kept at 105 deg C. Cover them with foil and place a weight over them. 6) Bake for 1 hour.
- This is followed by 10 micron PR (YES oven+bake at 90deg C for 200sec) on the wafer sandwich and EV align exposure for 12 sec followed by develop.
- Post bake at 110 deg C for 30 minutes.
- 9) Etch at STSetch 2 for 70 minutes-check under microscope for progress (use RAKESH SOI recipe on tool).
- Etch rate is approximately 4.5 microns/min completion under microscope.
- Continue etching at 5~10 minute intervals.
- Place the wafers in acetone in Wbsolv inside the litho area.
- After all the PR is removed, the shadow mask is ready.

APPENDIX B

M^3 CONFIGURATION

The automated MEMS packaging system described in chapter 4 can be reconfigured to suit various various packaging needs. Described in this appendix, are the configuration and hardware details of the setup. A DRIE based MOEMS die (figure 2) has to be aligned to and placed within a Kovar carrier (figiure1) within a specified tolerance budget (table B.1) to accomplish “die-attach operation”. The attachment is to be accomplished by heating a preform between the die and the carrier.

B.1 Part Description

The following parts need to be precision picked and placed:

B.1.1 KOVAR® carrier:

The carrier is made of KOVAR which is an alloy of Fe, Co and Ni. It is about an inch by an inch in area and comprises of a cavity to house the MEMS die and feedthrough holes on the side walls through which we pass optical fiber into the MEMS die.

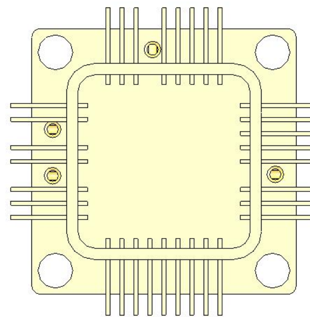

Figure B.1 Kovar Carrier (top view).

1) Sn-Au perform: Solders MEMS die to carrier. It is 12mm X 12 mm in area and 100 microns thick.

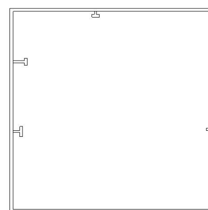

Trenches on die
(4X)

Figure B.2 Sn-Au Preform.

2) DRIE MEMS die: This MOEMS die has four trenches which are 150 microns wide and deep. These trenches need to be aligned to their corresponding fiber feedthrough holes on the carrier when the die is placed into the carrier.

B.2 Tolerance Budget

Table B.1 shows the permitted tolerance budget during the die-attach assembly operation. This refers to the tolerance between the MEMS die and the package carrier.

Table B.1 Tolerance Budget for Die Attach

Die to Package assembly tolerance in microns and degrees	ΔX (μm)	ΔY(μm)	ΔZ(μm)	Δθ(deg)
	50	50	25	0.5

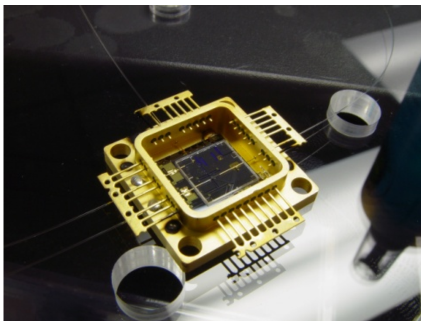

Completed package

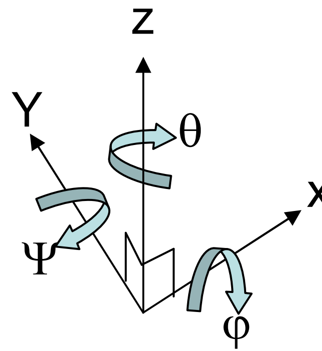

Reference Coordinates

Figure B.3: Completed Package

B.3 System components

The M3 system comprises of multiple high precision positioning robots, end effectors and fixtures which function across the meso and micro scales. These are described in this section.

B.3.1 Robots

M3 consists of four high precision robots that function within a single automation framework. Motoman RobotWorld ® is used as the work-cell. This houses the various robots, end effectors, vision systems, parts and process enabling equipment such as the Laser. The robots that function within M3 framework are:

(a) RM 6210 coarse positioning system. This is a 4 axis-XYZθ robot (figure3). The robot is open-loop and has a rated accuracy of 50 microns and a resolution of 2.5 microns along

XY. The Z and Theta axes have rated resolutions of 5 microns and 0.006 deg respectively. This robot is used to perform most pick and place operations in the M3 setup

Figure B.4 Four Axis Robot.

(b) TM 6200 GT fine positioning system. This is a 2 axis -XY robot (figure 4). The robot is closed loop and has a rated accuracy of 25 microns and resolution of 0.5 microns. This robot is used in conjunction with the vision system in the M3 setup.

Figure B.5 Two axis Robot.

(c) CM 6200 coarse positioning system. This is a 2 axis-XY robot (figure 78). The robot is open loop and is rated similar to the RM6210.

Figure B.6 Two axis robot

(d) Four Axis XYZθ fine positioner. The Thorlabs PT1Z3 (XYZ) and CR1-Z6 (Theta) are combined to form a 4 fours axis fine positioning robot (XYZθ).

B.3.2. Other Off-the-shelf hardware

(i) Edmund Optics VZM450 CCD microscope is mounted on the TM 6200 robot.

(ii)The 4 axis robot uses the XC-1 quick change adaptor from Advanced Robotics

(iii)Table B.2 shows the pneumatic accessories used with the M3 setup

Table B.2 Pneumatic Hardware.

Part	Manufacturer
Nylon Tubing (4mm gauge)	SMC corp
M3 fittings for 4mm tubing	SMC corp
Vacuum Nozzles	Virtual ii
Actuator for carrier pickup (RPLC-1M)	Robohand Inc
Solenoid for RPLC-1M actuator	SMC corp

B.3.3 End Effectors for Pick & Place

The following tools have been designed to be used in conjunction with the above mentioned hardware to accomplish the die-attach operation sequence.

(i)Carrier pick & place tool : This end effector (figure 6.0) uses the pneumatic RPLC actuator to open and close a pair of jaws that pick the Kovar carrier.

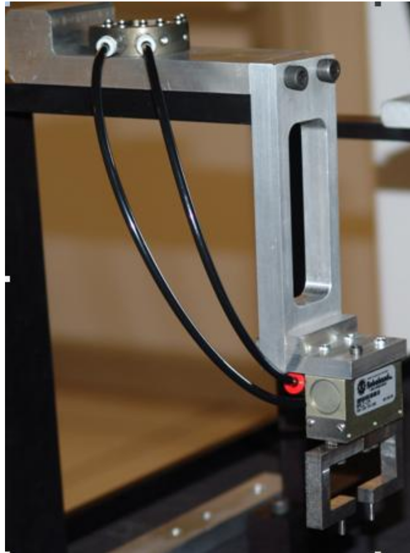

Figure B.7 Carrier Gripper.

(ii)Die pick-up tool: This end effector (figure 7.0) incorporates a 90 degree vacuum tip fixtured on an Optosigma ® tilt stage. This tool is used to pick and place the preform and the die.

Figure B.8 Die Pickup Tool.

B.4 Frequency Analysis

The design of these end effectors has been optimized for mass and modes of natural frequency vibration using FEA analysis. Using Ansys®, the end effectors designs have been optimized for low mass v/s higher natural frequency. The following table (Table B.3) illustrates the results.

Table B.3 End Effector Design

Type		Weight/ dimensions	Harmonics
1 (Version 1)		0.45 kgs plate thickness = 0.5 inches	1st=210.58 hz 2nd=272.64hz 3rd=957.69hz 4th=1106.62hz
2 (Design modified by changing thickness of plates)		0.285 kgs plate thickness =0.25 inches	1st=120.4 hz 2nd=190.76hz 3rd=351.67hz 4th=872.23hz
3 (Design modified by changing thickness of plates and reinforcing)		0.34 kgs plate thickness =0.25 inches	1st=242.58 hz 2nd=293.4hz 3rd=1058.75hz 4th=1271.76hz

The third design is chosen for the design as it shows higher level of harmonics for reduced mass as compared to the version1 design.

B.5 Platen Configuration

The default Robotworld platen size in the puck.ocx file is not accurate to the actual size of the platen.

a) The following is the procedure followed to establish the size of the platen and thus fix accurate homing positions for the robots Align the fine positioning vision robot to the

origin of the Robotworld® coordinate frame. Adjust the harbors at that corner of the platen such that they are both aligned to the robot (lights come ON).

b) Move the fine positioning vision robot away from that corner and place the next robot (four axis) in that corner without disturbing the harbor settings.

c) Initialize that robot and actuate it along X & Y to move it from the origin to the corner which is the desired homing position.

d) Note the home position of the robot when it reaches one of the corners. If this the corner opposite to the origin, then the extreme position reached gives us the platen size.

e) Align the harbors of the remaining corners in a similar manner.

Using this procedure the ACTUAL platen size is determined as *1166.04 X 790.125 mm* as opposed to 1400 X 800 which is the default value.

B.6 Die Attach Sequence

In order to accomplish the die attach operation, the sequence illustrated in the following page is adopted. For this purpose, the robots used are the four axis (called coarse1) robot and the two axis closed loop (called fine1) robot. The coarse 1 performs all of the pick and place operations. Via the quick change device, this robot switches between the carrier gripper tool and the die pick up tool. The fine 1 robot is used to facilitate vision. The VZM microscope is mounted on this robot.

Fine Positioning vision robot:

X=0.000 mm

Y=0.000 mm

Coarse Positioning four axis robot

X= 1166.040 mm

Y= 790.125 mm

As shown in the sequence block diagram, some of the operations are hard coded into the program that runs the die attach sequence. These locations are provided here:

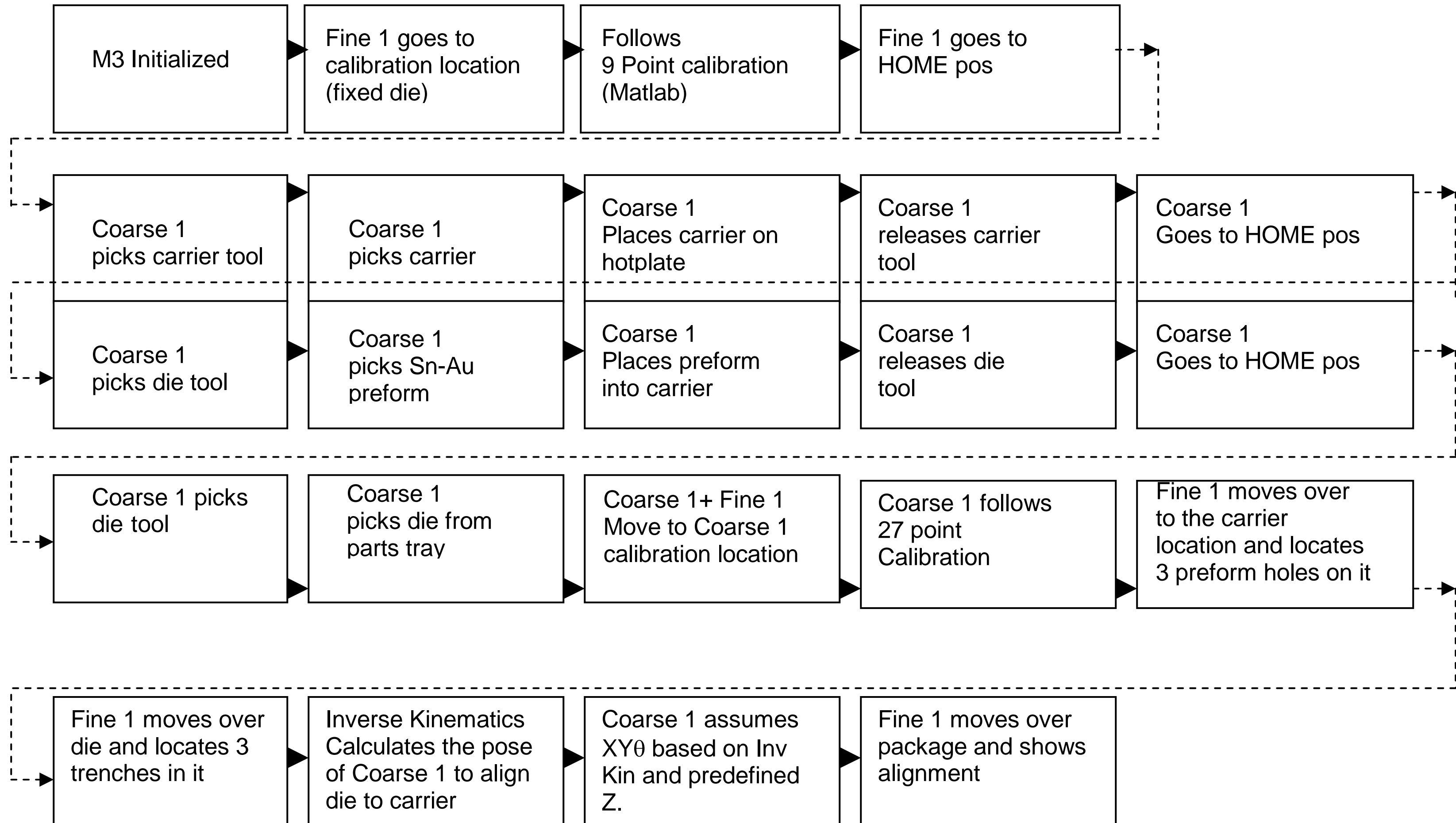

Figure B.9 M3 setup- Die Attach Sequence.

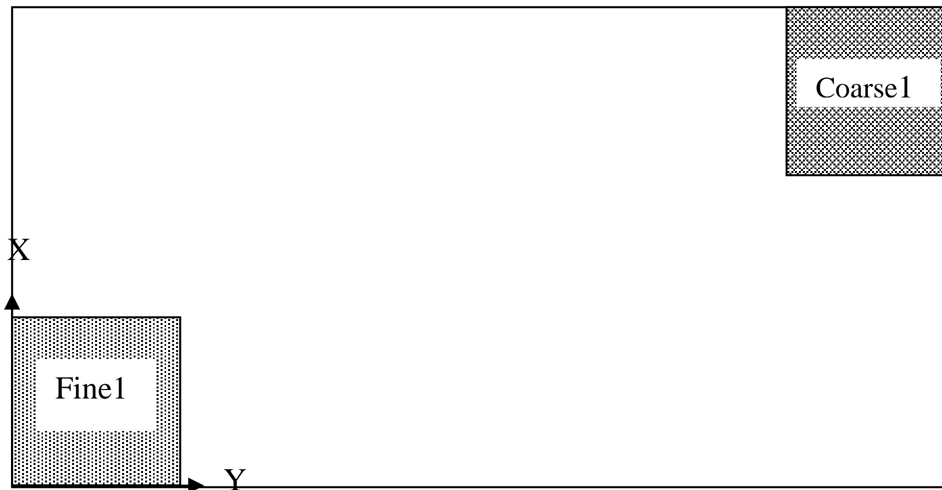

Figure B.10 Robot Home Positions

On Tool Rest

1) Location to align four axis robot with quick change on carrier pick up tool

   X = 1072 mm

   Y = 582.131mm

   Z = 57.8 mm

   θ = -4.654 degrees

2) Location to align four axis robot with quick change on die pick up tool

   X=1003.537mm

   Y=416.125 mm

   Z=10.75mm

   θ=179.658 degrees

On Parts Tray:

1) Location to pick carrier from parts tray

   X = 353 mm

   Y = 368 mm

   Z = 84 mm

   θ = -45 degrees

2) Location to pick perform from parts tray

X = 412.017 mm

Y = 506.125 mm

Z = 40.8 mm

θ = 180 degrees

3) Location to pick die from parts tray

X = 410 mm

Y = 558 mm

Z = 41.15 mm

θ = 180 degrees

4) Carrier Place Location

X = 545 mm

Y = 494 mm

Z = 83 mm

θ = -45 degrees

5) Preform Place Location

X = 593.75 mm

Y = 571.5 mm

Z = 40 mm

θ = 180 degrees

B.7 Camera (Fine1) Calibration

The following operating conditions were followed:

- Zoom: 3X
- Location of the fixed die used for calibration: X= 492.6, Y=172.9
- Total change in X during calibration = 0.3 mm
- Total change in Y during calibration = 0.4 mm

The following are the 9-points that are used to calibrate the vision system.

Table B.4 Camera Calibration Data

Sl No	Xc (mm)	Yc (mm)	PixelX	PixelY
1	488	171.75	164.113	148.75
2	488.15	171.75	335.859	132.023
3	488.3	171.75	489.074	114.841
4	488.3	171.9	505.15	241.078
5	488.15	171.9	351.173	258.02
6	488	171.9	177.801	274.855
7	488	172.05	184.124	391.901
8	488.15	172.05	357.148	394.852
9	488.3	172.05	511.863	357.173

The following is the transformation matrix that is derived for the calibration:

$$R = \begin{bmatrix} 0.000906036 & 0.0000867837 \\ -0.00012655 & -0.00121902 \end{bmatrix} \quad \text{(B.1)}$$

B.8 Robot Calibration

The 27 point calibration is used with the four axis robot + die pick-up tool combination.

Table B.5 Robot Calibration Data

Xo-mm	Yo-mm	theta-deg	Px	Py
750.2	559.95	179.93	202.431	350.462
750.2	560.1	179.93	197.3	291.282
750.2	560.25	179.93	190.65	234.365
750.4	559.95	179.93	291.459	336.397
750.4	560.1	179.93	287.265	281.586
750.4	560.25	179.93	281.335	226.673
750.6	559.95	179.93	369.556	330.4
750.6	560.1	179.93	364.388	274.627
750.6	560.25	179.93	358.426	220.565
750.2	559.95	179.86	195.331	290.467
750.2	560.1	179.86	189.454	235.4
750.2	560.25	179.86	184.219	179.583
750.4	559.95	179.86	282.614	284.425
750.4	560.1	179.86	278.381	230.447

The Matlab script to perform inverse kinematics and visual servoing calculations has been interfaced with Labview to run with the rest of the sequence (Figures 101 and 102 show the VI example).

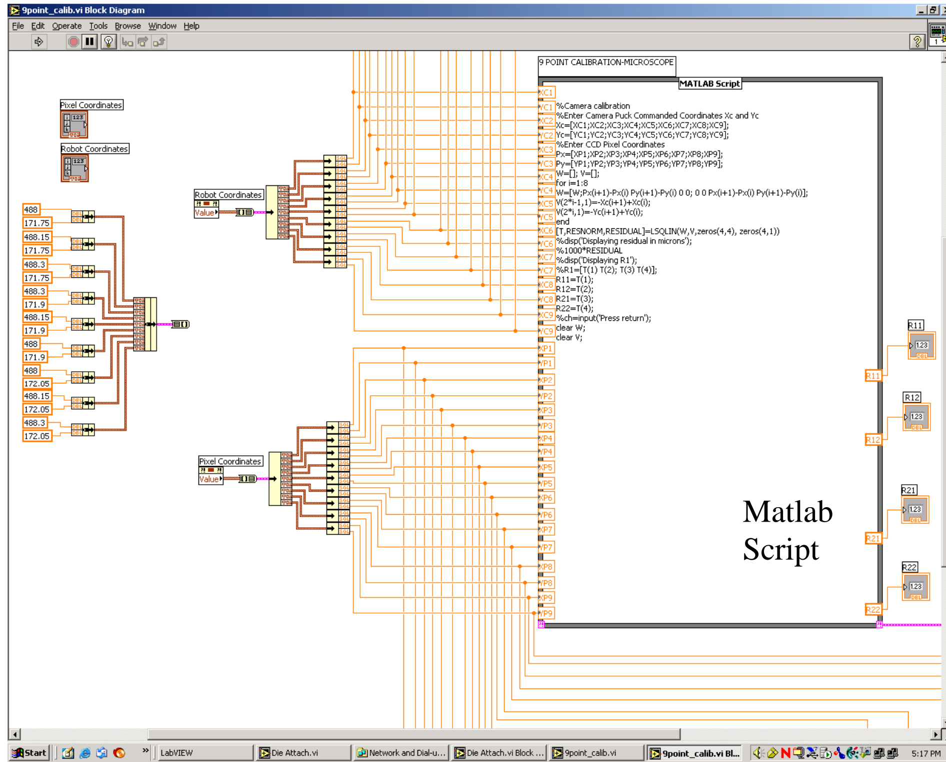

Figure B11 Visual Servoing VI.

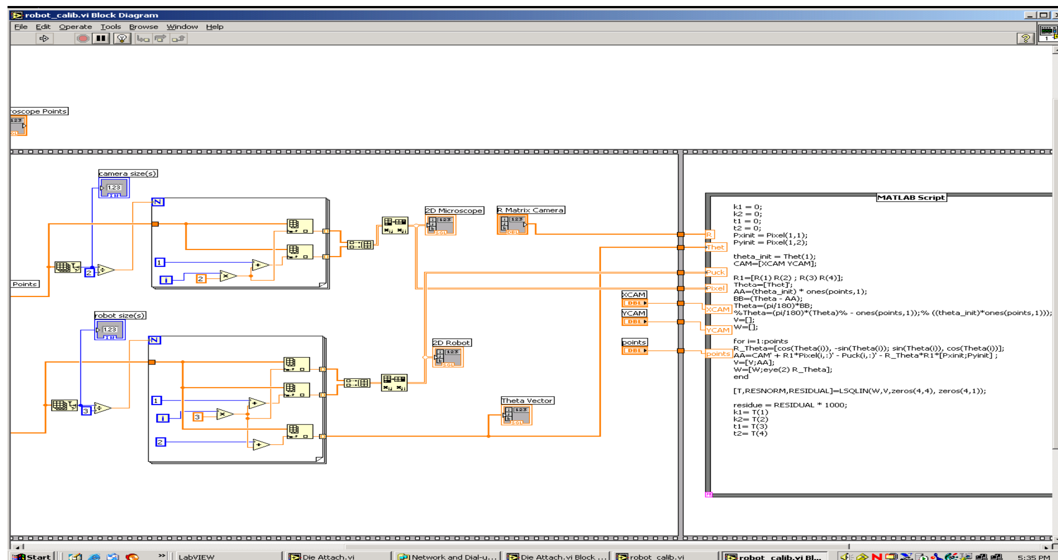

Figure B12 Inverse Kinematics VI.

APPENDIX C

DESIGN LAYOUTS

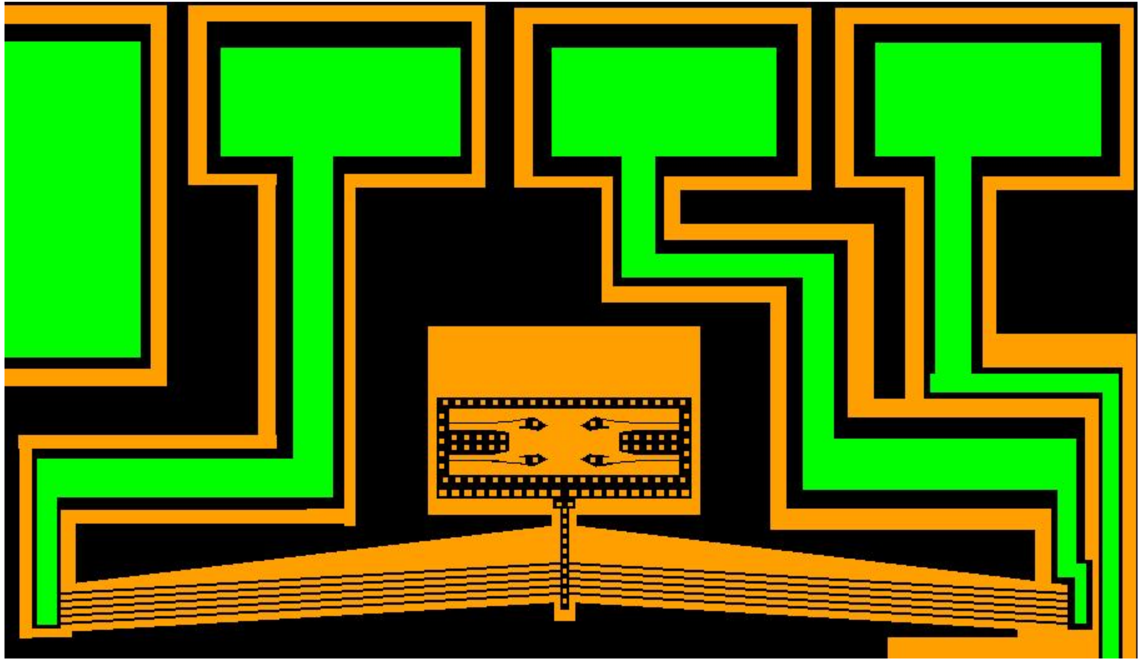

Figure C.1 ARRIpede Actuator Type1

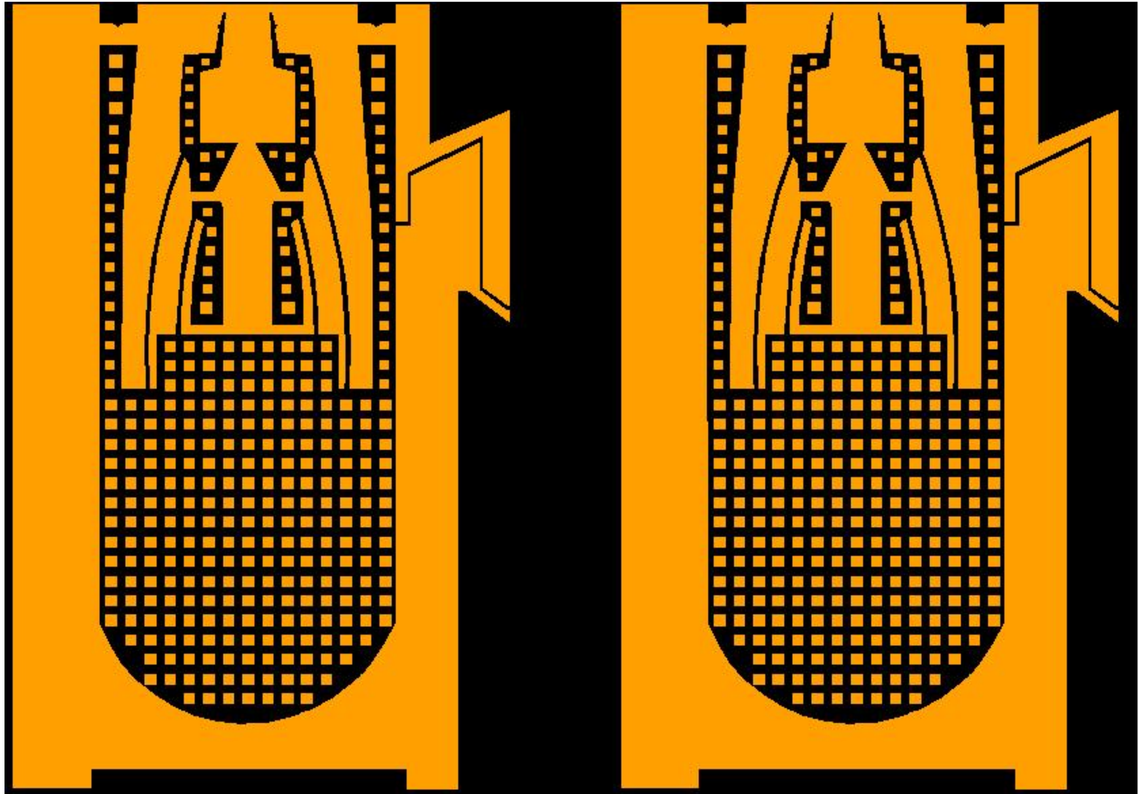

Figure C.2 ARRIpede Leg

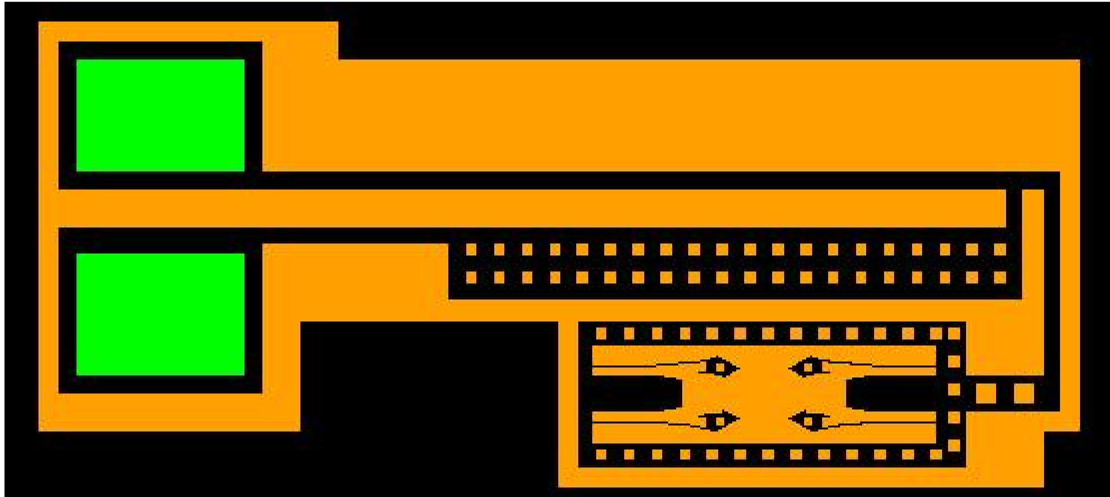

Figure C.3 ARRIpede Actuator Type2

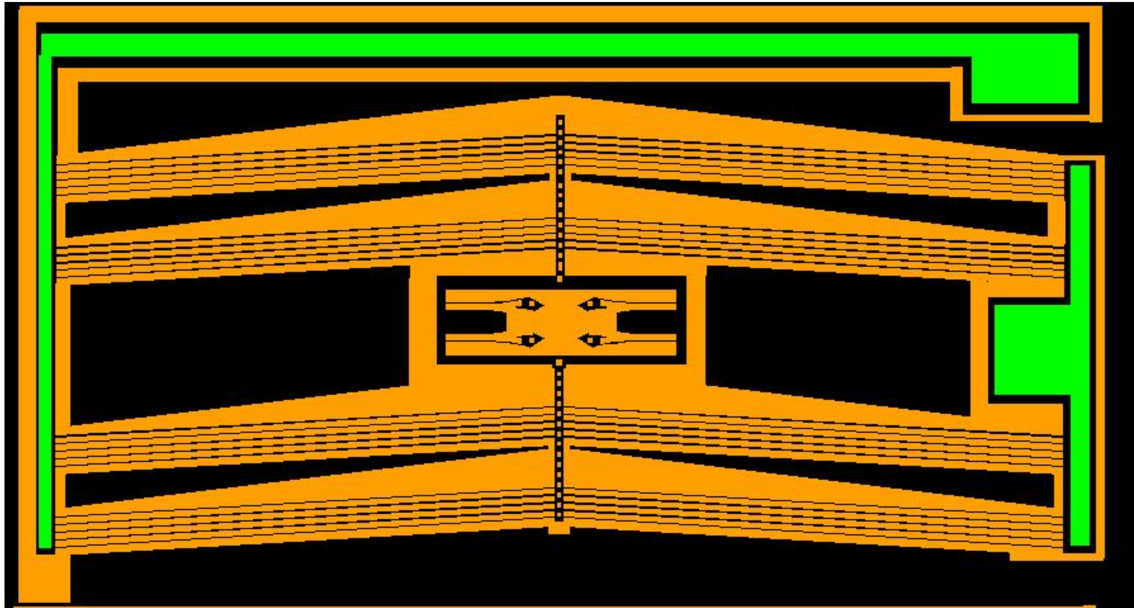

Figure C.4 ARRIpede Actuator Type3

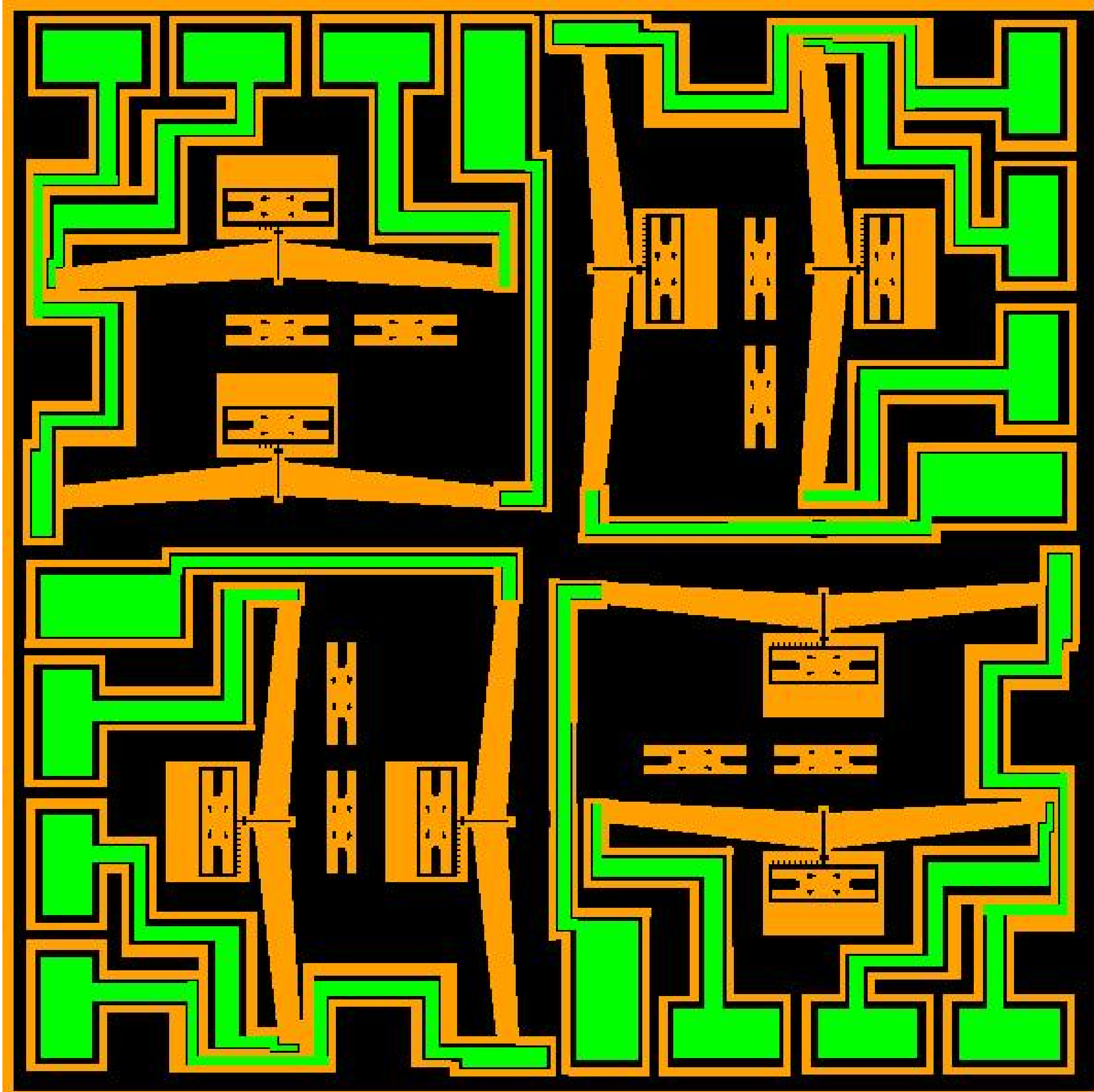

Figure C.5 ARRIpede Belly Type1

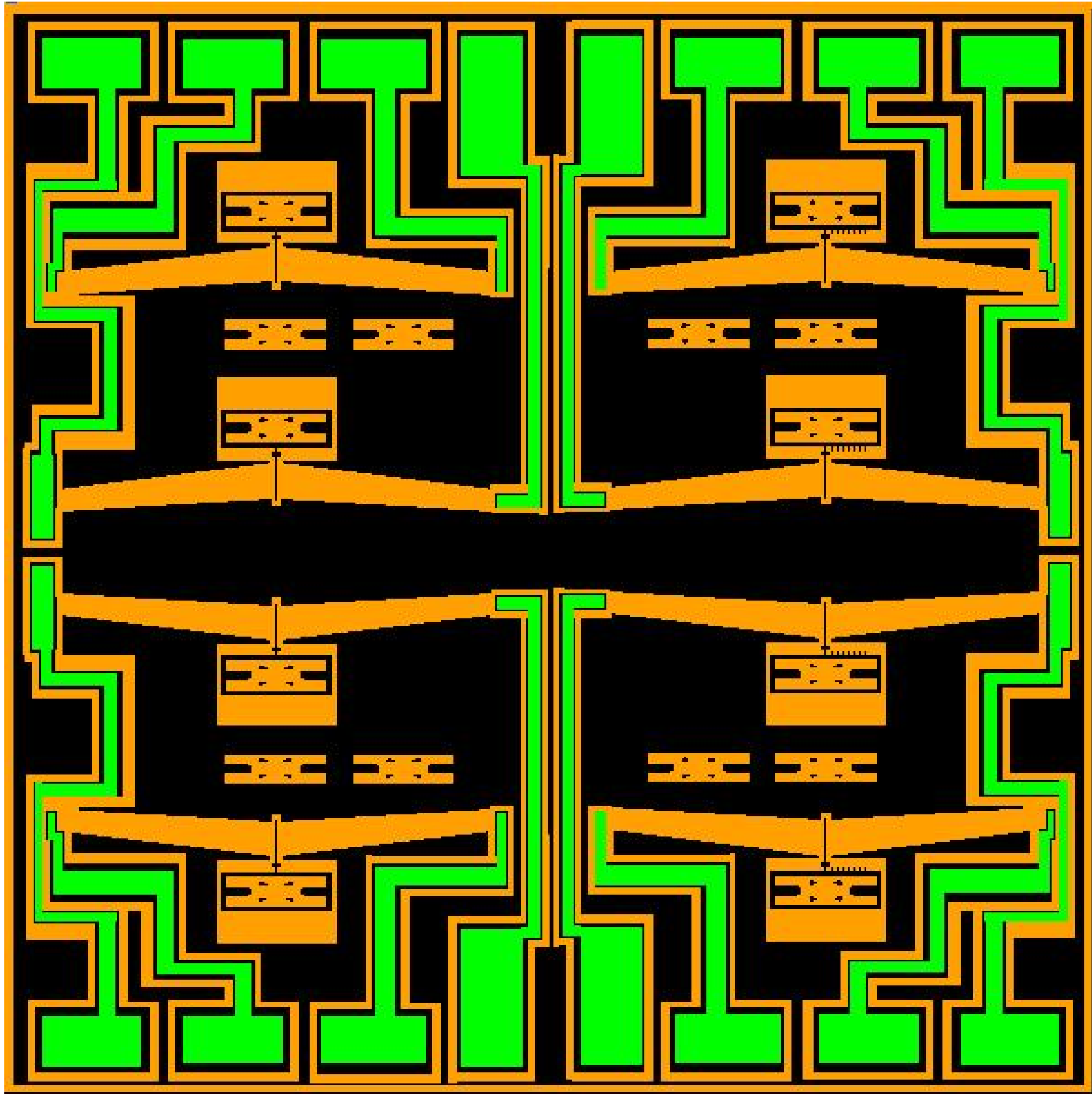

Figure C.6 ARRIpede Belly Type 2

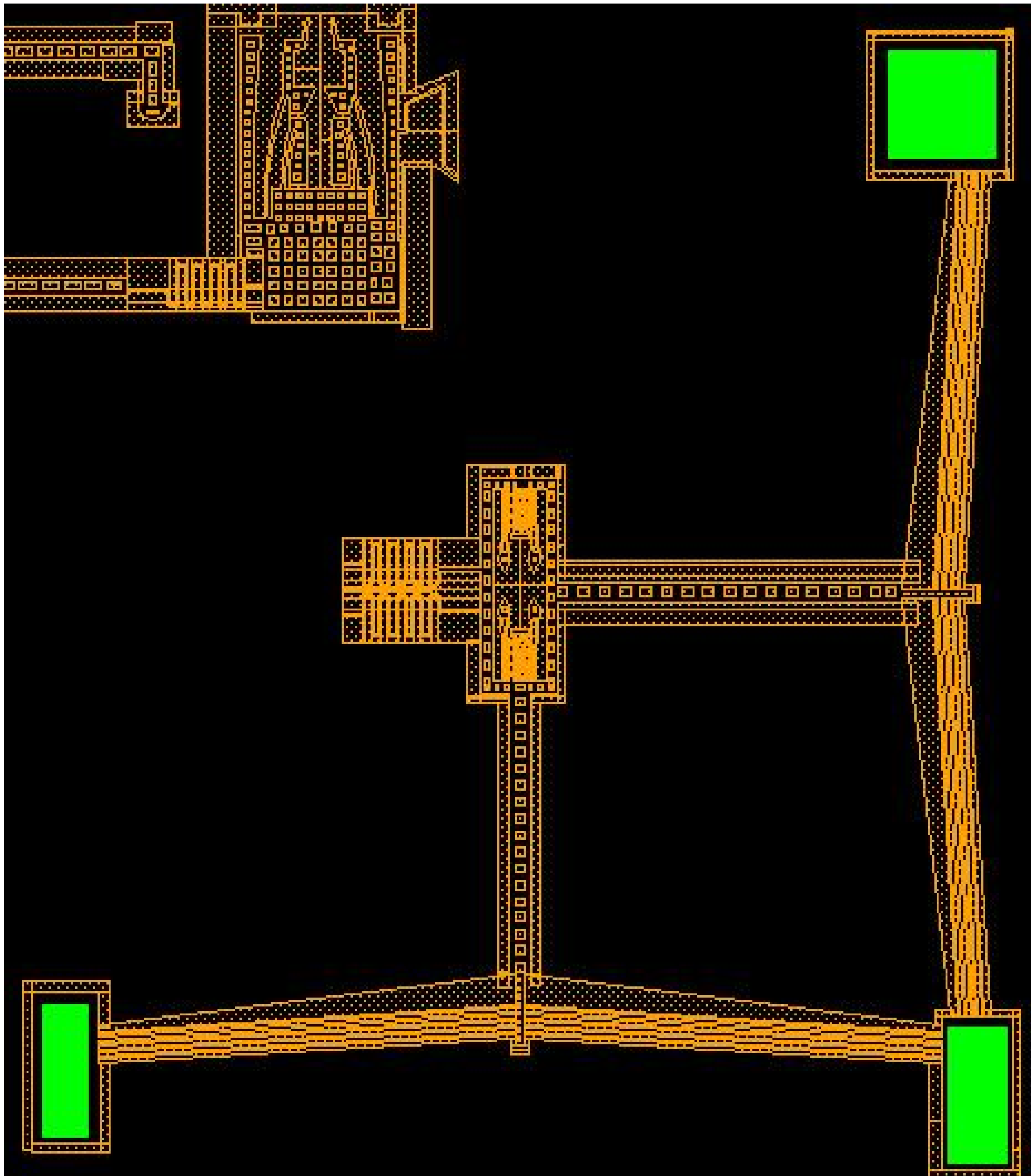

Figure C.7 XY Stage type1

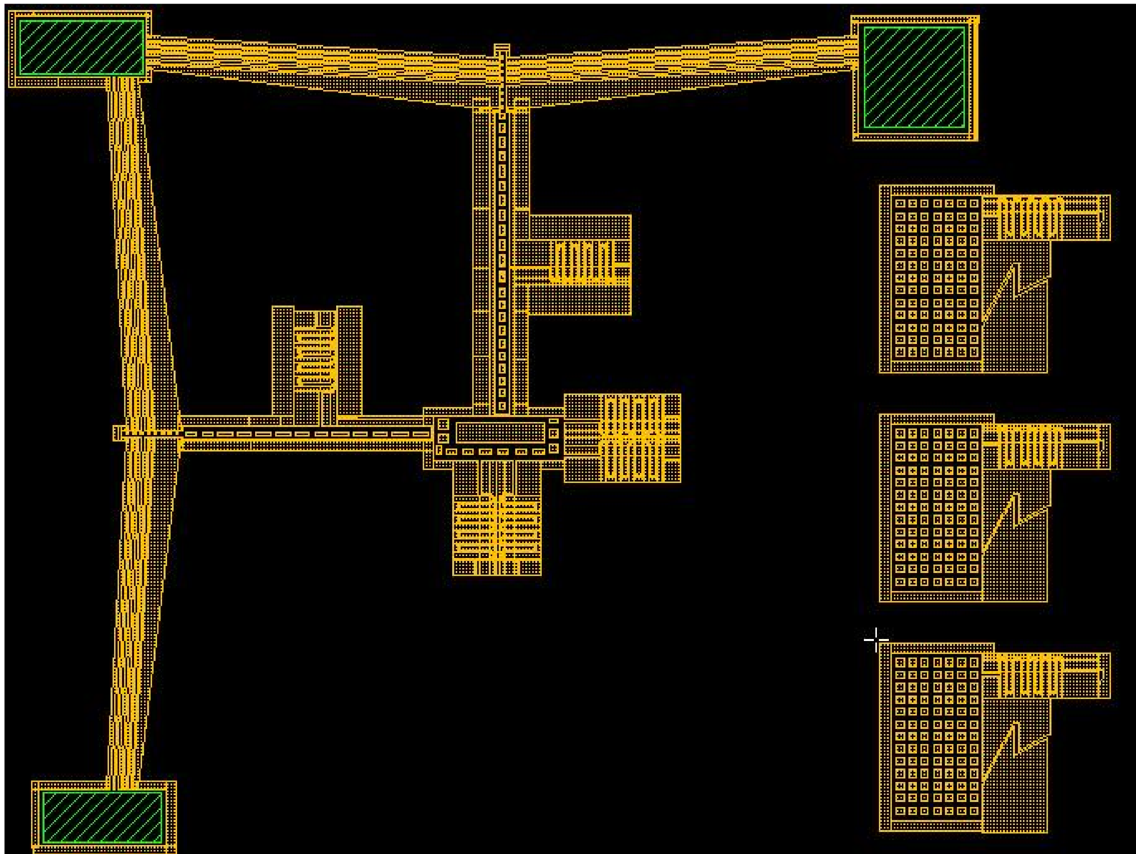

Figure C.8 XY Stage type2

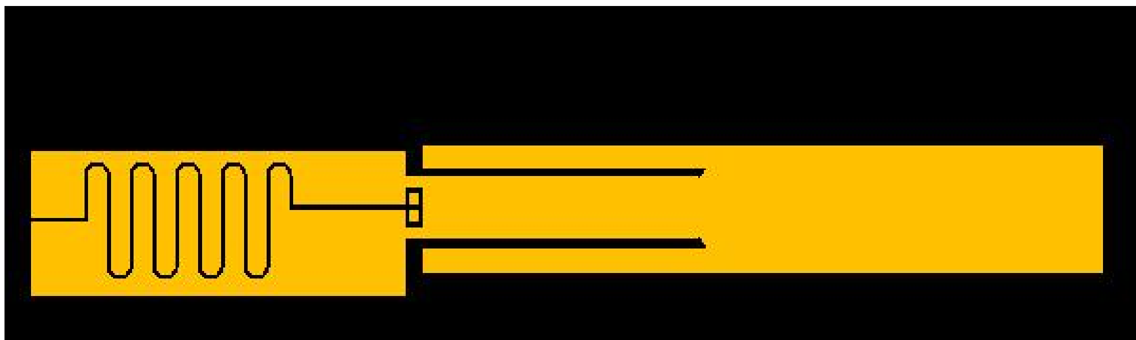

Figure C.9 Microsnapfastener type 1

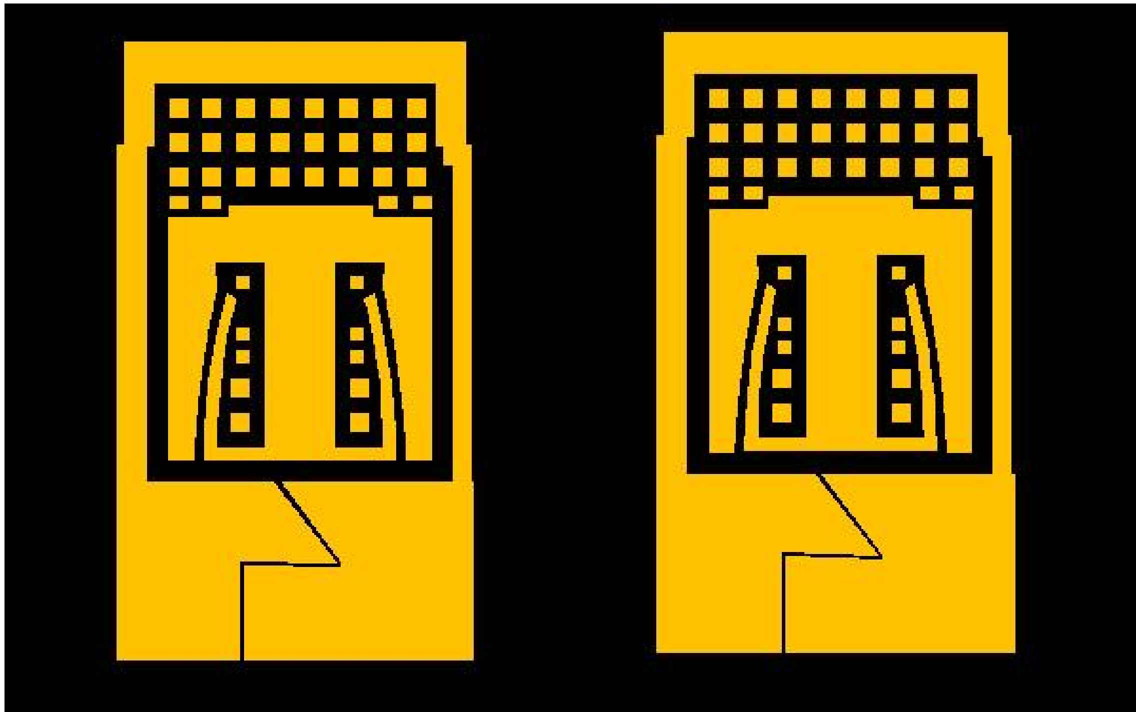

Figure C.10 Part corresponding to figure C.9

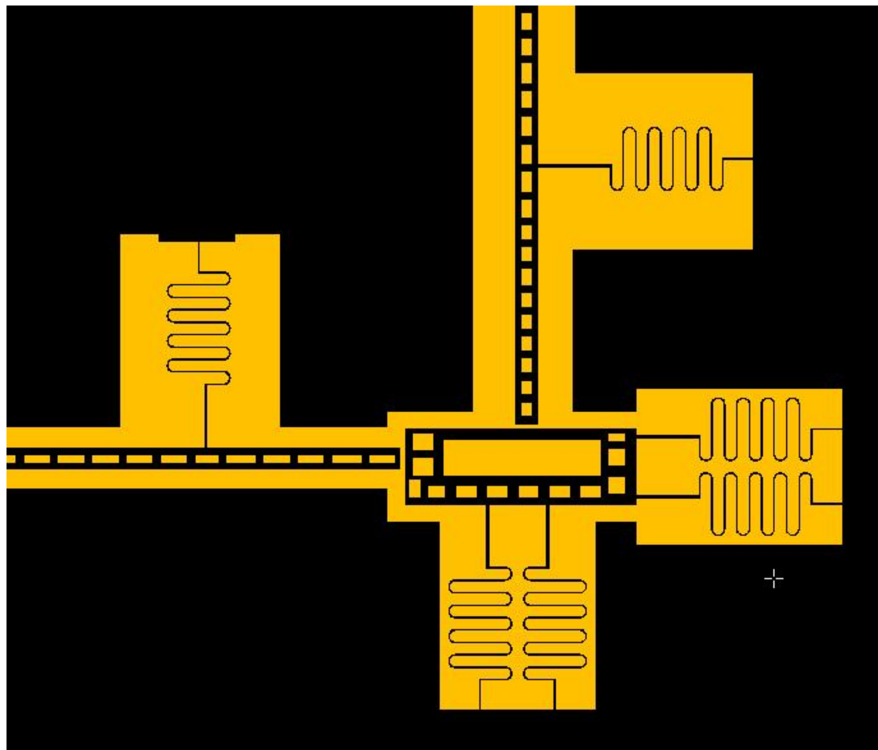

C.11 Single DOF flexures

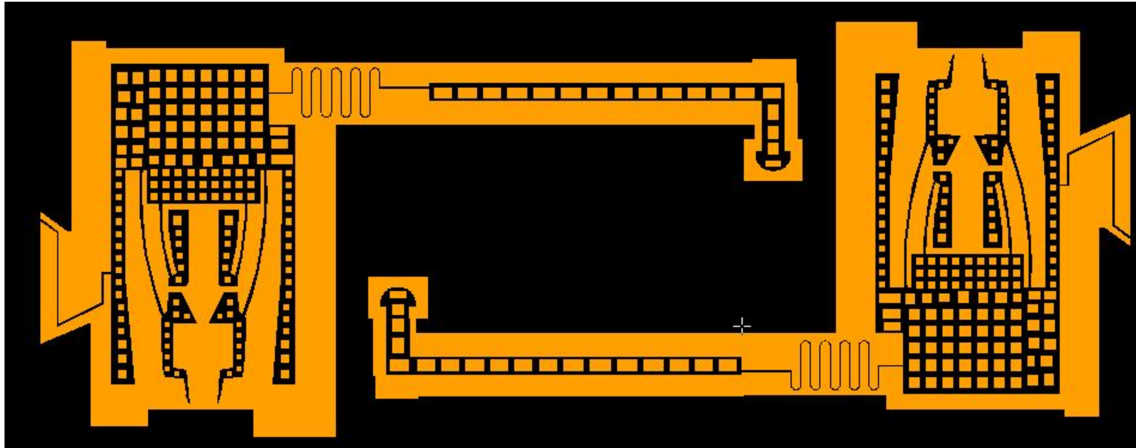

C.12 Z Axis Arm for the AFAM version 1

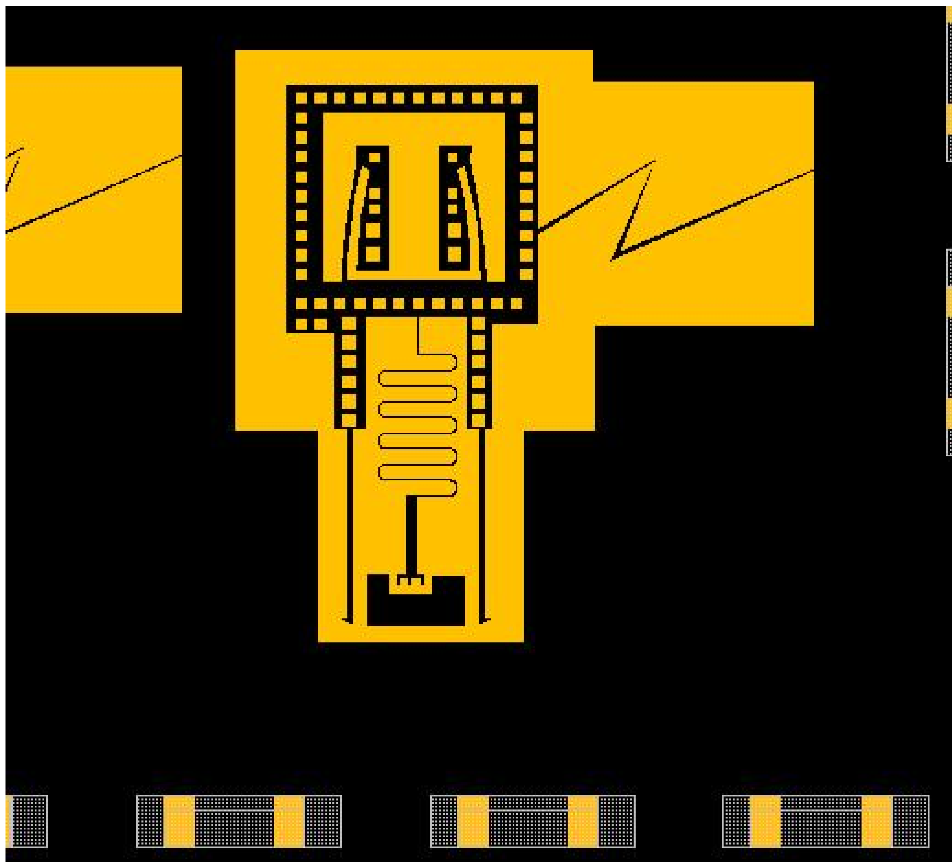

C13 Microsnapfastener type 2.

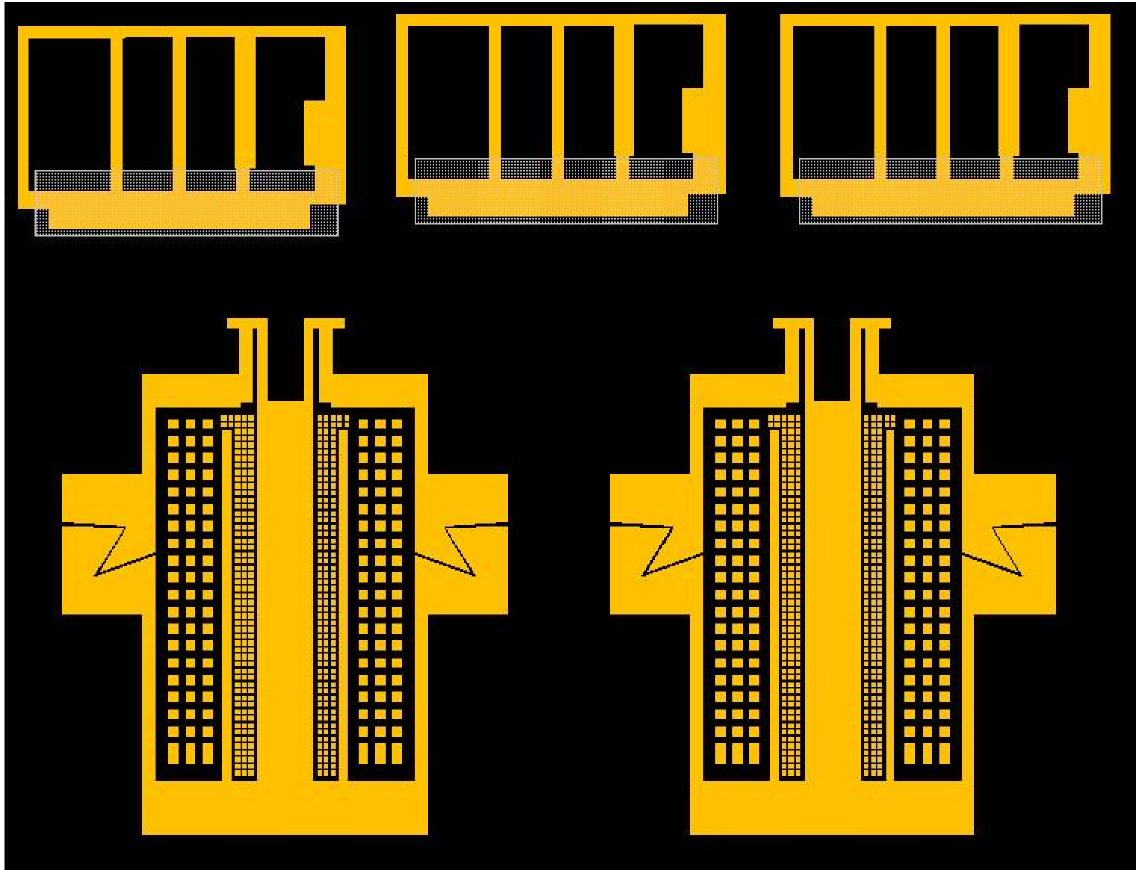

C.14 Z axis arm version 2.

REFERENCES

[1] M. Esashi, "MEMS Technology: Optical Applications, Medical Applications and SOC Applications," in Proc. of IEEE Symposium on VLSI Technology, 2002.

[2] M. Takeda, "Applications of MEMS to Industrial Inspection," in Proc. of IEEE International Conference on MEMS, 2001.

[3] M. Esashi, "Micro-Nano Electro Mechanical Systems for Practical Applications," in Proc. of IEEE International Conference on Nanotechnology, 2005.

[4] B.E. Boser "From Micro to Nano: MEMS as an interface to the nano world," in Proc. of IEEE International Conference on Computer-Aided Design, 2006.

[5] W.S.N Trimmer et al., "Integrated Fabrication of Polysilicon Mechanisms," IEEE Transactions on Electron Devices, Vol 35, No.6, Pp.719-723,1996.

[6] A. S. Velasco et al., "Double Sided Micromachining of Silicon on Insulator Films using Room Temperature Oxygen Plasma Assisted Bonding," Journal of Micromechanics and Microengineering, Vol.12. Pp. 786-794, 2002.

[7] A. Roger, "The LIGA Technique: What are the new opportunities," Journal of Micromechanics and Microengineering, Vol.2. Pp 133-140, 1992.

[8] T. Masaki, K. Kawata, T. Masuzawa, "Micro Electro-Discharge Machining and its Applications," in Proc. of IEEE MEMS, 1990.

[9] http://www.zyvex.com/nanotech/nano4/merklePaper.html

[10] http://crnano.org/

[11] http://www.mel.go.jp/

[12] N. Mishima, K. Ashida, T. Tanikawa and H. Maekawa, “Design of a Microfactory”, in Proc. of the ASME Design Engineering Technical Conference — 7th Design for Manufacturing Conference, Vol. 3, 2002.

[13] Y. Okazaki, N. Mishima and K. Ashida, “Microfactory and Micro Machine Tools”, in Proc. of the 1st Korea–Japan Conference on Positioning Technology, Pp. 1/6–6/6, 2002

[14] M. Suda, K. furata, T. Sakuhara and T. Akata, “The Microfactory System for Electrochemical Machining”, Galvanotechnik, Vol.9, Pp. 2607–2609, 2000.

[15] E. Drexler, "Engines of Creation", 1987.

[16] E. Garcia, M.A. Jimenez, P.G. De Santos, M. Armada, “The Evolution of Robotics Research,” IEEE Robotics & Automation Magazine, Volume 14, Issue 1, Pp: 90 – 103, 2007.

[17] T. Ebefors et.al, “A Robust Micro Conveyer Realized By Arrayed Polyimide Joint Actuators,” Journal Of Micromechanics And Microengineering, Volume 10, Issue 3, Pp. 337-349, 2000.

[18] P.Kladitis, V. Bright, K. Harsh, Y.Lee “Prototype Microrobotics For Micro Positiong In a Manufacturing Process And Micro Unmanned Vehicles,” in Proc. of IEEE 12th Workshop On Micro Electro Mechanical Systems (MEMS), 1999.

[19] M.H. Mohebbi, M.L. Terry, K.F. B¨ohringer, “Omnidirectional Walking Microrobot Realized By Thermal Microactuator Arrays,” in Proc. of ASME International Mechanical Engineering Congress And Exposition, 2001.

[20] B. Kim et.al, “A Ciliary Based 8-Legged Walking Micro Robot Using Cast IPMC Actuators,” in Proc. of the IEEE International Conference on Robotics & Automation, Taiwan, 2003.

[21] A. Bonvilain, N. Chaillet, “Microfabricated Thermally Actuated Microrobot,” in Proc. of the IEEE International Conference on Robotics and Automation, Taiwan, 2003.

[22] W. Driesen, A. Rida, J.M. Breguet, R. Clavel., ‘Friction based locomotion module for mobile MEMS robots,” in Proc. of IEEE/RSJ International Conference, CA, 2007.

[23] Sylvain Martel, “General description of the wireless miniature NanoWalker robot designed for atomic-scale operations,” in Proc. of SPIE Vol. 4568, 2003.

[24] Jeffrey S. Pulskamp, Kenn Oldham, “Highly Integrated Piezo MEMS Enabled Millimeter-Scale Robotics,” in Proc. of ASME International Design Engineering Technical Conferences, IDETC, 2009.

[25] Elbuken C., Khamesee M.B. and Yavuz M., “Large-Air gap Magnetic Levitation of Electrodeposited Co-Ni-Mn-P films”, in Proc. of IEEE Int. Conf. on Mechatronics and Automation, 2000.

[26] Bergbreiter, S.; Pister, K.S.J. "Design of an Autonomous Jumping Microrobot," in Proc.of IEEE International Conference on Robotics & Automation, ICRA, 2007.

[27] P. Valdastri, P. Corradi, A. Menciassi, T. Schmickl, K. Crailsheim, J. Seyfried, P. Dario, "Micromanipulation, Communication, Swarm Intelligence Issues in a Swarm Microrobotic Platform," Robotics and Autonomous Systems, Vol. 54, Pp.789-804, 2006.

[28] D. R. Frutiger, B. E. Kratochvil, K. Vollmers, B. J. Nelson, "Small, fast, and under control: wireless resonant magnetic micro-agents", International Journal of Robotics Research, 2009.

[29] C. Pawashe, S. Floyd, M. Sitti, ''Modeling and Experimental Characterization of an Untethered Magnetic Micro-Robot,'' International Journal of Robotics Research, Vol. 28, No. 8, 2009.

[30] B.R. Donald et al., “An Untethered, Electrostatic, Globally-Controllable MEMS Micro-Robot,” Journal of Microelectromechanical Systems, Vol 15, No. 1, Pp.167-173, 2006.

[31] R.J. Full, “Using Biological Inspiration To Build Artificial Life That Locomotes,” in Proc. of the International Symposium on Evolutionary Robotics from Intelligent Robotics to Artificial Life, 2001.

[32] J.M. Mcmichael, M.S. Francis, “Micro Air Vehicles – Toward A New Dimension In Flight,” DARPA Report, 1997.

[33] A. Hoover, E. Steltz, and R.S. Fearing, “RoACH: An autonomous 2.4g crawling hexapod robot,” in Proc. of IEEE International Conference on Intelligent Robots & Systems IROS, 2008.

[34] R.J. Wood, “The First Takeoff of a Biologically Inspired Robotic Insect,” IEEE Trans. on Robotics, Vol. 24, No. 2, Pp. 341-347, 2008.

[35] R.S. Fearing et al., “Wing Transmission for a Micromechanical Flying Insect,” Journal of Micromechatronics, Vol. 1, No. 3, pp. 221-238, 2002.

[36] O. Unver, A. Uneri, A. Aydemir, M. Sitti, "Geckobot: A Gecko Inspired Climbing Robot Using Elastomer Adhesives" in Proc. of IEEE International Conference on Robotics and Automation, 2006.

[37] M. Gauthier, E. Gibeau, D. Heriban, “Submerged Robotic Micromanipulation and Dielectrophoretic Micro-object Release,” in Proc. of 9th International Conference on Control, Automation, Robotics and Vision, ICARCV, 2006.

[38] S. Fatikow, J. Seyfried1, St. Fahlbusch, A. Buerkle, and F. Schmoeckel , “A Flexible Microrobot based Microassembly Station,” in Journal of Intelligent and Robotic Systems, Vol 27, No. 1-2, Pp: 112-191, 2000.

[39] N. Dechev, W. L. Cleghorn, J.K. Mills, “Microassembly of 3D MEMS Structures Utilizing Micogripper with a Robotic Manipulator,” in Journal of Microelectromechanical Systems, Vol. 13, Pp:11-19, 2004.

[40] M. Sitti, “Teleoperated and Automatic Nanomanipulation Systems using Atomic Force Microscope Probes”, in Proc. of IEEE International Conference on Decision and Control, ICDC, 2003.

[41] X. Liu, “A MEMS Stage for 3-Axis Nanopositioning, ” in proceedings of the 3rd Annual IEEE Conference on Automation Science and Engineering, CASE, 2007.

[42] J. Dong, D. Mukhopadhyay, P. M Ferreira, “Design, Fabrication and Testing of a Silicon-On-Insulator (SOI) MEMS Parallel Kinematics XY Stage,” Journal of Micromechanics and. Microengineering,” Vol 2, No. 17, Pp 1154–116, 2007.

[43] J.Y. Park, Y. Yaish, M. Brink, S. Rosenblatt, P.L. McEuen, “Electrical Nanoprobing of Semiconducting Carbon Nanotubes using an Atomic Force Microscope,” in Applied Physics Letters, Vol 80, Pp.444-456, 2002.

[44] R. Yeh,, Kruglick, E.J.J, Pister, K.S.J, “Surface-micromachined Components for Articulated Microrobots,” Journal of Microelectromechanical Systems Volume 5, Issue 1, Pp. 10 – 17, March 1996.

[45] J. Cecil, Derek Powel, Daniel Vasquez, “Assembly and Manipulation of Micro Devices—A state of the Art Survey,” Robotics and Computer-Integrated Manufacturing, Volume 23, Issue 5, Pp.580-588, 2007.

[46] C. G. Keller, R. T. Howe. “Hexsil tweezers for teleoperated micro-assembly”, In Proc. of IEEE Workshop on Micro Electro Mechanical Systems (MEMS), 1997.

[47] M. B. Cohn, R. T. Howe. “Wafer-to-wafer Transfer of Microstructures using Break Tethers”. United States Patent Application, May 1997.

[48] A. Singh, D. A. Horsley, M. B. Cohn, A. P. Pisano, and R. T. Howe. “Batch Transfer of Microstructures using Chip-Chip Solder Bump Bonding,” In Proc of International conference on Solid-State Sensors and Actuators,1997.

[49] M. B. Cohn "Self-Assembly of Microfabricated Devices", United States Patent 5-355-577, 1992.

[50] K. Hosokawa, I. Shimoyama, H. Miura. "Dynamics of Self-Assembling Systems- Analogy with Chemical Kinetics" Artificial Life, Vol.1, No.4, 1995.

[51] K. S. J. Pister, R. Fearing, and R. Howe. "A Planar Air Levitated Electrostatic Actuator System", in Proc. of IEEE Workshop on Micro Electro Mechanical Systems (MEMS),1990.

[52] A. Codourey, W. Zesch, R. Buechi, and R. Siegwart, "A Robot System for Automated Handling in Micro-World", in Proc. of IEEE/RSJ Intelligent Robots and Systems, 1995.

[53] J.T. Feddeman and R.W. Simon, "Visual servoing and CAD-driven microassembly," IEEE Robotics and Automation Magazine, Vol.5, No.4, Pp.18-24, 1998.

[54] B.J. Nelson, Y. Zhou, B. Vikramaditya, "Sensor-Based Microassembly of Hybrid MEMS Devices", IEEE Control Systems, Pp.35-45, 1998.

[55] A. Sulzmann, P. Boillat, J. Jacot, "New Developments in 3D Computer Vision for Microassembly", SPIE Conference on Microrobotics and Micromanipulation, 1998.

[56] W. Zesch, R.S. Fearing, "Alignment of Microparts Using Force Controlled Pushing," SPIE Conference on Microrobotics and Micromanipulation, 1998.

[57] Y. Zhou, B.J. Nelson, "Adhesion Force Modeling and Measurement for Micromanipulation", SPIE Conference on Microrobotics and Micromanipulation, 1998.

[58] N. Dechev, W. L. Cleghorn, J. K. Mills, "Microassembly of 3D Microstructures Using a Compliant, Passive Microgripper", Journal of Microelectromechanical Systems, Vol. 13, No. 2, 2004.

[59] S. Fatikow et al, "A Flexible Microrobot-Based Microassembly Station," Journal of Intelligent and Robotic Systems, Volume 27, Issue 1-2, 2000.

[60] “National Nanotechnology Initiative”, National Science and Technology Council/Committee on Technology/Subcommittee on Nanoscale Science, Engineering and Technology, July 2000.

[61] A. Ulman, “An introduction to Ultrathin Organic Films,” Academic Press,1991.

[62] A. Ulman, “Formation and structure of Self Assembled Monolayers,” Chem. Rev. Vol. 96, No. 4, Pp. 1533-1554, 1996.

[63] T. Hogg, “Robust Self-Assembly Using Highly Designable Structures,” Nanotechnology, Vol. 10, No. 3, Pp. 300-307, 1999.

[64] P. A. Lewis, et al., “Control and placement of molecules via self-assembly,” Nanotechnology, Vol. 12, No. 3, Pp. 231- 237, 2001.

[65] M. Sitti, “Survey of nanomanipulation systems,” in Proc. of IEEE-Nanotechnology Conference, 2001.

[66] A. A. G. Requicha, “Nanorobots, NEMS, and nanoassembly,” in Proc. of IEEE, Vol. 91, No. 11, Pp. 1922-1933, 2003.

[67] “Nanoscience and Nanotechnologies: opportunities and uncertainties”, Royal Society & The Royal Academy of Engineering Report, 2004.

[68] Z. Wang, P. Boggild, S. Fatikow, S. Su, D T Pham, “Object Oriented Nanoassembly,” European Project Proposal, No. FP6-505865-1.

[69] S. Fatikow, et al, “Smart Nanorobots for Automatic Object Handling in Different Application Fields,” European project proposal, No. FP6-011862-2, 2004.

[70] S. Fatikow, “Robotized Nanomanufacturing: Current Developments and Future Trends”, Proc of Virtual International. Conference on Intelligent Production Machines and Systems, 2005.

[71] R.P. Feynman, “There’s Plenty of Room at the Bottom,” Science, Vol. 23, Pp. 22–36, 1960.

[72] K.E. Drexler, Nanosystems “Molecular Machinery, Manufacturing, and Computation,” Wiley Interscience, 1992.

[73] G. Binning, H. Rohrer, C. Gerber, E. Weibel, “Tunneling through a Controllable Vacuum Gap.” Applied Physics Letters, Vol. 40, No. 2, Pp. 178-180, 1982.

[74] G. Binning, H. Rohrer, C. Gerber, E. Weibel, “Surface Studies by Scanning Tunneling Microscopy,” Physics Letters, Vol. 49, No.1, Pp. 57–61, 1982.

[75] G. Binning, C. F. Quate, C. Gerber, “Atomic Force Microscope,” Physics Letters. Vol. 56, No. 9, Pp. 930–933, 1986.

[76] http://www.veeco.com/products/Metrology_and_Instrumentation/

[77] J. A. Stroscio, D. M. Eigler, “Atomic and Molecular Manipulation with the Scanning Tunnelling Microscope,” Science, Vol. 254, No. 5036, Pp. 1319-1326, 1991.

[78] T. A. Jung, R. R. Schlitter, J. K. Gimzewski, H. Tang, C. Joachim, “Controlled Room-Temperature Positioning of Individual Molecules,” Science, Vol. 271 No. 5246, Pp. 181-184, 1996.

[79] P. H. Beton, A. W. Dunn, P. Moriarty, “Manipulation of C60 molecules on a Si surface,” Applied Physics Letters, Vol. 67, No. 8, Pp. 1075-1077, 1995.

[80] “The Nano Revolution”, European Research, 2002.

[81] F. Fukuda, F. Arai, L. Dong, “Nano Robotic World – from Micro to Nano,” in Proc. of IEEE International Conference on Robotics and Automation, 2001.

[82] P. Kim, C. M. Lieber, “Nanotube Nanotweezer", Science, Vol. 286, Pp. 2148-2150, 1999.

[83] P. Boggild, T. M. Hansen, C. Tanasa, F. Grey, “Fabrication and Actuation of Customized Nanotweezers with a 25nm gap,” Nanotechnology, Vol. 12, Pp. 331-335, 2001.

[84] P. Boggild et al. “Customizable Nanotweezers for Manipulation of Free-standing Nanostructures,” IEEE-NANO 2001,

[85] C. L. Petersen, T. M. Hansen, A. Bosisen, O. Hansen, T. Hassenkam and F. Grey, “Scanning Microscopic Four-Point Conductivity Probes,” Sensors and Actuators , Vol. 96, Pp. 53-58, 2002.

[86] R. Lin, O. Hansen, “Microcantilever equipped with Nanowire Template Electrodes for Multiprobe Measurement on Fragile Nanostructures,” Journal of Applied Physics, Vol. 96, No. 5, Pp. 2895- 2900, 2004.

[87] T. Fukuda, F. Arai, L. Dong, “Assembly of Nanodevices with Carbon Nanotubes through Nanorobotic Manipulations,” in Proceedings of the IEEE, Vol. 91, Pp. 1803–1818, 2003.

[88]Toshio Fukuda et al., “Nanoscale Cutting, Bending and Welding in a Nanoassembly,” in Proc. of the 2nd IEEE International Conference on Nano/Micro Engineered and Molecular Systems, 2007.

[89] S. G. Kim, M. Sitti, ''Task-Based and Stable Tele-Nanomanipulation in a Nanoscale Virtual Environment,'' IEEE Trans. on Automation Science and Engineering, Vol. 3, No. 3, Pp. 240-247, 2006.

[90] www.zyvex.com/Documents/Zyvex_S100.PDF

[91] http://www.nanotechnik.com/mm3a-em.html

[92] P T Docker, P K Kinnell, M C L Ward, “Development of the one-step DRIE dry process for unconstrained fabrication of released MEMS devices,” J. Micromech. Microeng.Vol 14, Pp. 941–944, 2004.

[93] Wenhua Zhang et al., “SCREAM'03: A Single Mask Process for High-Q Single Crystal Silicon MEMS,” in Proc. of ASME International Mechanical Engineering Congress and Exposition, IMECE , 2004.

[94] A. N. Das et al., “μ³: Multiscale, Deterministic Micro-Nano Assembly System for Construction of On-Wafer Microrobots,” in Proc. of IEEE International Conference on Robotics and Automation, ICRA. 2007.

[95] R. Murthy, A.N. Das, D. O. Popa, “High Yield Assembly of MEMS Snap Fasteners,” in Proc. of ASME-International Design Engineering Technical Conferences, 2008.

BIOGRAPHICAL INFORMATION

Rakesh Murthy received his Master of Science degree in Mechanical Engineering from the University of Texas at Arlington in 2005.